ABSTRACT

Title of Document: CLINOROTATION TIME-LAPSE MICROSCOPY FOR LIVE-CELL ASSAYS IN SIMULATED MICROGRAVITY

Alvin Garwai Yew, Ph.D., 2013
Department of Mechanical Engineering

Directed By: Associate Professor Adam Hsieh
Research Assistant Professor Javier Atencia
Fischell Department of Bioengineering

To address the health risks associated with long-term manned space exploration, we require an understanding of the cellular processes that drive physiological alterations. Since experiments in spaceflight are expensive, clinorotation is commonly used to simulate the effects of microgravity in ground experiments. However, conventional clinostats prohibit live-cell imaging needed to characterize the time-evolution of cell behavior and they also have limited control of chemical microenvironments in cell cultures. In this dissertation, I present my work in developing Clinorotation Time-lapse Microscopy (CTM), a microscope stage-amenable, lab-on-chip technique that can accommodate a wide range of simulated microgravity investigations. I demonstrate CTM with stem cells and show significant, time-dependent alterations to morphology. Additionally, I derive momentum and mass transport equations for microcavities that can be incorporated into various lab-on-chip designs. Altogether, this work represents a significant step forward in space biology research.

CLINOROTATION TIME-LAPSE MICROSCOPY FOR LIVE-CELL ASSAYS IN SIMULATED MICROGRAVITY

By

Alvin Garwai Yew

Dissertation submitted to the Faculty of the Graduate School of the
University of Maryland, College Park, in partial fulfillment
of the requirements for the degree of
Doctor of Philosophy
2013

Advisory Committee:
Dr. Adam Hsieh, co-Chair
Dr. Javier Atencia
Dr. Amr Baz
Dr. Miao Yu
Dr. Chandrasekhar Thamire
Dr. David Akin, Dean's Rep

Dedication

For that special someone

Acknowledgements

Above all, I'd like to thank my family for their years of unconditional support and my friends for making life more meaningful. To Adam Hsieh for his guidance as my advisor, commitment to my educational well-being, and understanding as a friend. To Javier Atencia, also a caring advisor, who served as a model for how to excel in research and shared his passion with me. Thanks to all the members of the Orthopaedic Mechanobiology Lab who were empathetic, considerate, and troublemaking accomplices. Special acknowledgement to Julianne Twomey, Hyunchul Kim, and Sang-Kuy Han. Finally, I owe much gratitude to my NASA colleagues for their unwavering confidence, especially Lawrence Han, Chuck Clagett, Tupper Hyde, and Karen Flynn. -- Thank you.

Table of Contents

1. Introduction

1.1. Manned space exploration

In the cutthroat environment of the multi-year economic recession that collapsed global markets in 2008, and with the ongoing fiscal stagnation threating to damage its slow recovery, all government programs and budgets in the United States (US) are under scrutiny, or otherwise threatened with a permanent shutdown.

While this does not exclude the National Aeronautics and Space Administration (NASA), the financial scrutiny is not new. Consider that every year since the completion of the Apollo program in the early 1970's, NASA is continually faced with criticism for spending beyond its means. If not criticized for spending, which typically constitutes less than 1% of the US federal budget, some claim that NASA is irrelevant, and its mission outdated.

I won't go into a lengthy discussion here on why the world's most prolific space program continues to inspire, why it represents so many aspects of what distinguishes mankind from every other species on Earth, and why it spurs the type of technological innovation that has been, and should continue to be, the furnace of the US economy. The debate on NASA's relevance may carry on indefinitely.

However, what I believe is important is that NASA's budget should be proportional to a manageable portfolio of ambitious goals. Otherwise, underfunded programs may fail to deliver. While I do not claim to know a whole lot about how money flows in the US economy or how NASA's money is managed, I know that any successful modern-day venture requires adequate financial backing. Given that

NASA is targeting a goal of long-term manned space exploration, the monetary investment is, by no means, trivial. So, I claim that adequate funding is the first important component needed for manned space exploration.

The second component is technology. Its capabilities should reflect the duration and destination of the mission and include the space vehicle architecture, propulsion, communications, navigation, and power systems. Moreover, there is a class of technology that is related solely to the human factor, protecting humans from the harsh space environment and maintaining human health. In order to better design technologies for this, we need to better understand how the human body interacts with the space environment. This is the crux of my dissertation.

In NASA's overall vision to "reach for new heights and reveal the unknown so that what we do and learn will benefit all humankind," [1] my dissertation plays a small, but important role. Small because its focus is very narrow and important because it supports such a large portion of NASA's investments. To elaborate, consider NASA's recently released 2013 budget estimate of $17.7 billion [2]. Of NASA's programmatic elements of human exploration and operation (HEO), aeronautics research, and science, HEO comprises of roughly half of NASA's expenditures (see Fig. 1).

The HEO element houses the space biology program, which supports HEO sub-elements for the international space station and exploration research. The NASA centers that most heavily support space biology research are Johnson Space Flight Center (JSC) and Ames Research Center (ARC). Outside of NASA, other organizations have limited investments in this field.

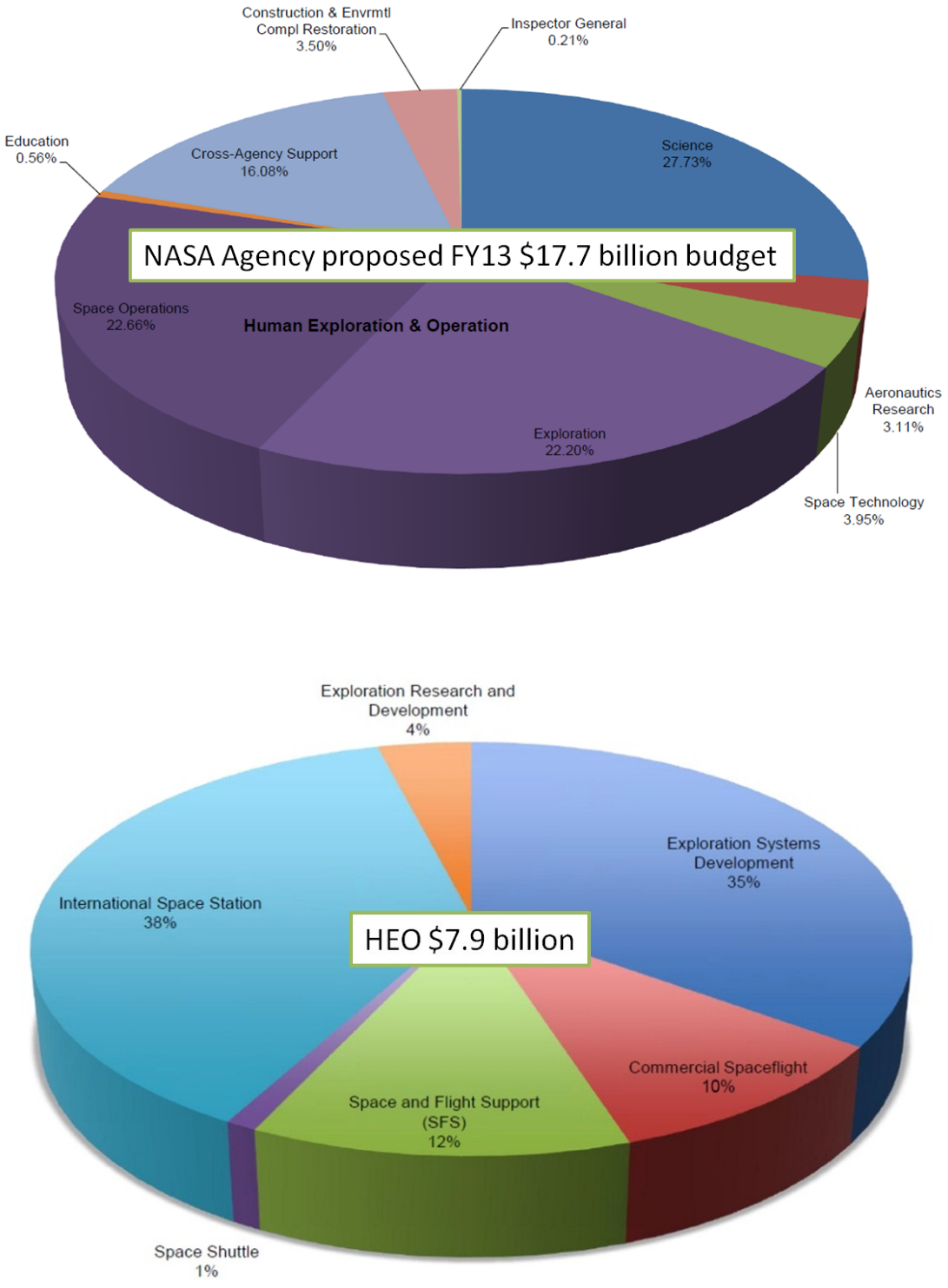

Figure 1. NASA's FY13 budget estimate for the agency and for the Human Exploration and Operations (HEO) element. Reproduced from [2].

1.2. The human factor

Radiation fields, an airless vacuum, cold temperatures, and weightlessness are some of the environmental conditions that astronauts must overcome to survive in space. Atmospheric pressure and temperature can be easily controlled. Radiation however, is perhaps the most hazardous, and weightlessness, sometimes used interchangeably with the term microgravity, is perhaps the least understood and most difficult to address. Even under brief exposure to radiation and microgravity, astronauts generally return to Earth with physiological conditions that may take weeks, or even months to recover.

First, let me briefly describe the radiation environment. The three primary types that relate to spaceflight are galactic cosmic radiation, solar cosmic radiation, and radiation from the van Allen belts around Earth [3]. While Earth's atmosphere provides adequate shielding on the ground, and the magnetosphere is somewhat adequate for shielding in low Earth orbit (LEO), a long-term mission far from Earth would expose astronauts to dangerous levels of galactic cosmic radiation. This type of radiation, a remnant of cataclysmic cosmic events, comprises of roughly 1% heavy elements that can penetrate through most barriers and damage genetic material.

We may also want to consider that future, long-term manned space exploration might use alternative power sources that provide far more energy than conventional solar cells. Radioisotope thermoelectric generators (RTGs) are already used to power deep space missions and an RTG system is currently used on the Mars Curiosity rover [4]. The use of similar, nuclear power technology on long-haul space vehicles may expose astronauts to additional sources of radiation.

In contrast, the effects of microgravity exposure are less dramatic and occur over timescales that are orders of magnitude longer than damage incurred by radiation. In fact, the body's response to microgravity exposure is more of a natural adaptation than a change caused by some exogenous factor. However, adaptations do not always imply that alterations are favorable for all systems in the body.

As an example: decreased bone density and reduced muscle mass might help an astronaut conserve caloric energy in microgravity. Although this energy conservation is favorable from an evolutionary standpoint, tissue atrophy might adversely affect hormone balance that could disrupt sleep and mental health [5] – not to mention that such changes would physically hamper the ability for astronauts to readapt to Earth's gravity.

Experiments in spaceflight have previously been used to investigate the effects of microgravity. In particular, cellular specimens in spaceflight exhibit abnormal, time-evolving morphology and cytoarchitecture, e.g. cytoskeleton and focal adhesions [6-9], which may affect certain cell events including replication, differentiation, migration, and signaling [10-13].

These events generally confer broader changes to tissues that can lead to reduced bone mineral density, muscle atrophy, and other ailments [14]. Specifically, it has been well-established that astronauts encounter roughly 1-2% loss in bone mineral density for every month in spaceflight [15-17]. Muscle strength is notably decreased, post-flight in astronauts and while large variability exists in measurements, muscle volume losses of certain muscle types have been recorded at roughly 40% [18-20]. Additionally, in the first 24 hrs of spaceflight, astronauts may encounter a

17% reduction in plasma volume, which leads to total decrease of 10% in total blood volume [21]. In one survey of 58 NASA astronauts, 68% reported low back pain, with some reporting moderate to severe pain [22,23].

Table 1 summarizes some of the major physiological conditions that astronauts encounter in spaceflight and postflight. From Table 1, it is clear that there is a time-dependent effect of microgravity exposure on the physiologic severity of symptoms. That is, astronauts who spend a longer time in space are more susceptible to encountering severe physiological alterations. Consequently, we would expect that longer exposures to microgravity would correlate to a longer time to recovery in postfight. In some cases, recovery may even take years.

Table 1. Timeline of physiologic conditions afflicting astronauts from launch to postflight recovery. Reproduced from [21].

Physiologic effects	Launch	Duration of flight				Landing	Postflight period		
		24 h	48 h	2 wk	> 1 mo		24–48 h	1–2 mo	> 1 yr
Fluid redistribution	• Redistribution of fluid to the torso and head • 10% decreased fluid volume in the legs	• 17% reduction in plasma volume	• Gradual decrease in erythropoietin secretion, leading to a 10% decrease in total blood volume			• Orthostatic hypotension from pooling of fluids in the legs	• Return of normal fluid distribution		
Neurovestibular effects	• Space motion sickness					• Space motion sickness			
Muscle changes		• Gradual decrease in muscle mass by 20%			• Gradual decrease in muscle mass by 30%	• Muscle soreness and tightness		• Full recovery of muscle mass and strength	
		• Gradual decrease in muscle strength (up to 50% loss observed)							
Bone demineralization		• 60%–70% increase in calcium loss (urinary, fecal). Reduced parathyroid hormone and vitamin D production.							• Complete or almost complete restoration of bone density
		• Gradual loss of bone density (1%–2% per month)							
Psychosocial effects	• Fatigue, sleep debt, isolation, emotional effects, stress to the astronaut's family, multicultural crew environment								
Immune dysregulation		• Possible reactivation of latent herpes viruses and impairment of cell-mediated immunity				• Numerous cellular and other changes leading to impaired immunity		• Gradual improvement in immunity (days to weeks)	

Therefore, the success of long-term manned space exploration requires countermeasures that address the underlying cellular changes adopted in microgravity and are most effective if they consider the time-evolution of these changes.

1.3. Mechanotransdution in microgravity

Consider how mechanical stimulus on some tissue might produce a biological response that changes the tissue makeup. If the balance of forces, chemicals, etc. is not in equilibrium, sustaining this stimulus over time yields tissue properties that could be very different from its original configuration [24]. This phenomenon describes a synergistic process known as functional adaption [25-27]. As an example of functional adaptation, take the case of a weightlifter building muscle mass to accommodate increased mechanical stress. While his muscles might not instantaneously enlarge, biological processes occur at smaller scales where adaptations may begin to take place.

Mechanotransduction then, is the complex biological pathway where mechanical signals are transferred from one level to another and ultimately "sensed" by a cell through some signaling cascade, conformational change on a membrane protein or other mechanism. Even a force as seemingly benign as gravity elicits biological responses that result in functional adaptation. But what is the pathway for gravity sensing? Are local changes in nutrient supply - a result of fluid shifts and reduced cardiovascular activity, for example - more of a driving factor in determining cell response than gravity as a mechanical stimulus? The National Aeronautics and Space Administration (NASA) has invested heavily in its human spaceflight program,

which includes research to answer such questions [28,29] and the future success of manned missions depends on finding ways to mitigate risk factors in spaceflight.

The way in which cells may perceive gravity is called ‘gravisensing’. Many biological systems have formed in the presence of Earth gravity and function optimally under 1-g conditions. We believe that removal of Earth gravity acts on cells in predominantly two ways: as a mechanical stimulus (local alterations) and as a mechanism that changes a cell's chemical microenvironment (systemic, or hormonal alterations). This dissertation focuses on the former.

Specifically, local cellular alterations may prohibit density-based loading of cell components that are characteristic of the 1-g environment and may also alter the convective flow environment around cells. There may be other important cellular effects associated with the microgravity environment, which are thoroughly reviewed by other authors [30,31]. An intriguing example of cellular gravisensing relates to some specific cells that have developed crystal structures called statoliths that slide over mechanosensitive cells like dead weights. Statoliths can be found, for example, in the inner ear and also in the roots of some types of plants. While these types of density forces in the microscopic world play a small role compared to other factors, such as surface forces, polymerization, and electrical forces as illustrated in Fig. 2, the effect of gravity may still be consequential.

Of particular interest to the space biology community, is how cytoskeletal alterations, due to mechanical unloading, may affect cell response. We’re interested in studying the cytoskeleton because it is involved in most of the major cell processes in the cell cycle, changes occur dynamically, it can be observed in the short term, and

it is relatively easy to observe with fluorescent tagging. Figure 3 shows how microgravity could disrupt certain stages in the cell cycle where the cytoskeleton plays an important role. The cytoskeleton is anchored to a number of cell structures, notably focal adhesions that are distributed throughout the cell membrane. These focal adhesions are responsible for sensing mechanical signals from the surrounding microenvironment and also help cells to migrate.

Li, et. al., 2009 [7] studied how modeled microgravity affects the cytoskeleton and focal adhesions in MCF-7 cells. Even though the study did not provide same-cell images, some interesting observations were made. Migration was significantly decreased when compared with controls in normal gravity. Cytoskeletal organization and microtubule formation were disrupted. Additionally, the distribution of vinculin focal contacts was significantly decreased in modeled microgravity.

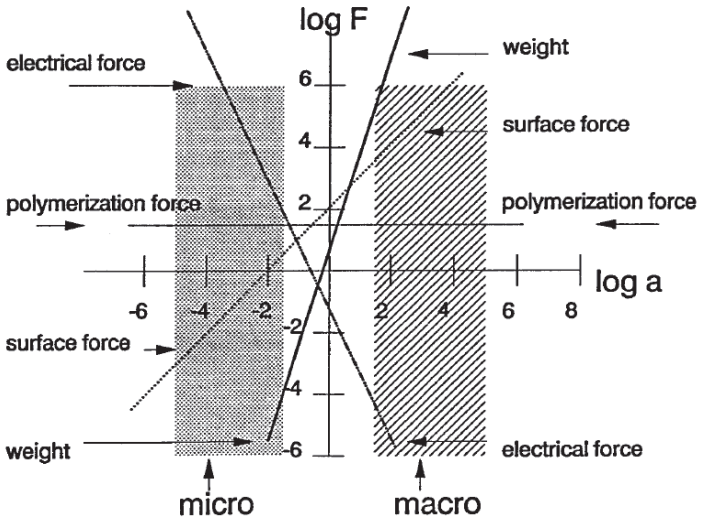

Figure 2. Graphical depiction of how various forces (*F*) may affect particles at different length scales (*a*). Objects in the microscopic world are dominated by electrical forces; polymerization forces can overcome surface and gravity forces. These relationships are inverted in the macroscopic world. Reproduced from [31].

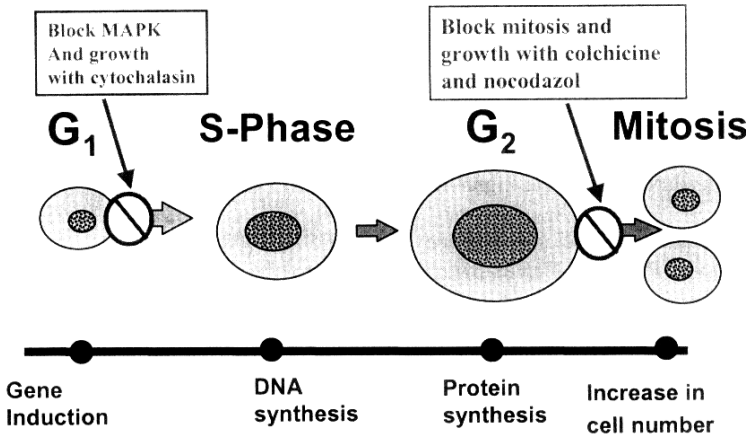

Figure 3. Time points in the cell cycle sensitive to cytoskeletal alterations and require polymerization for growth. Reproduced from [32].

The authors hypothesized that changes to the cytoskeleton and focal contacts in modeled microgravity are linked to inhibited migration behavior of MCF-7 cells. Specifically, disruption of the microtubule organizing centers alters the normal "push" and "pull" forces required for migration. Also, disruptions in the intracellular tension of actin filaments may compromise the complex cytoskeletal meshwork needed for maintaining normal cellular processes and inhibit polarization needed for migration events.

Finally, the reported decrease in focal adhesions may hamper its normal formation and disassembly, and limit cell spreading. These findings were studied further by verifying the enzymatic activity associated with the regulation of focal adhesion kinase activity, which was down-regulated in modeled microgravity, but did not show a time-dependent behavior. However, time-point data of vinculin number and focal adhesion area did indicate time-dependence.

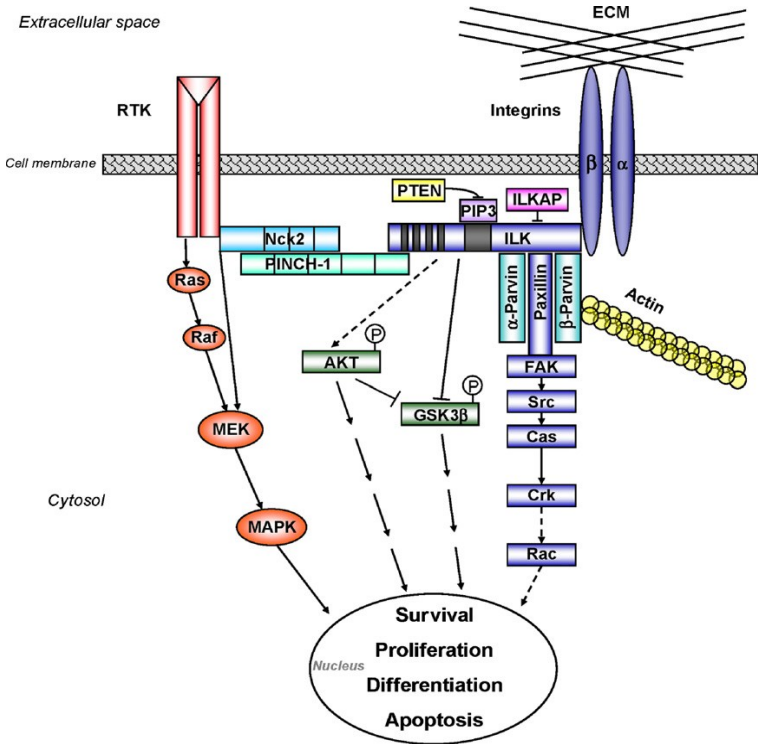

Figure 4. Integrin-actin-RTK signaling network is coordinated by RTK and the integrin-linked-kinase (ILK). Reproduced from [33].

The most fundamental level of mechanotransduction concerns the molecular and genetic response to mechanical signals. Although this is not directly the focus of my dissertation, I think a general discussion of signaling pathways is useful for understanding how my experiments relate to mechanotransduction. Signaling pathways involve a coordinated interaction between various cell structures, enzymes, and targeted gene(s) that relate to a cell's response. As an example, consider the integrin-actin-RTK (receptor tyrosine kinase) network in Fig. 4. Integrin-actin-RTK signaling is implicated in cellular proliferation, apoptosis, and differentiation, and may also be involved in other cell processes including migration and differentiation.

For example, in integrin-actin-RTK signaling, the dynamic behavior of collagen in the extracellular matrix (ECM) could cause time-dependent conformational changes to integrins, and affect binding to the integrin-linked-kinase (ILK). Similarly, actin interacts with ILK through Parvin molecules. In cooperation with RTK, ILK then coordinates the signaling cascade to ultimately regulate important cell processes. Let's then consider that microgravity could impose abnormal structural loads or fluid shear on tissues and transfer those signals to the ECM and actin filaments, which may ultimately alter normal cell processes.

Now, let me discuss all this in the context of a complete cellular analysis. The way in which researchers identify active signaling pathways is to first, analyze the enzymatic content of cells. This is usually accomplished by lysing cells and then using, for example, some type of spectrocolorimetric technique, such as ELISA [34] or electrophoresis, such as Western blotting [35].

An up-regulation in the phosphorylation of a certain enzyme, when compared with a control, might indicate that a certain pathway is more active. Active pathways can usually be confirmed by analyzing the expression of fragments of DNA, or genes, that are responsible for the phenomena of interest. The most widely used technique for this is called polymerase chain reaction (PCR) [36], and similarly, RT-PCR to replicate, or amplify these DNA fragments and make them easier to detect. Finally, a complete cellular analysis requires that we analyze a more global parameter, such as the protein composition of the ECM or something like the morphology of the cell, which may allow us to infer the state of a cell or how it is interacting with its local microenvironment.

1.4. Models of microgravity

The term "microgravity" is often used loosely, as we have done so far. Technically, there is a difference between zero-g, weightlessness and microgravity. To understand their subtleties it is useful to review Newton's law of gravitation, which states that two objects with masses m_1 and m_2 separated by a distance r will experience an attractive force of $F = Gm_1m_2/r^2$, where G is a universal constant equal to 6.674 x 10^{-11} N-(m/kg)^2. At Earth's surface, the acceleration a of an object with mass m_2 due to gravitational attraction can be calculated using Newton's second law of motion $F=m_2a$. Thus, the average acceleration due to Earth's gravity at the surface is $a=Gm_1/r^2$=9.8 m/s^2, which is the reference value for 1-g.

In order to achieve true 0-g, an object must be infinitely far in space from any other object; since this is physically impossible, 0-g does not truly exist. Within a moving reference frame however, an object can experience weightlessness if the net sum of forces is zero, which simulates the 0-g condition. Likewise, true microgravity is when the gravitational acceleration is 10^{-4}- to 10^{-6}-g. Even for satellites in high Earth orbit, which exceeds the altitude of the International Space Station, true microgravity is not achieved. A distance of over five times the span from the Earth to its moon is required for true microgravity relative to Earth. To get a better understanding, consider that a small object would need to assume Saturn's average orbit for true microgravity relative to the Sun!

Although there is semantic ambiguity in literature, microgravity is defined to be accelerations on an object, due to real and fictitious forces within a moving

reference frame, whose net sum is in the microscale. *Simulated* microgravity simply means that that the *apparent* effects of true microgravity are reproduced.

Since experiments in spaceflight are expensive, ground-based analogues have been used to simulate its effects. Tissue-level simulations usually assume a hindlimb unloading (HLU) configuration, i.e. head-down, feet-up in animal models (see Fig. 5). During HLU, changes in load-bearing properties of cancellous bone, such as decreased bone mineral density, are comparable to observations in flight [37,38]. Musculoskeletal structures in the weight-bearing lower limbs, both in animal models and astronauts in spaceflight, typically see more drastic alterations than tissues in the upper body. Though useful, tissue-level studies are limited since spatiotemporal changes in cell- and molecular-levels are not easily observed, which we believe to be the underlying processes that drive physiological alterations.

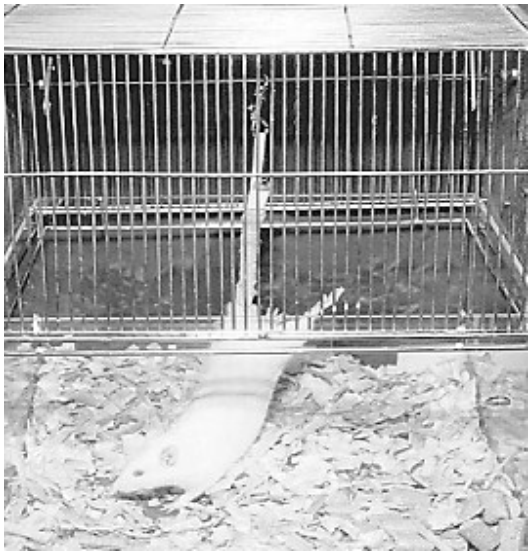

Figure 5. Hindlimb unloading for rat animal model used to simulate whole-body effects of microgravity on Earth. Reproduced from [39].

Figure 6. Commercially-available conventional clinostats from Synthecon Inc. Reproduced from [40].

The most common method of cellular-level microgravity simulation is clinorotation through a device called a clinostat (see Fig. 6). Early versions of the modern clinostat were built in the 1700s. Fundamentally, the device works as a rotating stage that constantly reorients the gravity vector on an object to eliminate a preferential direction. Clinostats were first used to study geotropism, the spatially-directed growth of plants due to gravity. In the late 1800s, animal cells and organs were studied in fluid-filled cylindrical containers rotating on its long axis. By 1980, the first reported mammalian cells were subjected to clinorotation [41,44].

Cell-based clinostat experiments generally compare well with microgravity experiments [41-43] and therefore, clinorotation has generally been accepted as a feasible ground-based analogue for spaceflight. Clinostat variants include the random positioning machine, which is a 3D version of the traditional clinostat and the RVW

bioreactor, which changes the particle physics to facilitate exposure to nutrients by rotating at a different speed.

1.5. Conventional clinorotation devices

Figure 7 shows a simulation of adherent cells seeded on a microcarrier bead in a clinostat. The beads observe unique physics, following a slightly elliptical path as viewed from the inertial frame and spiraling outward. In the rotating frame, these bead would appear to move in small circular paths, where a particle trace forms what looks like a daisy-chain link propagating toward the outer clinostat wall. Since the time-average of forces on bead in the clinostat is zero, the cells are said to be experiencing simulated microgravity [44,45].

Clinorotation has been used as a method by some researchers to enhance the quality of tissue engineering investigations. Tissues grown in clinostats corroborate some spaceflight studies that show that larger aggregates form under microgravity conditions when compared with conventional 2D techniques [46,47]. However, it is important to note that microgravity studies remain far from being conclusive; results from different investigations are at times, contradictory. We believe that this is primarily due to the large variation in experimentation using conventional clinostats.

For example, some researchers have found that microgravity inhibits proliferation and osteogensis in stem cells [48-51]. Others have found that microgravity potentiates proliferation and sustains stem cells' ability to differentiate [52-54]. Aside from these contradictions, what makes space biology extremely challenging is how different cell types respond to microgravity in different ways.

The rotation speed for clinostat walls is set to counter rates of sedimentation, and should seek to minimize the radius of the circular path in the rotating frame. Spin too slow and particles sediment due to gravity. Spin too fast and particles sediment due to centrifugal force. To summarize, the forces acting on particles in the rotating frame are gravity, centrifugal and coriolis and must be balanced with Stokes drag forces to minimize shear while maximizing delivery of nutrients.

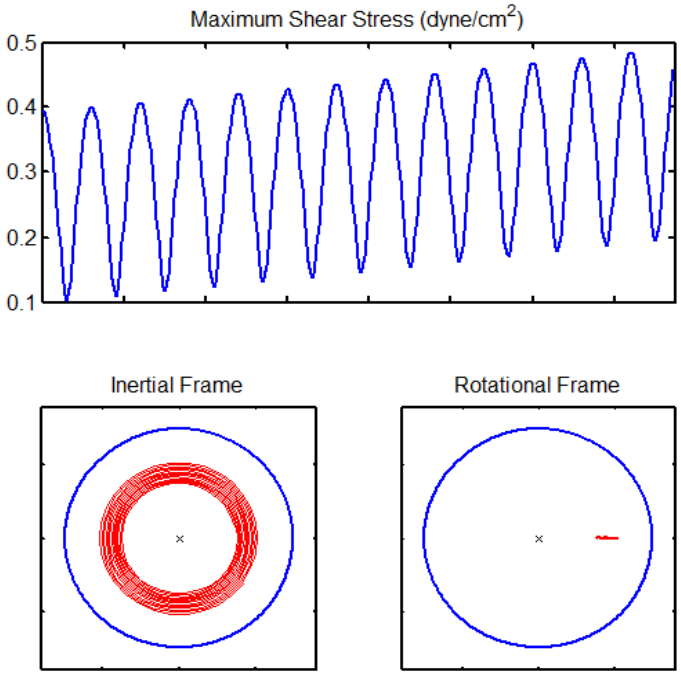

Figure 7. Conventional clinostat simulation. Matlab code in Appendix A, 4s time interval of a 200 μm Cytodex microcarrier bead with a density of 1.04 g/cm^3. Clinostat is 15 cm in diameter, filled with water and rotated at 200 RPM. *Top*: Maximum shear stress on microcarrier bead is oscillatory and increases as the particle moves outward toward the container wall. *Bottom Left*: Particle trace in the inertial frame. Particle spirals outward due to centrifugal force. Coriolis and gravity effects are relatively small. *Bottom Right*: Particle trace in the rotating frame. The particle has displaced several centimeters outward and will collide with the container wall multiple times for long-term testing.

In other words, the equation $F_{gravity}+F_{centrifugal}+F_{coriolis}=F_{stokes}$ yields the resulting equilibrium equations:

$$\sum F_x: \; a^2\Delta\rho\cdot\left[g\cos(\alpha)+\omega^2 r\cos(\beta)+2\cdot\omega\cdot u\cos(\gamma-\beta)\sin(\beta)\right]=8\mu\cdot u\cos(\gamma) \qquad (1)$$

$$\sum F_y: \; a^2\Delta\rho\cdot\left[g\sin(\alpha)+\omega^2 r\sin(\beta)-2\cdot\omega\cdot u\cos(\gamma-\beta)\cos(\beta)\right]=8\mu\cdot u\sin(\gamma) \qquad (2)$$

where a is the radius of the particle in suspension, $\Delta\rho$ is the differential density between the particle and the fluid medium, g is the gravitational constant, α is the angle from horizontal that the clinostat has rotated in the inertial frame, β is the angle from horizontal that points to the particle in the rotating frame, γ is the angle from horizontal that describes the velocity direction of the particle in the rotating frame (first unknown parameter), ω is the angular velocity of the clinostat rotation, μ is the dynamic viscosity of water and u is the terminal velocity magnitude of the particle in the rotating frame (second unknown parameter). Two unknown parameters with two nonlinear equations can be solved by numerical methods.

1.6. Microfluidics technology

The goal of this dissertation is to improve on state-of-the-art clinorotation devices, namely conventional, fluid-filled containers. Since particle physics in conventional clinostats is impossible to accurately control in experiments, cells can be subjected to mechanical forces and chemical gradients that might not be physiological. Additionally, adherent cells in these clinostats need to be seeded on microcarrier beads that have limited surface area for proliferation, which prohibits long-term

culture. Moreover, the constant movement of cells through culture media makes dynamic bioassays, which are important for a more holistic understanding of cellular response, generally unattainable. Finally, conventional clinostats can only offer a narrow range of possible science investigations.

Thus, there is much room for improving on ground-based methods of microgravity simulation. We are targeting methods that will allow us to precisely modulate microscale flow to create physiological cell culture environments, a feature that is not possible with conventional clinostat devices. Specifically, the surge of lab-on-chip technologies and microfluidics in the past decade has enabled unique capabilities for studying cellular response.

Microfluidics technology has become attractive for establishing appropriate culture conditions to enable cell culture in microcavities [55,56], *in vitro* differentiation of shear sensitive cells [57-59], and the generation of stable spatiotemporal gradients to study chemotaxis [60-62], among other applications [63,64]. Like conventional clinostats however, existing microfluidics techniques do not always provide a way to predict the microenvironment around cell cultures and may therefore impose unphysiological shear and chemical conditions. If we can find a way to rationally design microfluidics devices in combination with clinorotation, then we can offer a very powerful tool for space biology research by subjecting cells to complex chemical and shear gradients in their microenvironments.

1.7. Dissertation organization and significance

This dissertation presents my work on improving conventional clinorotation methods and is organized as follows: in Chapter 2, I discuss the use of lab-on-chip

devices for low-shear cell culture and for predicting chemical environments in cavities. Chapter 3 describes how these lab-on-chip devices can be incorporated onto a, "clinochip" platform for microgravity simulation and time-lapse microscopy. Preliminary experiments using the so-called, Clinorotation Time-lapse Microscopy (CTM) system is presented in Chapter 4. Finally, along with my conclusion for this dissertation, Chapter 5 also describes the path forward for CTM with a novel proposal to study osteogenesis in microgravity by looking at mesenchymal stems cells subjected to chemical gradients.

In terms of the significance of my work, I believe that CTM has the potential for more widespread use in space biology research and may find some commercial interest for tissue engineering applications. This, of course, would not be the first spaceflight innovation to expand beyond its original application. For example, the RWV bioreactor, used initially for transporting cells into space has been retooled by researchers for tissue engineering. Other NASA spinoffs include baby food, memory foam and scratch resistant lenses.

Although this dissertation is motivated first, by the need to understand the mechanisms of cell behavior and mechanotransduction in spaceflight, the techniques presented here may also be useful as a way to understand disuse atrophy in bed rest patients since tissue loss in astronauts is often considered analogous [16,65,66]. Moreover, CTM may offer tissue engineering researchers with the ability to understand morphogenesis and tissue development in real-time.

I am excited to introduce the techniques in this dissertation to the space biology community at large. The CTM system accommodates many chip

configurations to address a wide range of simulated microgravity investigations. It does not require any specific rotation speed, unlike conventional clinostats that must be rotated at an optimized RPM to balance sedimentation and centrifugal effects. I hope that CTM can reduce experimental variance and help the space biology community resolve some of the controversial findings common of simulated microgravity investigations.

Lastly, I demonstrate the use of a multi-passage, magnetically-clamped, miniature rotary joint for long-term cell culture. This technology is integral to the functionality of the CTM configuration presented. Aside from what is demonstrated in this dissertation, the same rotary joint could also enable a wide range of clinorotation experiments requiring the generation of complex, dynamic fluid microenvironments. Furthermore, the rotary joint could translate to potential applications in field-portable medical equipment and be integrated into microscale systems for *in situ* biochemical assays and separations.

2. Cell culture in microcavities *

For the informed design of microfluidic devices, it is important to understand transport phenomena at the microscale. This chapter outlines an analytically-driven approach to the design of rectangular microcavities extending perpendicular to a perfusion microchannel for applications that may include microfluidic cell culture devices. We present equations to estimate the transition from advection- to diffusion-dominant transport inside cavities as a function of the geometry and flow conditions. We also estimate the time required for molecules, such as nutrients or drugs, to travel from the microchannel to a given length into the cavity. These analytical predictions can facilitate the rational design of microfluidic devices to optimize and maintain long-term, low Peclet number environments with minimal fluid shear stress.

2.1. Background

Replenishing nutrients in traditional cell culture systems can potentially induce significant fluid shear not seen *in vivo*, disrupt intercellular signaling and cell-matrix interactions, and alter proliferation and migration behavior [67,68]. While microfluidics inherently has low Reynolds numbers, $Re=\rho vL/\mu$, guesswork or extensive simulations of different geometries and flow conditions are often needed to produce the desired microenvironment. To reduce design ambiguity, we derive equations to describe the mass and momentum transport in a microcavity extending

* portions of this chapter were published in:
Yew, A. G., Pinero, D., Hsieh, A. H., Atencia, J. (2013) Low Peclet number mass and momentum transport in microcavities. *Applied Physics Letters*, *102*(8), 084108.

perpendicular to a perfusion channel, which is the simplest microfluidic geometry considered for creating a diffusion-dominant region in the vicinity of cell cultures with continuous replenishment of nutrients and removal of cellular waste.

Of the various techniques used to establish low shear diffusion-dominant cell culture, microcavities are attractive since they can mimic *in vivo* environments, do not necessarily require complex barriers or membranes, consume relatively small quantities of culture media, and can help to precisely control fluid behavior [69,70].

2.2. Problem formulation

To estimate how cavity geometries could affect nearby cell cultures, we consider the case of flow past a rectangular cavity. Intuitively, a cavity extending perpendicular to the freestream flow will see diminishing advection velocities to a point where they become negligible relative to diffusion rates.

We derive an equation for the minimum length into a cavity where this occurs. While a very long cavity would mostly be diffusion-dominant, it may not be feasible since the time required to transport nutrients and waste can be prohibitive. Thus, we derive a simple model to predict the time required for molecules in the freestream to reach the bottom of the cavity.

Figure 8 shows a schematic of the problem formulation, where cells seeded at the bottom of a rectangular microcavity are exposed to a velocity field that decays along the cavity length, y. At a critical cavity length, y^* advection velocities become negligible compared to diffusive mass transport. To formulate the problem analytically, we evaluate the local Peclet number, Pe, at the center of the cavity (maximum velocity for a given cross section).

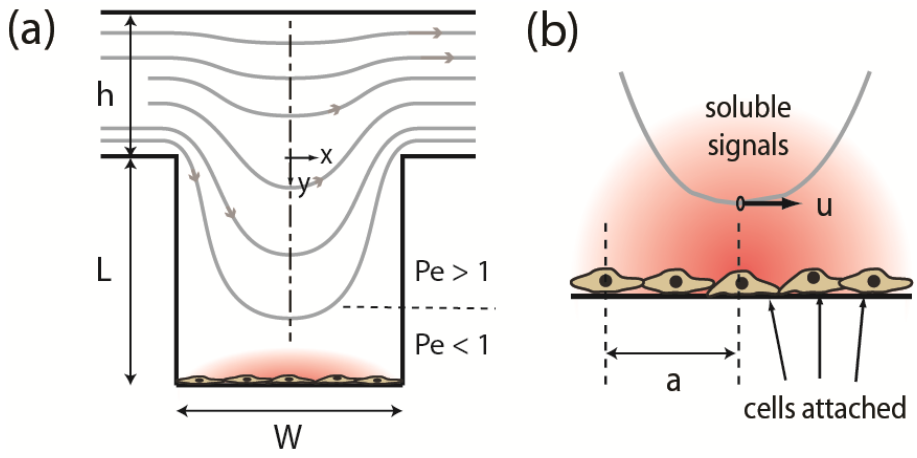

Figure 8. Problem formulation: cells attached to the bottom of a rectangular microcavity that is perpendicular to the freestream flow in a microchannel. (a) Intuitively, velocity decays as fluid flow enters the microcavity. At $Pe = 1$ advection velocities match rates of diffusion. The physiological range of flow conditions for many cell types occur at $Pe < 0.1$, where mass transport is diffusion-dominant. (b) With the proper geometrical design of microcavities, velocities near the vicinity of cultures should be sufficiently small, as calculated by *Pe* to ensure that soluble signals are able to travel some characteristic distance, *a* and are not removed.

The Peclet number,

$$Pe = u \cdot a \cdot D^{-1}, \tag{3}$$

relates the time it takes a particle moving with a velocity, u in the bulk flow to travel a characteristic length, a with the time it takes for that particle to diffuse the same length, where D is the diffusion constant. The transition between advection-dominant and diffusion-dominant mass transport occurs at approximately $Pe = 1$ and is decisively diffusive at $Pe \leq 0.1$.

As an example of how to use *Pe*, consider the diffusion of a small molecule, Stokes-Einstein radius ≈ 0.4 nm ($D \approx 7\text{x}10^{-10}\text{m}^2/\text{s}$) traveling $a = 50$ μm, roughly two

cell diameters. For a diffusion-dominant microenvironment, which is defined as $Pe = 0.1$, Eq. (3) yields a critical velocity of $u^* \leq 1$ μm/s. In order to satisfy this condition for u^* in microcavities, we need an explicit analytical equation relating the overall velocity field, u, to the length into a cavity. This will ultimately allow us to estimate the critical cavity length, y^* necessary for $u \leq u^*$.

2.3. Momentum transport

Initially, to determine an equation for the velocity decay inside cavities, we conducted a parametric study of cavity geometries and flow conditions. We tried a dozens of regression models to derive relevant correlations. Eventually, we noticed an important trend, shown in Fig. 9 where y^* depends, more than any other parameter, on the cavity width and the flow conditions in the perfusion channel. In the regression model, we assume that the velocity decay takes an exponential form, $u=u_D \exp(my)$.

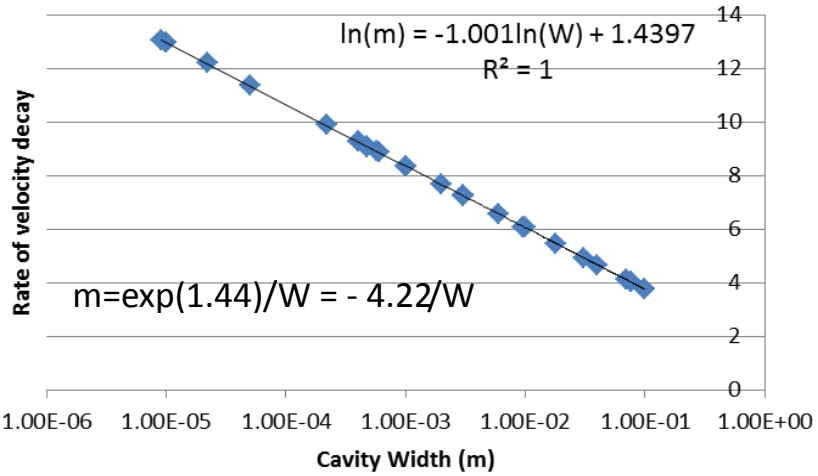

Figure 9. Regression model from parametric study used to predict critical length in microcavities yields, $m = \exp(1.44)/W = -4.22/W$, where m is the exponential constant for the exponential velocity decay. Substituting Eq (3) for u and m into $u=u_D \exp(my)$ yields $y^* = -W/4.22*\ln(Pe*D/u_D/a)$, which we later show to correlate well with the analytical solution.

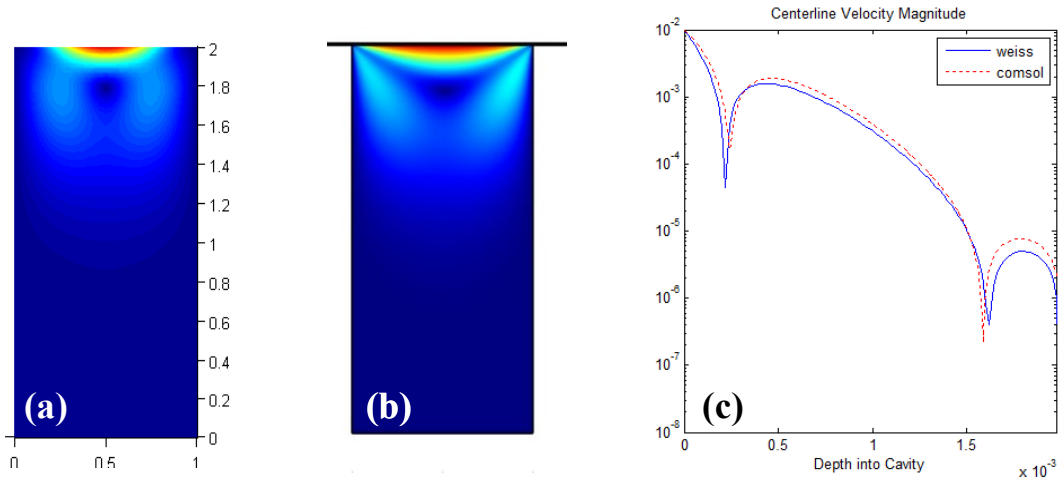

Figure 10. Graphical depiction of velocity fields in cavity flow. Matlab code in Appendix B. (a) velocity magnitudes from first-order Weiss-Florsheim solution; (b) velocity magnitudes COMSOL simulation with moving-lid boundary condition; (c) centerline velocities between Weiss-Florsheim and COMSOL solutions are rough in agreement.

As expected, y^* is a function of cavity geometries and flow conditions. For the analytical approximation, we simplified Weiss and Florsheim's solution [71] to the biharmonic equation that assumes low Reynolds number in the streamfunction-vorticity formulation of the Navier-Stokes equations. The full solution yields the velocity field shown in Fig. 10a, while a COMSOL simulation with a moving-lid boundary condition yields the one in Fig. 10b.

The analytical model is two dimensional in x and y and assumes infinite thickness ($z = \infty$). In our simplified solution, we: (i) consider only centerline velocities, which are approximately horizontal and maximum for a given depth; (ii) eliminate oscillatory terms to isolate the decay profile; and (iii) change the coordinate system origin to the top of the cavity as depicted in Fig. 8a. In detail, we begin with the stream-function representation,

$$\psi = \frac{u_D \sin^2(\pi x/W)}{a\varphi \sinh(bL)\cos(aL)}\left\{\frac{b}{a}\cosh(by)\sin(ay) - \sinh(by)\cos(ay) + \left[\frac{1-bz/a}{\tan(aL)}\right]\sinh(by)\sin(ay)\right\}$$

The horizontal velocity can be calculated from the stream-function as:

$$u = \frac{u_D \sin^2(\pi x/W)}{\varphi \sinh(bL)\cos(aL)}\sinh(by)\left\{\left[\frac{b^2}{a^2}+1\right]\sin(ay) + \left[\frac{1-bz/a}{\tan(aL)}\right]\left[\cos(ay) + \frac{b\sin(ay)}{a\tanh(ay)}\right]\right\}$$

Then, we eliminate oscillatory terms and consider only midline velocities to obtain,

$$u = u_D \frac{\sinh(by)}{\sinh(bL)}$$

Rewriting the hyperbolic signs in terms of exponentials yields,

$$u\left(e^{bL} - e^{-bL}\right) = u_D\left(e^{by} - e^{-by}\right)$$

$$\ln(u) + \ln\left(\frac{e^{2bL}-1}{e^{bL}}\right) = \ln(u_D) + \ln\left(\frac{e^{2by}-1}{e^{by}}\right)$$

The unit number is small relative to exponential terms and can approximated as,

$$\ln\left(\frac{u}{u_D}\right) \cong \ln\left(\frac{e^{2by}}{e^{by}}\right) - \ln\left(\frac{e^{2bL}}{e^{bL}}\right)$$

$$\ln\left(\frac{u}{u_D}\right) \cong b(y-L)$$

Rearranging the equation yields,

$$u \cong u_D e^{b(y-L)}$$

In the above equations,

$$\Phi = \left(1 + b^2 / a^2\right)\tan(aL) + \left(1 - b^2 z^2 / a^2\right)\left(1 / \tan(aL)\right)$$

$$z = \tan(aL) / \tanh(bL)$$

$$a = \frac{2\pi}{3^{0.25} W} \sin\left[\frac{1}{2}\tan^{-1}\left(\sqrt{2}\right)\right]$$

$$b = \frac{2\pi}{3^{0.25} W} \cos\left[\frac{1}{2}\tan^{-1}\left(\sqrt{2}\right)\right]$$

By applying a change of coordinates and substituting known terms, we then find that the field of horizontal velocity at the centerline is given by,

$$u = u_D \cdot \exp\left(-4.24 y / W\right), \tag{4}$$

where u_D is the maximum velocity at the top of the cavity, W is the width of the cavity and y is the length into the cavity. Conveniently, the velocity decay constant depends cavity length and width. Setting $Pe^* = u^* a/D$, substituting u^* for u into Eq. (4) and rearranging yields the critical cavity length,

$$y^* = \frac{-W}{4.24} \cdot \ln\left(\frac{Pe^* \cdot D}{u_D \cdot a}\right), \tag{5}$$

We used finite element analysis to verify that with increasing cavity thickness, 3D centerline velocities converged to the 2D solution in Eq. (4). However, for very thin cavities with low thickness-width aspect ratios, the velocity decay deviates from the analytical solution. Thus, Eq. (4) does not always represent a worst case in velocity decay as compared to the 3D simulations. Nonetheless, Eq. (5) still serves as a relatively useful approximation for practical cell culture applications that use a configuration similar to Fig. 8 with moderate to high thickness-width aspect ratios, and especially with ratios >1.

To experimentally validate Eq. (4), we measured fluid velocities in a microcavity device, which was fabricated by sandwiching layers of double-sided medical grade tape, AR8890 (Adhesives Research, Glen Rock) - with a perfusion channel and a microcavity cutout - between two standard glass microscope sides, per previously developed protocols [72]. The cavity dimensions were $W = 1$ mm, $L = 15$ mm, thickness $d = 200$ μm and main channel height $h = 500$ μm.

Latex particle standards, 10 μm-diameter (Beckman Coulter, Pasadena) were diluted in water and pumped into the perfusion channel at a flow rate of $Q = 500$ μL/hr. Because the particles auto-fluoresce, they appeared as streaks in pictures taken under a fluorescence microscope, Zeiss Axiovert 200 (Zeiss, Oberkochen) with 100 ms exposure at 470 nm excitation (Fig. 11a). The maximum velocity at the top of the cavity, $u_D = 1.2$ mm/s[24] (Re=0.24) was measured by dividing the length of the particle streak by the exposure time; additional measurements are plotted in Fig. 11b.

Qualitative observations of the flow field (Fig. 11a) were similar to those published extensively in literature [73-76], but were slightly different from the more plug-like flow we observed in finite element simulations. Nonetheless, the experimental centerline velocity distribution in the cavity agrees well with the theoretical decay from Eq. 4 as shown in Fig. 11b. From the previous example, the resulting value for $y^* = 1.5$ mm, given $D = 7\text{x}10^{-10}\text{m}^2/\text{s}$, $a = 50\ \mu\text{m}$, and $Pe^* = 0.1$ is calculated via Eq. (5), which indicates the critical length for diffusion-dominant flow.

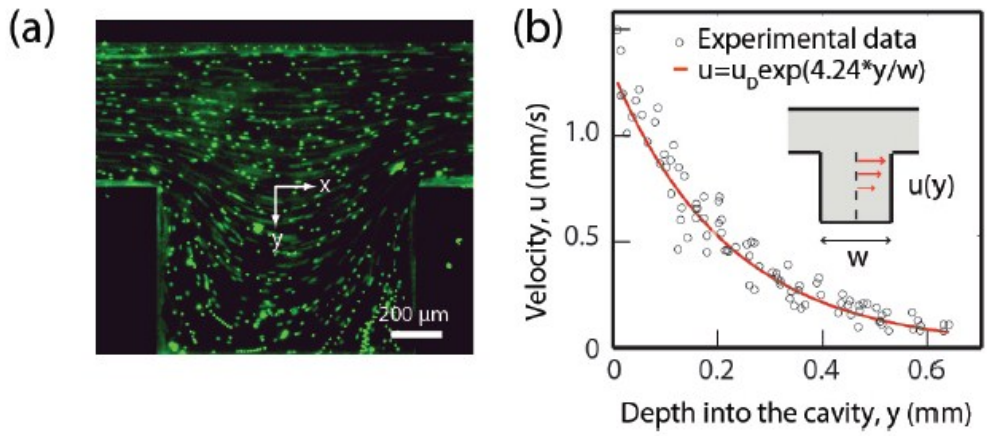

Figure 11. Experiments were used to validate the analytical model derived for predicting the velocity decay in microcavities. Tracer particles were sufficiently small (at least 10 times smaller than the smallest cavity dimension) and followed streamlines in the flow. (a) Images (5x objective, N.A. 0.13) of beads flowing at 500 μL/hr from a perfusion microchannel into a 1 mm wide cavity. The figure is a composite of nine independent pictures at 100 ms exposure. (b) Velocities in experiments were obtained by measuring streak lengths, where $n = 90$. Data points correlate well with the analytically-derived curve.

2.4. Mass transport

In order to assess the dynamics of mass transport from the perfusion channel to the cellular microenvironment in the cavity, we propose a simplified model of the transport process. In the model, we assume that molecules travel first, along a streamline to the centerline at maximum concentration primarily by advection t_a and second, from that position to the bottom of the cavity mainly by diffusion, t_d, (Fig. 12). The advection time is estimated by considering a molecule traveling from the entrance of the cavity to the centerline at length y as $t_a \approx (y^2+0.25W^2)^{1/2}/u(y)$, where substituting $u(y)$ with Eq. (4) yields,

$$t_a = u_D^{-1} \cdot \exp\left(4.24 y / W\right) \cdot \left(y^2 + 0.25 \cdot W^2\right)^{1/2}. \tag{6}$$

The estimated time required for molecules to travel from y to y^* by diffusion and accumulate to 89% of steady state concentration is,

$$t_d = \left(y^* - y\right)^2 D^{-1}. \tag{7}$$

To solve for the concentration at y^*, we estimated t_d in Eq. (5) using the solution provided by Crank et al (see Eq. 2.67, pp. 21-24 from [77]) for the case of a semi-infinite membrane that is suddenly subjected to $C=C_0$ on both sides. Because of symmetry, the solution in the center of the membrane is the same as in the bottom of the cavity (see Fig. 12).

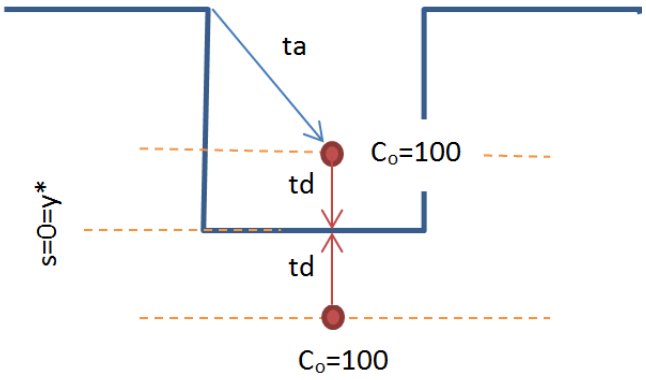

Figure 12. Model for diffusion used to determine diffusion time constants for cavity system. Solution was initially developed for the case of a semi-infinite membrane but is the same as the solution for the bottom of a cavity because of symmetry.

The solution is an infinite series that converges rapidly for large values of t, and therefore it can be simplified as:

$$C = C_0 - \frac{4C_0}{\pi}\exp\left(\frac{-D\pi^2 t}{4(y^*-y)^2}\right) \tag{8}$$

And therefore, for $Dt=(y^*-y)^2$, the concentration at y^* would be 0.89 of the steady state concentration, $C=0.89C_0$.

Since there are as many possible trajectories for nutrient delivery as streamlines into the cavity, the minimum time, t_c required to reach 89% of steady state concentration at y^* is given by the minimum time required to travel through any of the possible paths by advection and diffusion,

$$t_c = \min(t_a + t_d), \qquad 0 \le y \le y^*. \tag{9}$$

Eq. (9) does not have an explicit solution but can be solved using numerical methods, as depicted graphically in Fig. 13b for the transport of fluorescein inside a microcavity of length of $y^* = 1.5$ mm.

We experimentally verified our model for mass transport by first, fabricating a microcavity with dimensions shown in Fig. 13a, with thickness of $d = 200$ μm and then quantifying the evolution of the concentration profile of fluorescein we perfused into the cavity at a flow rate of $Q = 500$ μL/hr. Time-lapsed images with 10 s intervals and 860 ms exposure at 470 nm excitation were acquired with the Zeiss microscope and quantification was determined by measuring the average pixel intensity of a 0.5 mm wide by 0.05 mm tall region at the bottom of the cavity. The experimental steady state value of $t_c = 4.0$ min shown in Fig. 13c agrees relatively well with the prediction of 5.0 min. Equation (9) can also be used to estimate the time for the delivery of a drug or for removing waste products secreted by cells.

2.5. Discussion

Additional values for y^* and the corresponding t_c are tabulated in Table 2 for typical flow conditions and geometries used in microfluidics. To determine if conditions at these values of y^* are physiological for diffusion-dominated, interstitial flow, we estimated the shear stresses from Eq. (4) using the relation, $\tau = \mu(\partial u/\partial y)$. Resulting stresses are physiologically-relevant to stresses expected in interstitial flow [78-79].

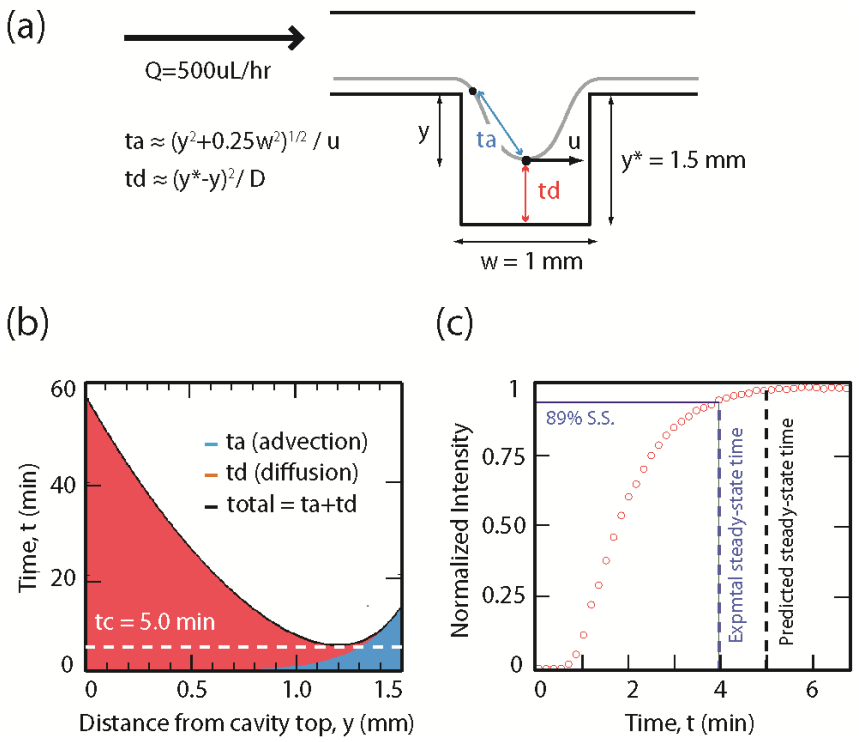

Figure 13. Experiments of nutrient delivery in microcavities using fluorescein as a representative small molecule to validate Eq. (9). (a) Illustration of the model used to estimate the time required for small molecules to reach cells at y^* from the perfusion channel. The model assumes that first, molecules travel only by advection to the centerline of the cavity, and then only by diffusion to the bottom; the total time for the mass transport through any streamline trajectory can be calculated by adding both contributions. (b) The minimum time required for nutrients to migrate from the freestream to y^* through any possible path is predicted to be $t_c = 5.0$ min based on Eq. (9). At this minimum, nutrients would travel roughly 1.2 mm by advection and 0.3 mm by diffusion to reach y^* and would roughly reach steady state concentration. (c) For validation, fluorescence intensity at y^* was measured at 10s intervals with 860 ms exposure and 450 nm excitation. In rough agreement with our prediction of 5.0 min, the experimental intensity reached 89% of the steady state value at 4.0 min.

In summary, we derived an equation to predict the transition from advection- to diffusion-dominant regions in a microcavity, which can be used to design devices mimicking *in vivo* diffusion-dominant microenvironments for cell culture. We also derived the time needed to obtain 89% of steady-state concentration of nutrients in

the system. Shear stress approximations show that transport conditions in microcavities in the vicinity of cell cultures are similar to physiological behavior of the interstitial flows. Aside from their ability to predict shear stresses, our equations can be used to target specific values of *Pe*. For example, Aroesty and Gross (1970) have predicted Peclet numbers in blood plasma microcirculation *in vivo* [80].

Both of the momentum and mass transport equations can be used for the rational design of microcavities for cell culture under diffusion-dominant conditions. Microcavities and similar structures are simple to fabricate, with potential applications beyond cell culture, including protein crystallization and conditions that require stagnant flow with continuous replenishment of soluble chemicals.

One of the limitations in this work is the ability to accurately predict the velocity field in the perfusion channel in the vicinity of the cavity. The work that we've demonstrated assumes that we know u_D *a priori*. Since the velocity at the top of the cavity is not easily determined, a conservative value for u_D, equaling the maximum freestream velocity can be calculated by assuming the Hagen-Poiseuille profile and using standard microfluidics equations for channel resistance [81]. Doing so provides a reasonable estimate for the velocity decay in plug flows and a conservative estimate in fully-developed flows. Another limitation is that large recirculation regions in cavity flow may deviate slightly from our predictions of both advective and diffusive mass transport.

In this dissertation, the use of our analytical equations provides a way to design lab-on-chip devices for producing low-shear, diffusion-dominant cell cultures while also providing a way to predict mass transport from a perfusion channel to cell

cultures at the bottom of a microcavity. These analytical tools are an exciting improvement over conventional culture techniques that cannot guarantee precise regulation of microscale flow. In the same way, cells cultured in clinostats, either for microgravity simulation or for tissue engineering research cannot offer control of fluid shear or nutrient delivery in the same way as our analytical approach. To enable the use of lab-on-chip technologies for clinostat experiments, a method of microgravity simulation is required. This is the focus of Chapter 3.

Table 2. Estimation of the cavity length required to generate a diffusion dominant microenvironment for a given velocity at the top of the cavity, u_D and a cavity width, W using Eq. (4,5). The value of t_c estimates the time for the concentration of molecules at the bottom of the cavity to reach 89% of steady state. All the values where calculated for fluorescein, where $Pe^* = 0.1$, $D = 7\text{x}10^{-10}$ m^2/s, and $a = 50\mu$m. Corresponding shear stresses, τ are physiological for interstitial flow.

W(mm)	u_D(mm/s)	y^*(mm)	t_c(min)	τ(Pa)
0.2	1	0.310	0.540	0.021
0.5	1	0.775	2.270	0.008
1.0	1	1.550	6.420	0.004
0.2	5	0.386	0.600	0.106
0.5	5	0.965	2.560	0.042
1.0	5	1.923	7.310	0.021
0.2	10	0.419	0.630	0.212
0.5	10	1.046	2.680	0.085
1.0	10	2.092	7.660	0.042

3. CTM technology **

Cells in microgravity are subject to mechanical unloading and changes to the surrounding chemical environment. How these factors jointly influence cellular function is not well understood. Our focus is to elucidate their role using ground-based analogues to spaceflight, where mechanical unloading is simulated through the time-averaged nullification of gravity.

The prevailing method for cellular microgravity simulation is to use fluid-filled containers called clinostats. However, conventional clinostats are not designed for temporally tracking cell response, nor are they able to establish complex fluid environments. To address these needs, we developed a clinorotation time-lapse microscopy (CTM) system that accommodates lab-on-chip cell culture devices for visualizing time-dependent alterations to cellular behavior.

3.1. Background

The National Aeronautics and Space Administration (NASA), European Space Agency (ESA), and other organizations manage a robust portfolio of research initiatives for space biology, using the International Space Station (ISS) as their flagship facility. However, the ISS is not easily accessible and does not often accommodate continuous monitoring of onboard experiments, thereby limiting the ability to observe time-evolving processes. While ground-based methods of simulated

** portions of this chapter are being considered for publication:
Yew, A. G., Chinn, B., Atencia, J., Hsieh, A. H. (in preparation) Lab-on-chip clinorotation system for live-cell microscopy under simulated microgravity. *Acta Astronautica.*

microgravity with conventional clinostats are notably less expensive, they also preclude the possibility of real-time cell monitoring. Thus, state-of-the-art methods do not easily allow time-dependent investigations to identify the mechanisms of cellular alterations and consequently, may lead to an incomplete understanding of how microgravity affects human health.

A brute-force remedy for this latent need is to incorporate a full-scale microscope onto a mega-scale clinorotation platform for ground simulations. Clinorotation was initially developed for studying how plants respond to gravity and is currently the prevailing method for cellular microgravity simulation. It is based on the assumption that a time-averaged nullification of gravity can be achieved by reorienting the gravity vector on biological samples, and that the reorientation is fast enough to ensure that specimens cannot perceive a gravitational bias in any direction. The ESA's clinostat microscope [82] is an example of one mega-scale configuration. Another example was published in 2010 by Pache et. al. [83] and was optimized in 2012 by Toy et. al. [84] to demonstrate how digital holographic microscopy (DHM) with mega-scale clinorotation can monitor cytoskeletal changes in simulated microgravity. Interestingly, these studies showed the first published, same-cell images exhibiting time-dependent lamellipodium retraction, filopodia extension, and perinuclear actin accumulation under clinorotation compared to static controls.

3.2. Clinochip platform for CTM

Even though the clinostat microscope and CR-DHM can be used for time-lapse microscopy, many labs do not have the resources or facility space to incorporate a mega-scale system. Furthermore, mega-scale systems could induce significant

mechanical vibrations that may disturb cell cultures. Therefore, we present a clinochip system for clinorotation time-lapse microscopy (CTM) that may also enable long-term, low shear cell culture. While the underlying principles of the clinochip are identical to conventional clinostats, CTM enables live-cell imaging, without prohibitively large equipment or disruption of culture environments. Importantly, clinochips under CTM represent a significant step forward in space biology research because it is an affordable, size-manageable system that enables microgravity studies of not only traditional endpoint outcomes, but also dynamic cellular processes.

Moreover, CTM is compatible with any lab-on-chip device assembled on a standard microscope slide, for example: microcavites for cell culture; chemical gradient generators; cell sorters; and capillary-based separation columns. It can accommodate cells in monolayer, suspension, and 3D constructs.

We provide a preliminary demonstration of how CTM makes long-term culture feasible by integrating lab-on-chips with a miniature rotary union for programmable media exchange, continuous media circulation, and chemical infusions. Taken together, the enormous scope of possible microgravity investigations distinguishes clinochips from conventional clinostats. We believe that their affordability, easy implementation, and amenability for live-cell imaging will fully-enable researchers seeking to understand the time-evolution of cellular alterations under microgravity simulation.

We fabricated a clinochip system that enables simultaneous imaging of cells subjected to two-dimensional microgravity simulation and of cells in static control. The CTM configuration depicted in Fig. 14a uses a stepper motor with a resolution of

200 macrosteps per revolution and a two-gear train assembly to transfer rotational motion to a platform that holds a lab-on-chip device. This rotating platform pivots on a custom-built miniature PTFE rotary joint that allows one rotational degree of freedom about the spin axis. Additionally, the rotary joint is equipped to manage fluid exchange between external fluid reservoirs and devices on the rotating platform.

Based on the design of CTM shown in Fig. 14, cells on the clinochip are 1 mm from the top of the platform. The center of the top of the platform is 1 mm from the axis of rotation. Therefore, according to the equation $a_c=\omega^2 r$, where a_c is the centripetal acceleration, ω is the angular velocity in rad/s, and r is the distance away from the axis of rotation, the minimum centripetal acceleration that cells are exposed to at 60 RPM is 0.08 m/s^2, which is 8x10^{-3} g's. This "artificial gravity" can be eliminated by asymmetrically redesigning the platform such that the expected location of cells would align with the axis of rotation.

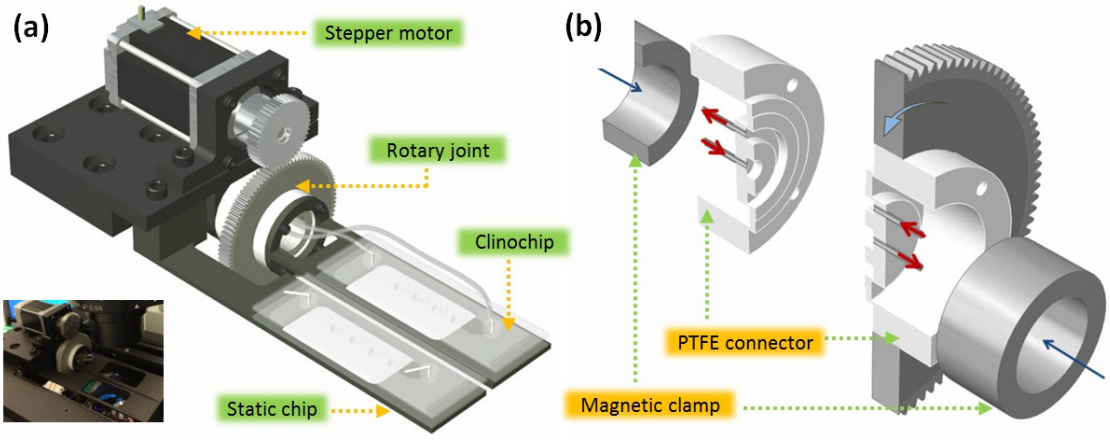

Figure 14. Microscope stage-amenable, clinorotation timelapse microscopy (CTM) system enables live-cell imaging of cells. Matlab code in Appendix C. (a) CTM components include a clinochip for simulated microgravity and static chip for a 1-g static control. (b) exploded computer model of rotary union designed to allow media perfusion into clinochips for long-term cell culture.

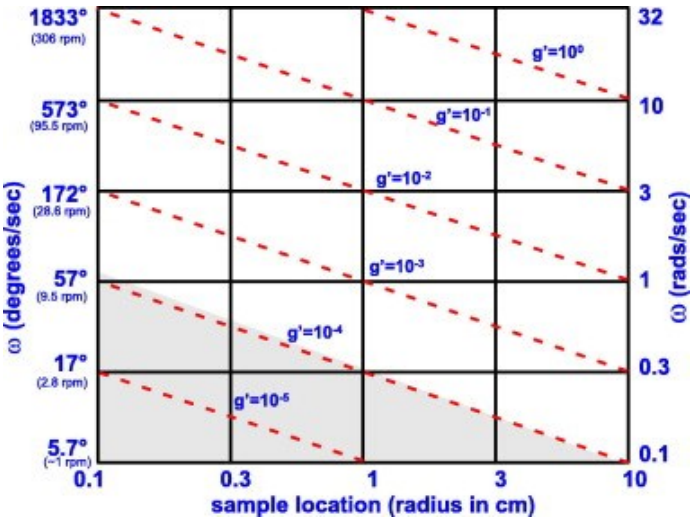

Figure 15. Residual gravity on a particle in conventional clinostats for various clinorotation speeds and distances away from axis of rotation. Shaded area represents the most appropriate regime for microgravity simulation. Reproduced from [85].

For cells that are not at the midline of the clinochip platform – for example, cells at the edges of a large culture cavity – the residual gravity would be greater. Moreover, this residual gravity is proportional to the square of the rotation speed. Therefore, we advise researchers to design clinochips that take these factors into consideration and if possible, keep cells at the clinochip midline and to use as slow a speed as possible. However, when CTM is compared with conventional clinostats, the residual gravity with CTM is much lower (see Fig. 15).

3.3. Magnetically-clamped rotary joint

In brief (refer to Fig. 14b), the rotary joint was fabricated with 19-guage blunt syringe needle tips that were press fitted from the rear of CNC-milled PTFE connectors into 1 mm access holes until flush with the microchannel groves on the front. Axially self-aligning neodymium ring magnets (RC86, K&J Magnetics) were pressed into slots at

the rear of the connectors and provide substantial clamping force when mating two identical connectors. Commonly used as a material for gaskets, PTFE has some unique properties that also make it suitable for the rotary joint: 1) high compressibility forms a tighter seal at the mating interface; 2) hydrophobicity helps to prevent fluid wetting and leakage at the interface; 3) low coefficient of friction allows for easy rotation about the spin axis.

The selection of motor to drive the clinochip platform depends on the friction forces encountered in the system. The expected friction forces occur primarily at the mating interface of the rotary joint that helps to form a seal. Based on the geometry of the interface shown in Fig. 16, the total area A_T=130 mm^2. With a clamping force of approximately F_C = 70 N and a worst-case coefficient of friction of μ_f =0.1,

$$p_n = \frac{F_c}{A_T} = \frac{70\ \text{N}}{130\ \text{mm}^2}$$

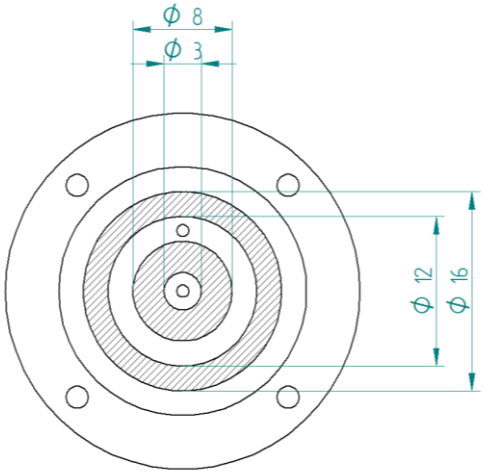

Figure 16. Rotary joint, dimensions of mating interface. We use these values to calculate the required torque for sizing the motor.

And the required torque can be calculated as,

$$T = \int_0^{r_p} \int_0^{2\pi} \mu_f p_n r^2 d\theta dr$$

$$T = 0.05\left(\int_{1.5}^{4} \int_0^{2\pi} r^2 d\theta dr + \int_6^8 \int_0^{2\pi} r^2 d\theta dr \right)$$
$$= 0.1\pi\left(\int_{1.5}^{4} r^2 dr + \int_6^8 r^2 dr \right)$$

$$T = 0.1\pi \frac{1}{3}[4^3 - 1.5^3 + 8^3 - 6^3]$$

Therefore, we calculated a minimum required torque of 38 N-mm, which is the minimum output that a motor needs in order to rotate the clinochip platform.

To analyze the quality of the seal formed at the mating interface of the rotary joint and to attempt to predict the leak rate, we first used a profilometer (Tencor TP-20, AlphaStep 200) to obtain a scan of the surface topology, as shown in Fig. 17. The profilometer is a contact-based system that drags a stylus across the sample being scanned. From the profilometer data, we obtained a histogram of surface heights (Fig. 18), which showed a non-Gaussian distribution. Surface heights were skewed toward higher values, which we attributed to machining processes and Teflon wear from having operated the rotary joint repeatedly.

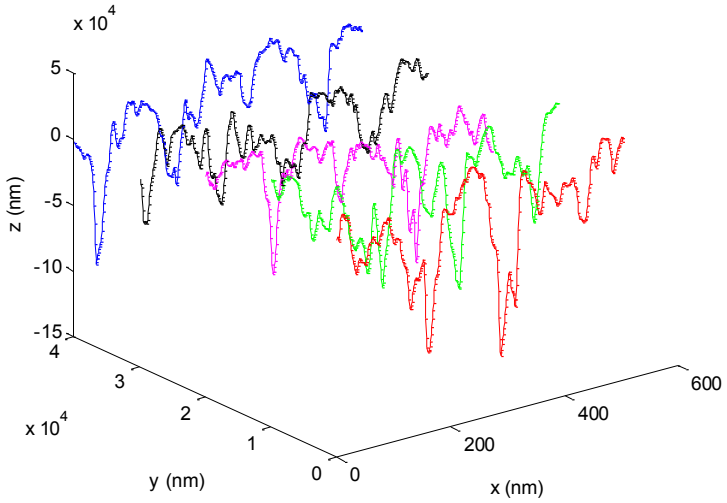

Figure 17. Profilometer surface scan of mating interface on rotary joint. A total of five line scans were performed with a resolution of 2 microns.

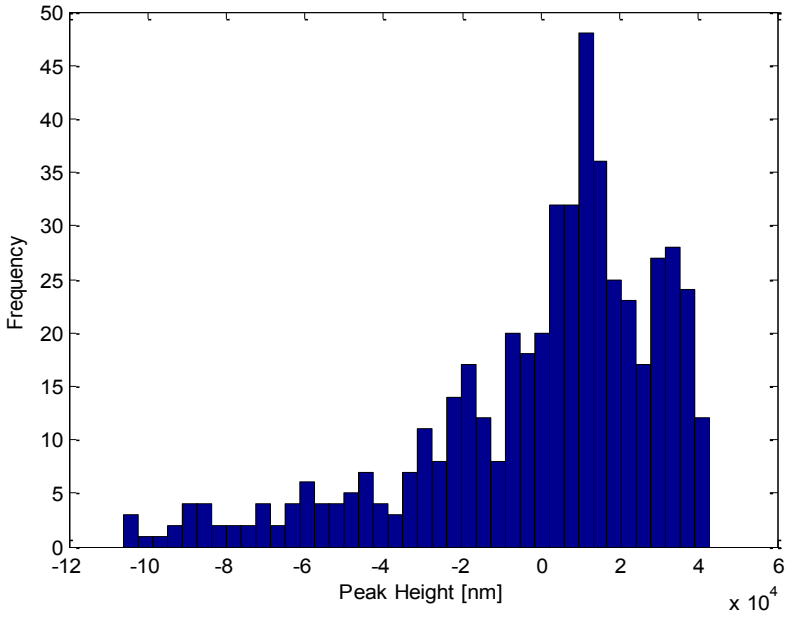

Figure 18. Histogram of asperity heights from one profilometer linescan. Non-Gaussian distribution is skewed toward larger values that may indicate that machining processes, plastic deformation, and Teflon wear produces a flatter interface.

We also briefly looked at various theories for predicting the leak rate at the interface of the rotary joint [86-88]. Determining the nominal separation gap between two contacting surfaces is an active area of research in contact mechanics. The Hertzian model is a classical formulation for contact deformations between various shapes. Greenwood [89] and others have expanded Hertzian contact to consider non-spherical shapes and multiple asperities [90-92].

More recently, Persson et al. and others have considered a fractal approach that is applicable for self-affine surfaces [93-95]. While these models are informative, we agree with many in the field that gasket theory remains a "black art" in the sense that it is not uncommon to use empirical "fudge factors". In fact, manufacturers often publish standards that are based on empirical formulations rather than pure theory.

We think that existing theories for predicting leak rates are inadequate because they do not account for surface effects, e.g. hydrophobicity. Teflon gaskets, for example, would be highly hydrophobic and capillary forces between mating surfaces may be sufficient to keep liquids from leaking. However, gasket theory has traditionally been formulated for gases, rather than liquids; therefore, capillary effects are understandably, not as relevant in these established theories.

Therefore, we think that the development of more accurate models for leak rates would be an interesting research avenue that could yield cross-cutting applications. However, it is beyond the scope of this dissertation.

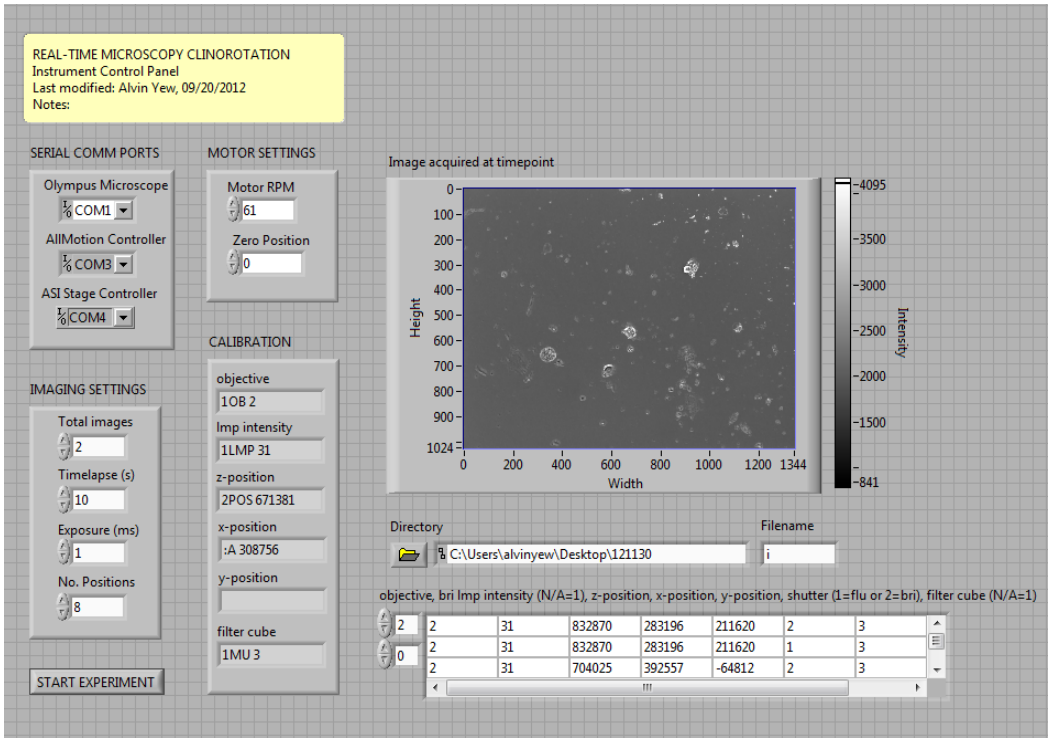

Figure 19. LabVIEW GUI for open loop control system with input parameters for the stepper motor, microscope, XY motorized stage, and camera. Matlab code in Appendix D.

3.4. Open loop control system

Open-loop control for CTM is established with LabVIEW (v.10.0, National Instruments) for the stepper motor (HT11-013D, Applied Motion Products), inverted fluorescence microscope (IX81, Olympus Corporation), XY motorized stage (MS-2000, Applied Scientific Instrumentation), and B/W CCD digital camera (ORCA-ER, Hamamatsu Photonics). To establish appropriate communication with the various devices, we used RS-232 protocols for the stepper motor, microscope, and XY motorized stage. We used IEEE 1394 protocols to communicate with the microscope. The graphical user interface (GUI) developed in LabVIEW is shown in Fig. 19.

3.5. Clinochip filter

After conducting several live-cell experiments with continuous media circulation, we noticed that debris would accumulate in some clinochip configurations. While we initially attributed the debris to cell waste, it soon became apparent that the debris came from an external source. Furthermore, the debris was only present in the clinorotated samples and not in the static control. Therefore, we concluded that debris was being generated by the rotary joint, either by PTFE wear, by dried media at the interface that was caking and reentering into the flow stream, or both.

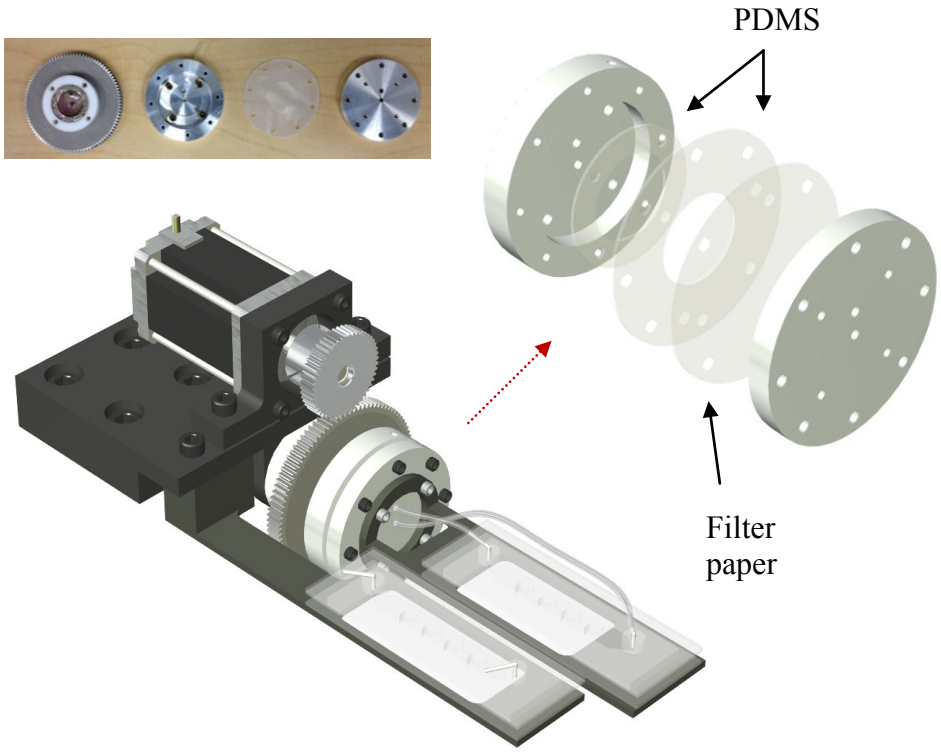

Figure 20. Filter system designed to be integrated onto the clinochip platform. Gaskets are constructed out of PDMS. Filter paper is used to strain debris. We tested our filter with a 10 micron pore size cell filter paper and found that it was effective in removing some of the debris. However, we require additional optimization.

External debris is a nuisance for imaging, as it detracts from being able to accurately identify cell boundaries. However, what's more disconcerting about debris is that they may introduce experimental artifacts in clinorotated samples that cannot be accounted for in static controls. Therefore, we have designed a filter system that can be integrated into the CTM system, see Fig. 20. The actual filter element is fabricated out of cellular-grade filter paper, and gaskets are made out of PDMS sheets. We tested the filter with cells cultured under clinorotation and found that it was successful in removing some amount of debris, but requires additional optimization to improve its efficacy.

3.6. Discussion

Clinorotation time-lapse microscopy enables a wide range of scientific investigations without the complicated optimization procedures needed to balance centrifugal and gravitational forces in conventional clinostats. Moreover, the possibility of performing real-time assays with CTM addresses a latent need in microgravity research. With CTM, we have the unique ability to investigate live-cell response in simulated microgravity with established methods that are typically used in traditional 1-g techniques, such as microscopy.

While CTM is a powerful tool for space biologists, the design that we've presented can only be used to simulate microgravity in 2D, i.e. one axis of rotation. Although this is not considered a major hurdle in microgravity research, as other investigators still use 2D clinostats, 3D microgravity simulation (two-axes of rotation) through random positioning machines is considered a superior model for microgravity. In order to achieve 3D clinorotation on a microscope stage-amenable

platform, clinochip devices would need to be significantly reduced in size. Also, a completely new type of rotary joint would need to be designed to accommodate the additional axis of rotation.

4. Live cell assays using CTM **

Multipotent mesenchymal stem cells (MSCs) are intimately involved in human health. They are responsible for tissue growth during development, help maintain homeostasis in mature tissues, and may be used for therapeutic treatments of bone, skeletal muscles, and other mesodermal tissues [96-98]. Soluble factors and mechanical stimulation jointly modulate lineage commitment; however, perturbations in spaceflight can change a cell's environmental cues [99,100] and hence, influence physiologic processes, such as inhibiting osteogenesis [101-103]. We hypothesize that such changes arise from altered cell-cell interactions and chemotactic behaviors brought about by morphologies and cytoarchitectures adopted during microgravity.

4.1. Introduction

MSCs are cellular precursors for mesenchymal components that normally migrate to injury zones and differentiate [104-107], ultimately producing tissues such as bone or fat, depending on chemical and cytoarchitectural cues. This was shown in previous studies that used patterned substrates to produce rounded MSC morphologies, which limited their osteogenic potential in the presence of growth factors [108]. These alterations may affect motility and change the spatial interaction between cells, which is important for example, because osteogenesis is favored at low MSC densities, while high densities prohibit spreading and lead to adipogenesis.

** portions of this chapter are being considered for publication:
Yew, A. G., Chinn, B., Atencia, J., Hsieh, A. H. (in preparation) Lab-on-chip clinorotation system for live-cell microscopy under simulated microgravity. *Acta Astronautica.*

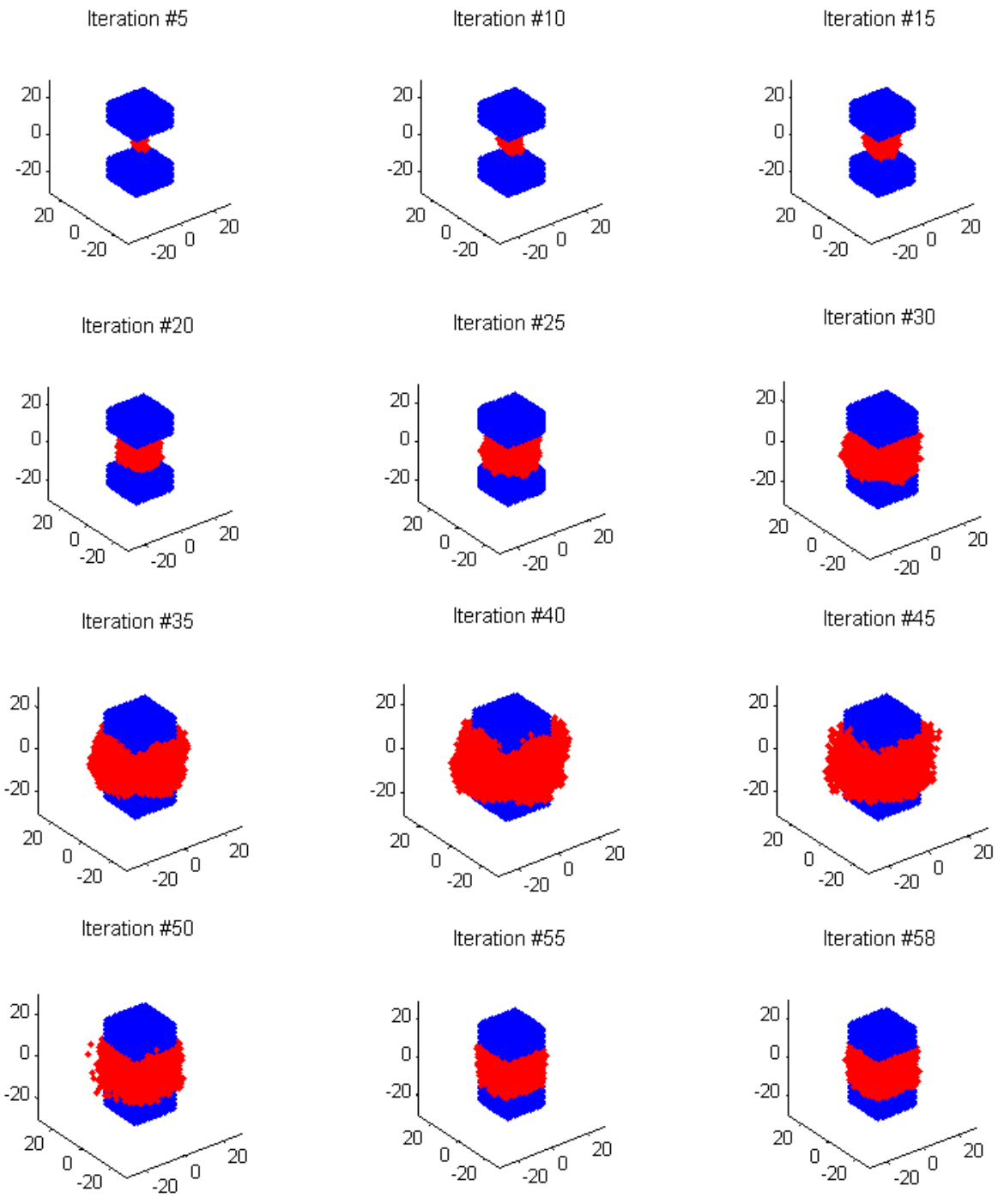

Figure 21. Three-dimensional simulation of the formation of callus (red) between the original bony fragments (blue). Original cells at fracture site consist entirely of hMSCs.

Investigations under NASA NNJ04HB27G showed that simulated microgravity disrupts MSC function by enhancing adipogenesis and reducing osteoblastogenesis [50,51]. We hypothesize that microgravity-induced morphological alterations could be the primary cause of these disruptions and are also responsible for the markedly lower rates of differentiation observed in stem cells flown during NASA NNH08ZTT003N [109]. At the tissue-level, excessive adiposity may disrupt normal bone metabolism, a hypothesis currently being investigated by researchers under NASA NNX12AL24G.

We performed preliminary work [24] on simulating how MSCs may contribute to bone fracture healing during cyclic loading (see Fig. 21). The motivation behind these simulations was to show the importance of time- and load-dependent processes. In brief, a three-dimensional, anisotropic random walk model with an adaptive finite element domain was developed for studying the entire course of fracture healing. Our simulation improves on existing models that do not consider the changing callus morphology and probabilistic behavior of biological systems.

Although we did not specifically simulate the microgravity condition, we found that cell population was directly proportional to the load magnitude. Fibrous tissue formation constitutes much of the increase in overall cell population. Cartilage tissue formation showed a time response that also depended on load magnitude. The growth and remodeling of the bone matrix through osteoblasts displayed behavior typical of step responses for second-order control systems with various degrees of damping. Increasing the load magnitude for the fracture healing protocols appeared to be analogous to increasing the damping ratios in a control system.

4.2. Methods

4.2.1. Optimizing cell culture protocols

One challenge that we faced was determining the optimum treatment for glass surfaces to facilitate cell adhesion and spreading. We initially considered several configurations: bare glass, poly-l-lysine, fibronectin, and a double coat of poly-l-lysine + fibronectin (see Fig. 22). We found that bare glass (Fig. 22a) and poly-l-lysine (Fig. 22b) treatment were not effective at promoting cell adhesion, as cells at 24 hr incubation were easily flushed away after gentle agitation. Surfaces containing fibronectin treatment (Fig. 22c,d) showed healthy spreading after 24 hr incubation. Because the double-coating did not appear to add any benefit to cell spreading, we decided to further optimize a single coating of fibronectin.

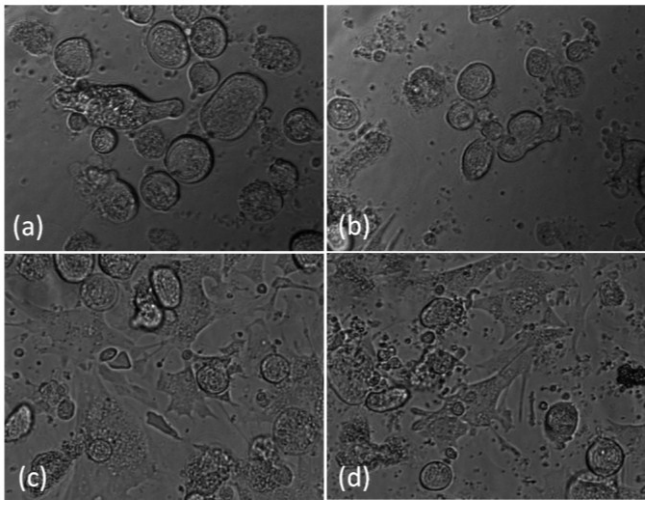

Figure 22. We considered various surface coatings to optimize cell spreading, demonstrated here with DIC images of P5 hMSCs after 24 hr incubation. All glass surfaces were initially cleaned with acetone, rinsed with DI water, cleaned with ethanol, rinsed with DI water, and then air-dried. a) bare glass. b) treated with poly-l-lysine at 0.01% (w/v) in PBS for 5 min prior to cell seeding. c) treated with 20 ug/mL fibronectin in PBS for 1 hr prior to cell seeding. d) treated with poly-l-lysine followed by fibronectin.

To minimize the possibility of cells "sinking" into a fibronectin substrate, which may affect the investigative quality of our experiments, we examined cells cultured under various concentrations of fibronectin treatments. Typical protocols call for concentrations of 0.1 to 100 ug/mL incubated for 1 hr, but we tested for concentrations at 5, 10, 15, and 20 ug/mL. We found that cell spreading was marginally reduced at 5- and 10 ug/mL concentrations while 15- and 20 ug/mL concentrations were approximately the same.

4.2.2. hMSCs without perfusion

Live-cell CTM devices were fabricated using a high-frequency corona treater (BD-20AC, Electrotechnic Products) to energetically bond layers of polydimethylsiloxane (Sylgard 184, Dow Corning), i.e. PDMS at 10:1 ratio of base to curing agent, between 75x25x1 mm glass slides. Geometric features in PDMS were formed by a high-resolution razor cutter (FC8000, Graphtec). To prepare microfluidic devices for experiments, cell culture surfaces, consisting of a 200 micron tall by 1 mm wide microchannel constructed from PDMS and glass, were cleaned with 70% ethanol, rinsed in deionized water, and air-dried.

Immediately before cell experiments, the entire microchannel was incubated in ambient for one hour with 15 ug/mL fibronectin (354008, BD Sciences) in phosphate buffer saline (PBS) without Ca++ and Mg++ and then gently rinsed with 2-3 times with PBS. Fibronectin-treated surfaces were kept hydrated by filling culture cavities with fresh PBS and were sterilized by ultraviolet exposure for at least 15 m prior to cell seeding.

Passage-5 hMSCs were expanded in 6-well plates with MSC media until confluent. Stem cells were trypsinized, centrifuged, resuspended at 10^5 cells/mL, plated into microchannels, and incubated in a microscope-amenable environmental chamber (Precision Plastics) at 37 ºC, 50% humidity, and 5% CO_2 for 20 min before microchannels were gently flushed with MSC media to remove non-adherent cells. One clinochip and one static chip were placed onto the CTM system, which was mounted to an XY motorized stage (MS-2000, Applied Scientific Instrumentation) on an inverted fluorescence microscope (IX81, Olympus Corporation).

Cells that had been seeded on both the clino- and static chip were randomly selected for time-lapse microscopy using DIC and phase contrast. Both chips had similar seeding densities, roughly 5-6 cells in the field of view using a 10X objective, and similar initial morphologies. Before subjecting the clinochip to 30- or 60 RPM clinorotation, we acquired cell images at 0 hrs. At each subsequent hour, for 8 hrs, we acquired additional images.

4.2.3. hMSCs with perfusion

The main objective of this experiment was to demonstrate the use of the rotary joint for long-term cell culture under clinorotation. In brief, the methods discussed here are similar to section 4.2.1, with the exception that: (1) cells were cultured in cavities (see Fig. 23) rather than microchannels; (2) cells were subjected to clinorotation after 24 hr incubation rather than the roughly 30 min in section 4.2.1; (3) media was circulated through cavities at the critical flow rate, per Eq. (5).

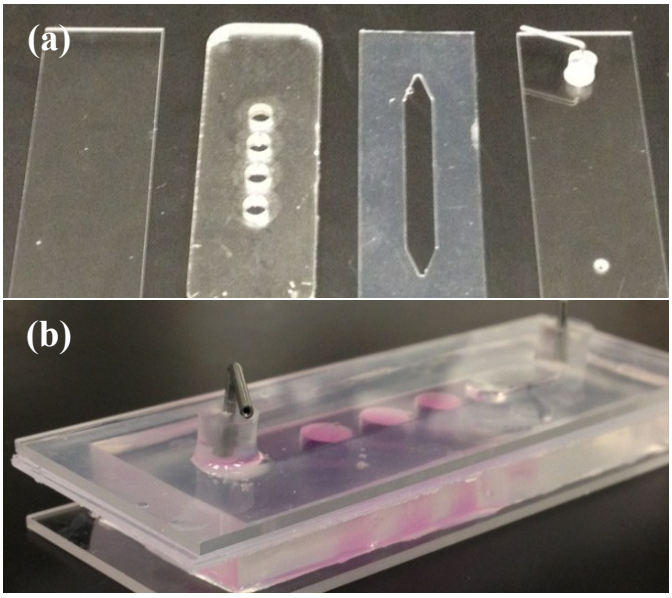

Figure 23. Lab-on-chip devices used for cell experiment 2. (a) device layers were energetically-bonded with corona treatment. (b) full-assembled device.

In detail, we again used a high-frequency corona treater to energetically bond layers of PDMS at 10:1 ratio of base to curing agent, between 75x25x1 mm glass slides. Geometric features in PDMS were formed from PTFE molds or by a high-resolution razor cutter. To provide media perfusion through the PDMS microchannels and into cell culture cavities, we used syringe pump infusion (Pump 11 Elite, Harvard Apparatus) of media through 1.5 mm diameter orifices in glass slides. Orifices were created with a micro-sandblaster (Model 6500, S.S. White Technologies Inc.).

To prepare microfluidic devices for cell culture, surfaces were cleaned and incubated with 15 ug/mL fibronectin in PBS. Passage-4 hMSCs were expanded until confluent in tissue culture polystyrene flasks with MSC media, then trypsinized, re-suspended at 10^5 cells/mL, and seeded into clinochip and static chip microcavities with MSC media. After 24 hr incubation in microcavities, the clinochip was set to

rotate at 60 RPM and the static chip at 0 RPM. Dual syringe pump infusion into both chips was set at a flow rate of 0.5 mL/hr to allow continuous media circulation in devices. Time-lapse images were acquired at 10 m intervals.

4.2.4. HEK293 with perfusion

We used CTM on cultures other than hMSCs and chose to use HEK 293. Methods are similar to those described previously (i.e. PDMS/glass device construction cell culture protocols, continuous perfusion with pump). However, a major difference is that we did not use same-cell images; therefore, the images that we acquired represented typical morphologies for the conditions described.

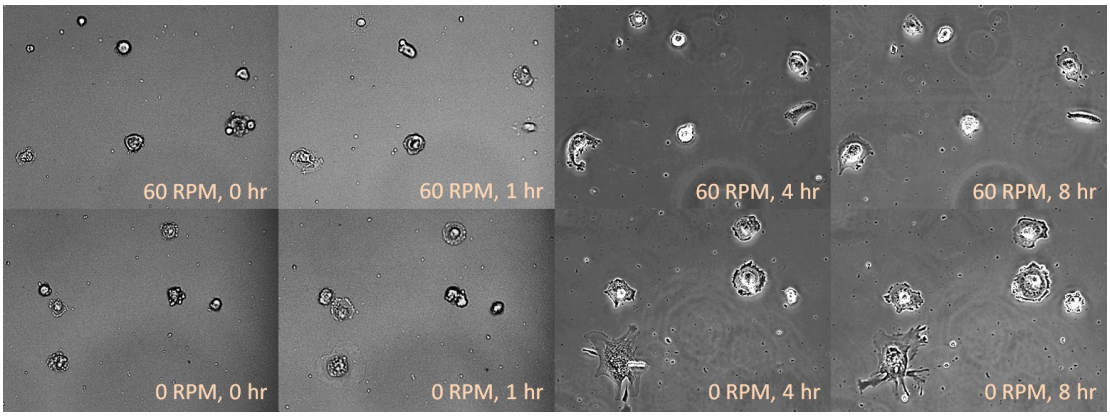

Figure 24. Time-evolution of early spreading in hMSCs, without perfusion, imaged under DIC and phase contrast at 60 RPM clinorotation and at 0 RPM static control. While initial morphologies for all cells were similar, cells at 0 RPM were qualitatively more spread at 4-8 hrs compared to 60 RPM. This may indicate that microgravity inhibits cell growth.

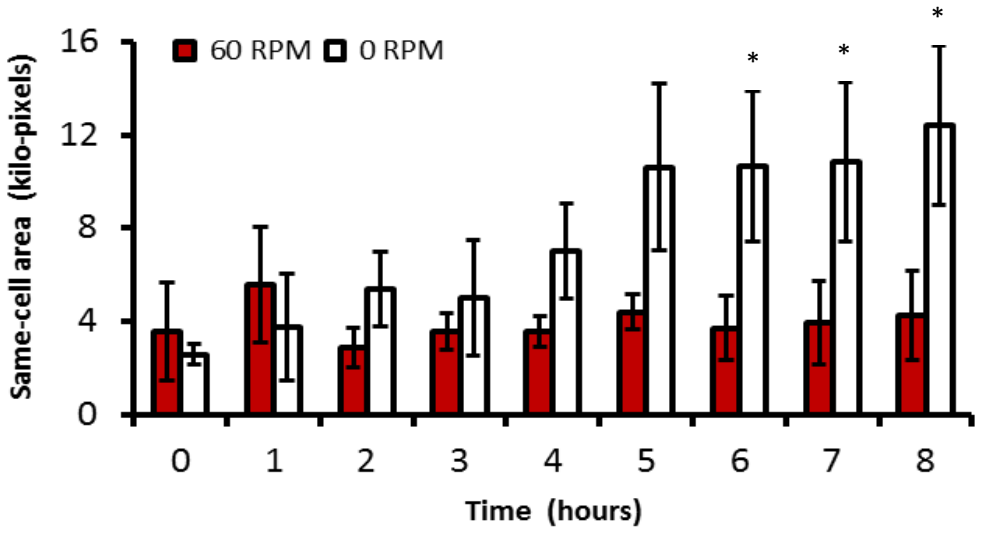

Figure 25. Mean values of same-cell areas (n=3) and 1 S.D. error bars. From calculated cell areas at 8 hrs (based on images from Fig. 24), cells with the three median values were digitally-tagged. To eliminate outliers in cell behavior, only the tagged cells were then used to calculate areas at all remaining time points and used for comparison of means. We show significant difference between the 60 and 0 RPM chips at 6-8 hrs. * p<0.05. Matlab code in Appendix F.

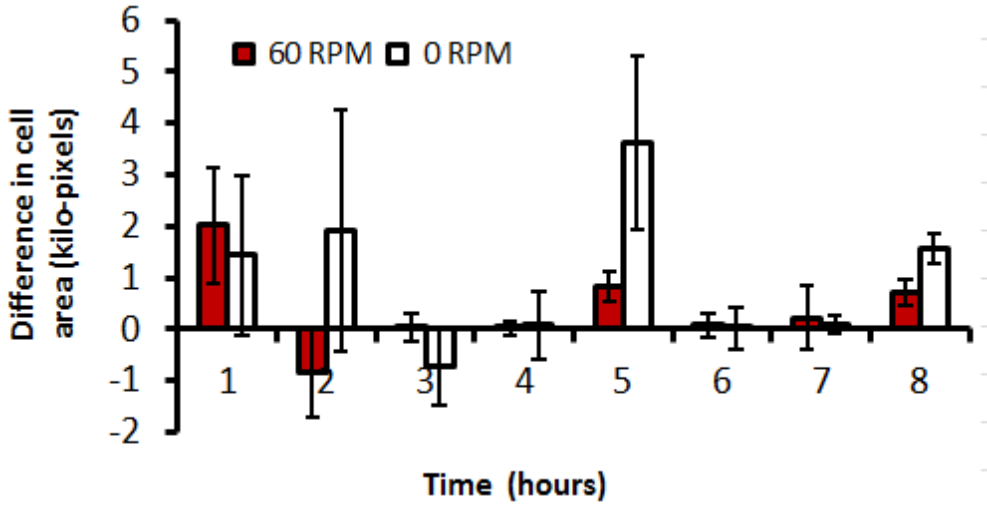

Figure 26. Difference in cell area between current time point and previous time point (n=3) and 1 S.D. error bars. To eliminate outliers in cell behavior, only the 3 median values of difference were used for analysis. Although much variability exists in the measurements, specimens at 0 RPM averaged 70% higher differences when compared with 60 RPM.

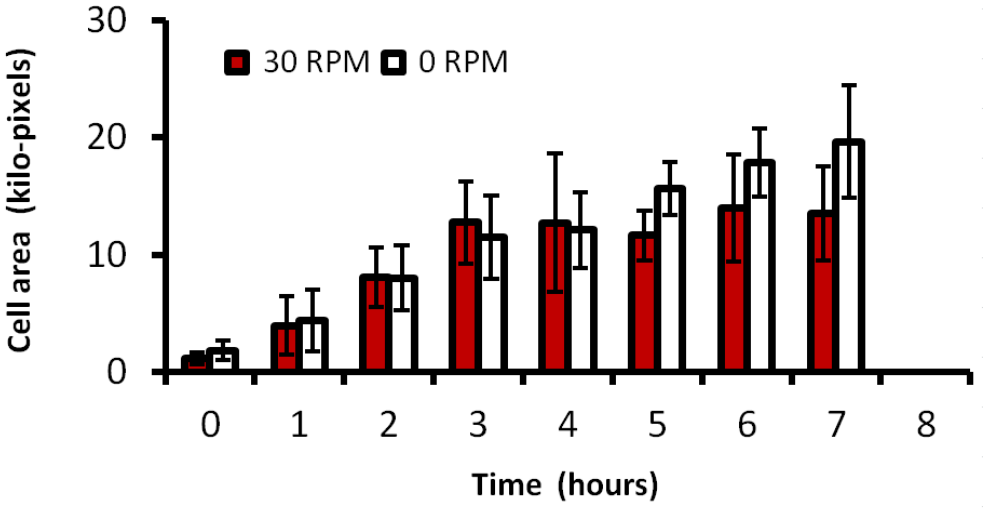

Figure 27. Mean values of same-cell areas (n=3) and 1 S.D. error bars. From calculated cell areas at 8 hrs, cells with the three median values were digitally-tagged. To eliminate outliers in cell behavior, only the tagged cells were then used to calculate areas at all remaining time points and used for comparison of means. We did not show any significant difference between the 30 and 0 RPM chips. Matlab code in Appendix F.

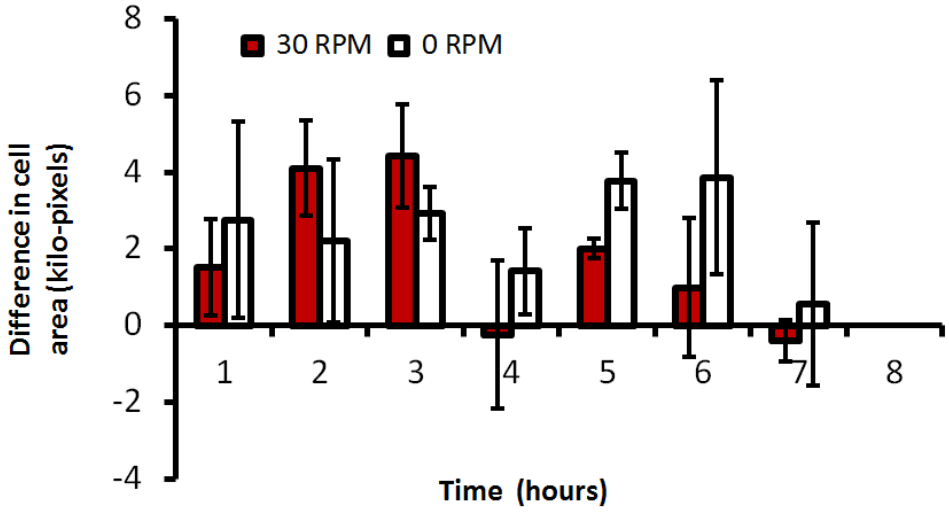

Figure 28. Difference in cell area between current time point and previous time point (n=3) and 1 S.D. error bars. To eliminate outliers in cell behavior, only the 3 median values of fold difference were used for analysis. Although much variability exists in the measurements, specimens at 0 RPM averaged 40% higher differences when compared with 30 RPM.

4.3. Results

4.3.1. hMSCs without perfusion

Figure 24 shows images at 0, 1, 4, and 8 hr time points. From these timelapse images, we measured time-evolving, same-cell areas using a custom Matlab algorithm (see Fig. 25). Matlab code in Appendix E. Average areas were not different in the first 3 hrs of clinorotation. After 5 hrs however, cell areas at 0 RPM increased dramatically while cells at 60 RPM showed little change. Significant differences were found at 6-8 hr time points. Cells under 30 RPM clinorotation did not exhibit significant differences in cell areas when compared with static controls even though cell areas at time points after 5 hrs, in the static chip exhibited mean values that were larger (see Fig. 27)

At each time point, we conducted a visual inspection of other cell groups and found that morphologies for the randomly selected cells were qualitatively representative of the entire population in the chip. Although our sample size was small, our preliminary results demonstrate substantial changes to hMSC morphology at 60 RPM that may affect functions important to bone health including differentiation and chemotactic homing.

We also took measurements for the absolute difference of same-cell areas between each time point and the previous point, as shown in Fig. 26 and 28. While much variability exists in the data, specimens at 0 RPM were measured at approximately 70% higher average difference when compared with 60 RPM and 40% larger when compared with 30 RPM.

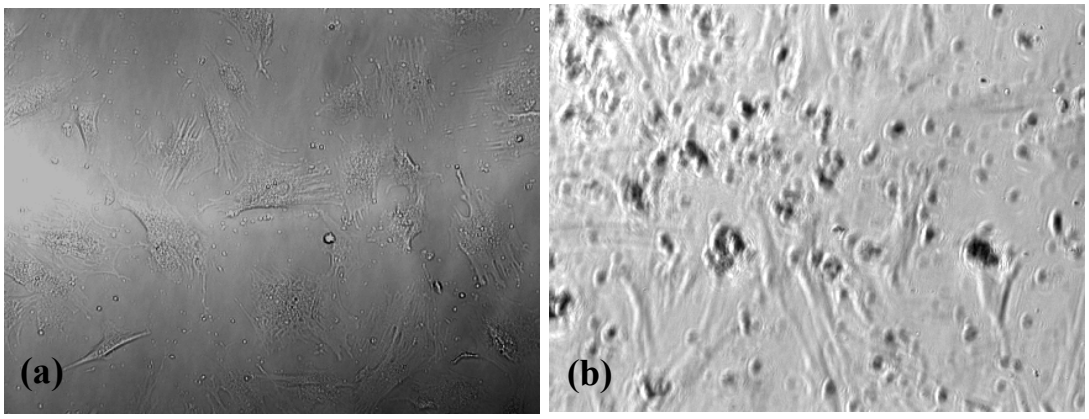

Figure 29. DIC images obtained after 12 hrs of continuous media circulation in microcavities. (a) static control at 0 RPM. (b) 60 RPM. Wear debris (darker particles in the image) has entered into the cavity and obstructs view of cells.

4.3.2. hMSCs with perfusion

Clinorotated cells were subjected to continuous perfusion of MSC media at 60 RPM for over 12 hrs. Cells remained viable and were motile. However, a comparison between 60 RPM and 0 RPM cells is not appropriate because seeding densities were different. Additionally, cells on the clinochip platform were subjected to another confounding factor: wear debris from the rotary joint, as shown in an extreme case in Fig. 29. A filter has been proposed for our clinochip system and discussed in more detail in the previous chapter.

4.3.3. HEK 293 with perfusion

At 0 hrs, cells were seeded and incubated for 2 hrs prior to recording observations (Fig. 30). Cells were mostly round and showed evidence of attachment

points at the edges. At 24 hrs, there was minimal difference between clinorotation and static control. Cell density in static control was higher than clinorotation, but could be from bubbles that induced shear on cells under clinorotation. At 48 hrs, there were very few cells remaining in clinorotation cultures, perhaps sheared off from bubbles.

Remaining cells were round and isolated or formed large 3D colonies. In contrast, cells in the static control were in large, monolayer colonies. At 72 hrs, many cells in the static control remained in large colonies, but individual units were difficult to distinguish. All cells in clinorotation were detached. Also at 72 hrs, cells in standard incubator (IB) formed large colonies and individual units were easily distinguished. Cells in the standard incubator with polystyrene (PS) flasks were more elongated than IB and static control.

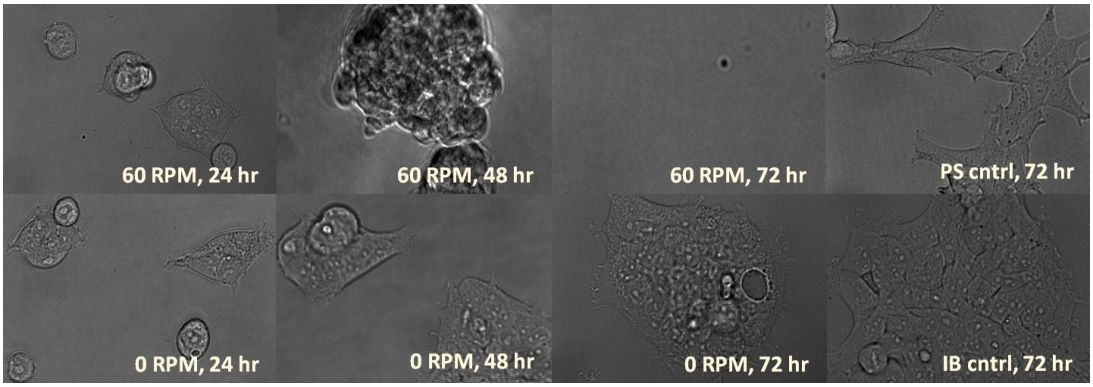

Figure 30. Phase contrast images (40X mag) of HEK 293 at 60 RPM clinorotation vs. the 0 RPM static control. 24hrs: little difference between 60 and 0 RPM. 48 hrs: only a few 3D aggregates remain in 60 RPM, compared to many monolayer colonies in 0 RPM. 72hrs: no cells remaining in 60 RPM, large colonies in 0 RPM. Cells in polystyrene (PS) were more spread than on glass (IB). Both PS and IB were cultured in a standard incubator vs. the environmental chamber for 60 and 0 RPM.

4.4. Discussion

We demonstrated CTM with HEK 293 cells and hMSCs, and obtained preliminary results that show how microgravity may affect cell behavior. HEK 293 cells at 60 RPM clinorotation formed 3D aggregates that were dramatically different from the monolayer colonies in the static control. While hMSCs under clinorotation were not as dramatically different from the static control, they did show significant changes in cell area. Both HEK 293 cells and hMSCs did not initially show these qualitative differences, but eventually showed differences at later time points.

We particularly found it interesting that the response in HEK 293 cells were so dramatically different from hMSCs. This behavior may partially be explained by the normal adhesion properties of these cells. In general, HEK 293 cells cultured in traditional plastic flasks tend to have more rounded morphologies and are more easily trypsinized than hMSCs. In fact, after trypsinization, HEK 293 cells tend to lift off of the substrate in colonies as opposed to lifting off as individual cells, as exhibited by hMCSs. We believe that this clumping behavior with HEK 293 cells allows them to bind more readily to each other than to substrates. As a result, under microgravity, this aggregation behavior appears to be dramatically enhanced, up to the point of forming 3D aggregates, as we observed.

Some investigators have reported cytoskeletal alterations in specimens subjected to less than 1 min of weightlessness on parabolic flights. While it is very possible that the cytoskeleton for the cells in our experiments also underwent similar alterations, we were not able to observe these effects without fluorescent tagging

cytoskeletal elements, such as actin filaments. Thus, we were only able to report observations on overall cell morphologies.

As a whole, CTM allowed us to identify the time-evolution of cell response in simulated microgravity without the limitation of only being able to obtain images at static time-points that are usually the extent of the capabilities afforded by conventional clinostat devices. Using static time points would limit the ability to understand how the time-dosage of microgravity affects cells, introduces more variability in experimental data, and may require more experimental controls to rule out confounding factors than our CTM system. For these reasons, and for its affordability and versatility, we believe that CTM represents a significant step forward in space biology research.

This observations of clinorotation speed dependence on cell response that we showed between 0, 30, and 60 RPM warrants further investigation. We think that lower rotation speeds may be too slow to simulate the microgravity condition. Thus, we believe that at some clinorotation speed between 30 and 60 RPM, there may be a critical speed that marks the transition to microgravity simulation. And if no distinct critical threshold exists, then we hypothesize that that the effect of clinorotation varies proportionally to speed up to the point where an increase in speed has diminishing effect on cell behavior.

The hypothesized dependence of clinorotation speed on cell behavior is a unique aspect that CTM can help to investigate; this is not possible through conventional clinostats that should be rotated at only one optimum speed at any given time. Therefore, CTM allows us to study possible “mechanoresponse” time constants

for cells. Previous investigations have reported, by probing integrin proteins, that cells are most sensitive to signals around 1 Hz, or 60 RPM. In future work, we would like to investigate these findings through CTM.

Gaining this type of understanding of cellular mechanoresponse is an application for this CTM technology that encompasses and transcends the field of space biology. In fact, we believe that using gravitational force to probe cells may be more accurate of an experimental tool when compared with mechanical probes. This is just one of many possible investigations through CTM. In the next chapter, we discuss another interesting application.

5. Conclusion

In the introduction to my dissertation, I discussed the future of manned space exploration in the context of the current sociopolitical climate. I want to reiterate that without adequate political support and financial backing, our efforts to explore space will not be possible. Like most of what we consider basic research, manned space exploration has no commercial market and therefore, its success is largely at the whim of our lawmakers.

But the focus of this dissertation was not to make an argument for funding space exploration. My goal was to present research tools that may allow investigators to develop enabling technologies. CTM is the type of tool that's been lacking in the space biology community. I think that large variations in experimental techniques with conventional clinostats make it difficult to reproduce results in space biology investigations. In addition, understanding cell response is sometimes incomplete without being able to characterize the time-evolution of these responses. Therefore, CTM is one step closer toward solving these issues.

5.1. Summary of work

A powerful aspect of CTM is that it can accommodate a wide range of research investigations and culture methods through the use of lab-on-chip devices. Microfluidic technologies have seen rapid development in the past decade and now, provide us with many different ways to investigate cell behavior. As described in my first Aim, my contribution to the field of microfluidics is providing approximations for the mass and momentum transport of fluid media into microcavities with

experimentally-validated models. Microcavities are simple to fabricate and can enable long-term cell culture and cell waste removal. The same analytical models may also facilitate the design of other device configurations to generate complex chemical microenvironments for "probing" cells in various ways. My hope is that other researchers, both within and outside of space biology, will find the approximations useful and time-saving.

After characterizing the mass and momentum transport in microcavities, my second Aim was to design and fabricate a clinorotation platform that was amenable to real-time microscopy and media exchange, a technique called Clinorotation Time-lapse Microscopy (CTM). My final design for the CTM system is in stark contrast to mega-scale clinostat microscopes that are prohibitively large, expensive to build, and may induce significant vibrations or impulse loads on cell cultures. Moreover, by using lab-on-chip devices, CTM provides the ability to precisely modulate microscale flow, a capability not easily accomplished with conventional clinostats.

For CTM, I also designed a fully-automated control system that establishes communication with various instruments for time-lapse, multi-position microscopy with clinorotation of cell cultures. Another important aspect of CTM was the design and fabrication of a magnetically-clamped rotary joint for media exchange between a stationary external fluid reservoir and the rotating, "clinochip" platform on the CTM system. Like the entire CTM system itself, our microfluidic rotary joint is many times smaller than readily available commercial parts.

Finally, my third Aim demonstrated CTM with various cell experiments. With HEK 293 cells, I showed that microgravity causes these types of cells to clump

together in 3D aggregates rather than adhering to their substrates. These observations were different than what we saw with hMSCs, which maintained their adhesion to substrates. However, microgravity significantly inhibited hMSC spreading at 60 RPM when compared with static controls after 6 hrs. Cells cultured at 30 RPM did not show significant differences in cell area. Therefore, there appears to be a dependence on clinorotation speed for the mechanoresponse of cells.

5.2. Limitations

While CTM is a very exciting technology for space biology, there are limitations. The first is that CTM can only simulate microgravity in one-axis (i.e. 2D simulation). While 2D simulated microgravity is still a very acceptable model, a 3D system would certainly be an improvement. Moreover, the rotary joint is a 2-passage system, but future designs could accommodate additional fluid passages to enable more complex fluid flows. Additionally, we showed that this rotary joint may introduce debris into cell cultures; therefore, the rotary joint can really only be used in conjunction with a filter. Alternatively, we can also consider alternative designs, perhaps those inspired by electrical slip rings on helicopters, for example.

Our analytical models for momentum and mass transport in microcavities also have their limitations. Firstly, our model for momentum transport tends to breakdown for low thickness-width (<0.5) aspect ratios. Therefore, we show that the decay constant for the analytical solution, compared with an FEM simulation of our experimental geometries is within 20% error. We believe that the analytical solution is still useful for an approximation, but also want to emphasize that for cell culture

applications using a configuration similar to Fig. 8, thin cavities (such as the one used in validation experiments) would not be practical since most useful designs would tend toward thickness-width aspect ratios >1. Additionally, our model for mass transport does not take into account recirculation regions that may influence how molecules from the top of the cavity reach cell cultures at the bottom. This model could therefore, be improved in future work.

5.3. Future work

An exciting proposal that extends the work in this dissertation is to investigate the time-dependent effects of microgravity on MSC behavior using CTM for microgravity simulation and lab-on-chip devices to generate chemical gradients in cellular microenvironments. Specifically, CTM is needed for visualizing the motile behavior of cells, and can also be used in conjunction with immunostains to quantify final focal contact densities and phenotype markers. This study will provide new insight into dynamic cellular events in weightlessness that may adversely affect bone formation, targeting future efforts toward *in vitro* experiments in spaceflight to develop effective treatments.

5.3.1. Background

Our goal in this future work is to form a more complete understanding of MSC response since we believe that a thorough investigation of complex cellular events cannot rely solely on end-point evaluations in experiments. This is especially true, for example, when observing single-cell behaviors at various stages in the cell cycle, identifying epigenetic changes, or studying motility-dependent processes. Our

overall hypothesis is that mechanical unloading alters the morphology and cytoarchitecture enough to disrupt MSC motility, chemotactic homing, and ultimately affect osteogenic differentiation and ECM deposition.

5.3.2. Research plan

This future work summarizes a new proposal to investigate the role of gravity-unloaded MSC morphology and motility in cellular differentiation. Our proposed specific aims directly address the Cell, Microbial and Molecular Biology (CMM) element, guiding questions CMM-1b, CMM-2, and CMM-3 in NASA's Space Biology (SB) Science Plan. We also address identifier AH2 in the NRC's 2011 Decadal Survey Report to investigate how extracellular cues and weightlessness could impact osteogenesis.

Specifically, we aim to: (1) investigate the long-term, dynamic behavior of MSCs under chemokine gradients in simulated microgravity and (2) quantify changes in distributions of focal adhesions and phenotype indicators. We have developed methods to address these aims, as elaborated in the following subsections.

5.3.3. Aim 1: Live cell MSC motility

MSCs exhibit chemotactic homing, i.e. chemically-induced migration toward a chemical source, during normal maintenance and injury repair. The cellular morphology and supporting cytoarchitecture is integral to this process, but may be adversely affected under microgravity. To investigate these effects, we developed

CTM to characterize time-dependent MSC behavior when subjected to spatiotemporally stable gradients of osteogenic growth factors.

This targets guiding question CMM-1b in the SB Plan to elucidate the effect of microgravity on cellular cytoarchitecture and CMM-3 for understanding cell-cell interactions. We are further interested in linking these effects to motility and overall MSC function.

Methods: Lab-on-chip devices mount easily to the CTM platform and can generate stable, linear chemical gradients with virtually no shear and high diffusion constants to allow sustained, *in vivo* like conditions and to optimize mass transport. The gradient device was demonstrated with chemotactic Vero cells in controlled, time-varying chemical gradients [72].

Protocols: In brief, early-passage, GFP-actin MSCs are plated onto fibronectin-treated lab-on-chip cavities at 3000 cells/cm^2 and incubated at 37 ºC, 50% humidity, and 5% CO_2 with MSC media (DMEM, 10% FBS, 0.3 mg/mL L-glutamine, 100 U/mL penicillin, 100 ug/mL streptomyicin) for 30 m, or up to 2 days, before interfacing with the environmentally-controlled CTM. Experimental groups are: (1) chemical gradient at 60 and 0 RPM, (2) chem grad at 6, 0 RPM, (3) no grad at 60, 0 RPM, (4) no grad at 6, 0 RPM. The chemical gradient is established by dual-syringe pump infusion of [MSC media without growth factors] and [MSC media + osteogenic growth factors]. Osteogenic growth factors comprise of 50 uM ascorbic acid-2-phosphate, 10 mM B-glycerophosphate, 100 nM dexamethasone.

An inverted microscope is programmed for multi-position, time-lapse microscopy, using fluorescence for temporal changes to GFP-actin, and DIC or phase

contrast for morphology and motility studies. After clinorotation, cells are chemically-fixed for immunostaining.

Analysis: Images will be analyzed with custom algorithms in Matlab (Mathworks) to create time-varying cell density maps and to calculate motility parameters including persistence times, random motility coefficients, and migration speeds. We will also calculate cell areas and GFP-actin filament density, orientation, and polarization. Cell-cell interactions are investigated by correlating density maps with local morphology, actin characteristics, and motility data.

5.3.4. Aim 2: Immunostains

Cytoarchitectural changes in microgravity can affect osteogenesis, as demonstrated in the earlier studies where MSCs tended toward adipocyte phenotypes. We predict similar results with our investigations but will also use live-cell and end-point immunostains to draw further conclusions. The live stain will be introduced into CTM-circulated MSC cocktails to temporally tag AP levels as an approximation of osteogenesis. End-point stains will be used to correlate cell density maps obtained in Aim 1 with relevant phenotype indicators, i.e. lipids and AP, to further infer how differentiation relates to cell-cell interactions.

We will also stain for vinculin, a focal adhesion protein that clusters in response to mechanical tension, in order to correlate its organization with GFP-actin characteristics and motility parameters. We anticipate that these experiments will reveal an orchestrated process linking morphology to differentiation.

This targets guiding question CMM-1b in the SB Plan to elucidate the effect of microgravity on cellular cytoarchitecture and CMM-2 to study morphogenesis. We are further interested in how MSCs differentiate and maintain bone health in spaceflight.

Methods: Immunoassay protocols are well-established and routinely used. After staining cells and imaging, we will quantify the distribution of vinculin, lipids, and AP. These results will be correlated with spatially collocated and temporally concurrent data obtained in Aim 1 to map the time-history of MSC behavior.

Protocols: In brief, the protocols and experimental groups for using the live-cell AP stain are identical to procedures in Aim 1, but will also incorporate equal concentrations of the AP stain into both reservoirs of the MSC cocktails. Media circulation will facilitate the diffusion of the non-toxic stain to enable nearly real-time reporting of AP activity.

End-point immunoassays are for vinculin, lipids, and AP. For vinculin, cells will be fixed in 4% paraformaldehyde, rinsed with water, washed in buffer, permeabilized with Triton X-100, washed in buffer, incubated with anti-vinculin antibody, and followed by a FITC-conjugated secondary antibody. For lipids, cells will be fixed in 10% formalin, rinsed with water, washed in 60% isopropanol, and incubated with Oil Red O. For AP, cells will be fixed in acetone/citrate, rinsed with water, and incubated in a mixture of naphthol AS-MX phosphate alkaline solution with fast blue RR salt.

Analysis: Fluorescence micrographs of the vinculin stain will be used to compare morphology and motility data to the concentration of focal contacts. Images

of lipids and AP will be correlated with cell density maps to determine relationships that may help elucidate the mechanisms that regulate tissue maintenance in spaceflight.

5.3.5. Design of experiments and statistics

The buried channel, in which cells will be subjected to a chemical gradient, will be "binned" along the gradient into five regions of interest (ROI) as shown in Fig. 31. Each ROI will correspond to a specific combination of clinorotation speed (0, 6, 60 RPM) and average biochemical concentration within the ROI (i.e. 10%, 30%, 50%, 70%, 90% concentration of osteogenic growth factor). Within each ROI, [clinorotated + gradient] measures will be normalized with corresponding [clinorotated without gradient] measures, to eliminate any confounding effects not due to clinorotation and biochemical concentration.

Two analyses will be performed: (1) within each ROI (concentration) to compare effects of clinorotation speed and (2) within each clinorotation speed to identify concentration-dependence. For each of the continuous outcome measures, we will perform one-way analyses of variance (ANOVA). Because these experiments represent conditions that have not been investigated, to date, we can only estimate the variance and differences we expect to see. Moreover, we will be performing cell-by-cell analyses from micrographs. If we use a conservative estimate that our standard deviation for any particular measure is twice that of the differences we wish to detect, a power analysis calculation of sample size yields a sample size of 88 cells, based on a critical significance of $\alpha = 0.05$ and statistical power of $(1- \beta) = 0.9$ [110].

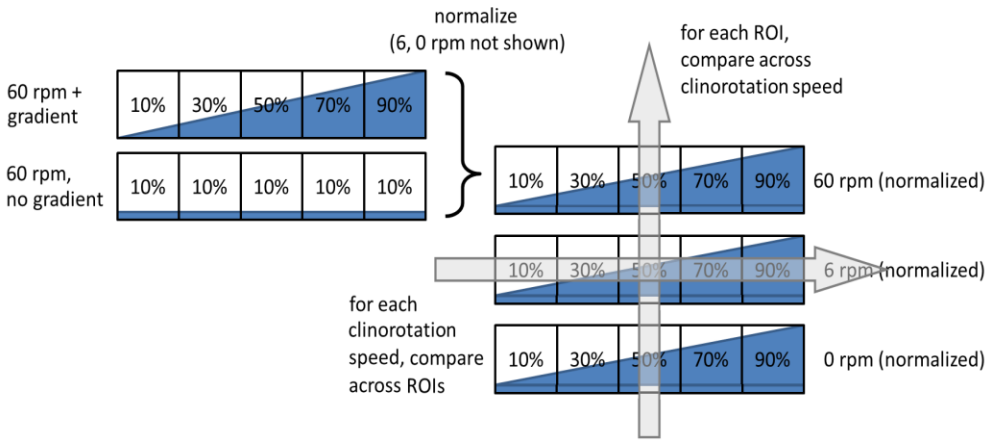

Figure 31. Experiment design compares cellular regions of interest (ROIs) in growth factor gradients v. no gradient. Also compare clinorotation speeds. Statistics w/ one-way ANOVA.

Since we expect at least 10 cells in any given ROI, it is estimated that 9 independent experiments will need to be conducted, assuming that each chip can accommodate one buried channel at a time. This is a conservative estimate because our chips can reasonably fit up to four microchannels. Thus, we conservatively need to complete up to 36 trials, and as few as twelve.

Schedule: A typical trial consists of thawing low-passage stem cells, expanding them in flasks, fabricating and sterilizing microfluidic devices, seeding cells in devices, subjecting cells to clinorotation for up to 72 hours, staining cells, and data processing. This entire process takes approximately one week. Some of these steps can be combined into batch operations or overlapped, but there are limitations based on the availability of shared equipment. The conservative total of 36 trials, which encompasses Aims 1 and 2, will conservatively take approximately ten months

to complete, which includes an extra month budgeted for schedule conflicts and experiment reruns. If we finish the experiments earlier than ten months, we will run additional trials or include other test conditions.

The specific device that we've proposed, originally published in [72] is based on a T-sensor configuration that maintains a distinct interface between two parallel streams of flowing media. Our device is slightly modified from published work but remains an inexpensive, multi-layer construction of glass, plastic, and biocompatible tape that is designed to generate stable, linear chemical gradients (see Fig. 32). We verified with fluorescent dye that with these modifications, we were still able to produce relatively linear gradients, as depicted in Fig. 33.

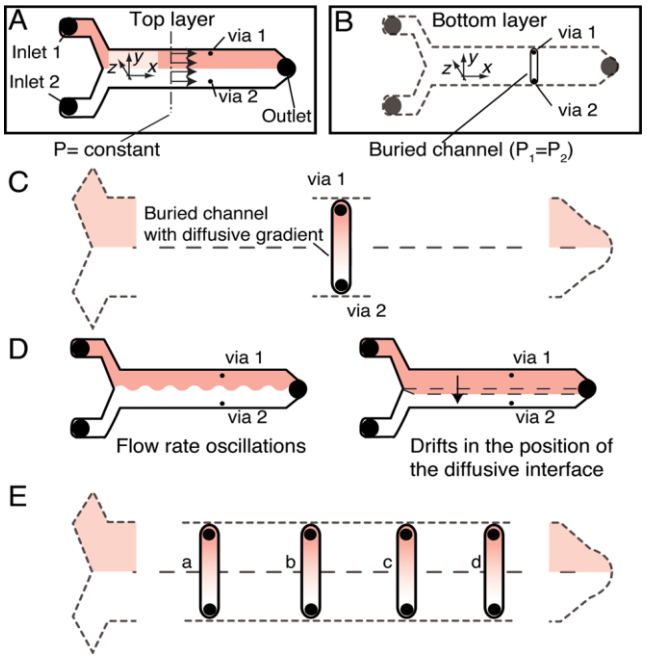

Figure 32. Chemical gradient generator. (a) vias connect T-sensor flow in top layer to the buried channel where cells are cultured in (b) the bottom layer. (c) a gradient is created within the buried channel. (d) flow oscillations and diffusive broadening do not disrupt the gradient. (e) multiple cavities can be designed onto a single chip to increase sample size. Reproduced from [72].

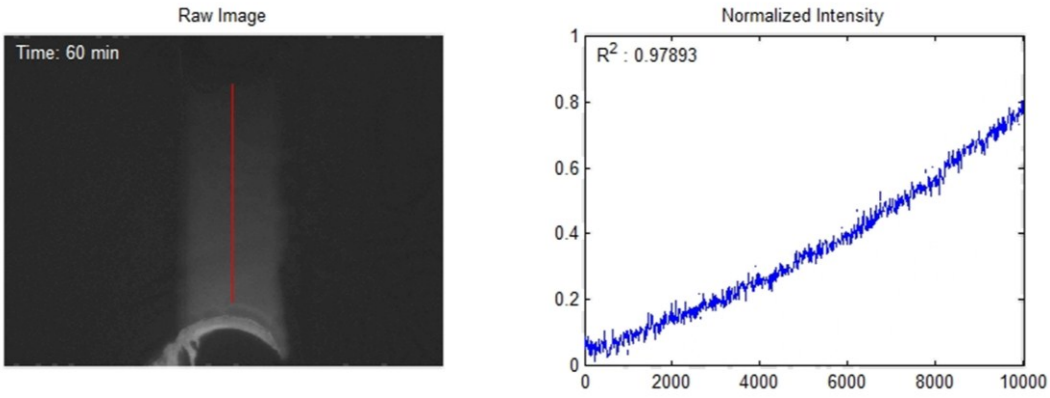

Figure 33. Validation of steady-state gradient in buried channel where cells would be cultured. A linescan (shown in red) and corresponding graph of fluorescence intensity, which reached R^2=0.98 in 20 min and remained steady after 1 hr of flow.

5.3.6. Expected outcomes

From our preliminary work (as presented in this dissertation), we believe that motility parameters with higher clinorotation speeds will be markedly different from static controls, showing that motility is reduced in microgravity. Temporal alterations to MSC morphology will reflect this by showing less spread cell shapes and a more randomized cytoskeletal orientation. These qualities should subsequently induce an adipogenic phenotype. Live-cell AP staining will give preliminary insight into the differentiation process and end-point stains show a complete lipid and AP assay. The vinculin stain is expected to show a proportional relationship between the concentration of focal contacts and MSC motility, and will also be proportional to the expression of an osteogenic phenotype.

5.3.7. Research roadmap

MSCs are important for maintaining bone health and play an integral role in bone fracture healing. Normal cell functions are hypothesized to be adversely affected in spaceflight and may partially explain the decreased bone health and generally poor quality of fracture healing in animal models flown in space. Our incomplete understanding of MSC behavior, as related to bone heath in space, may jeopardize the success of future, long-duration manned missions. Future results from this proposed work will contribute new knowledge that could eventually help to develop therapeutic countermeasures for astronauts.

This new space biology investigation is the preliminary groundwork to ultimately target spaceflight experiments that would confirm ground simulations and utilize the readily-available, commercial grade Culture Habitat (CHAB) or similarly designed system with integrated dual-tube pumps and microscopy-amenable configuration. Ultimately, we envision that these experiments may provide new knowledge of stem cell behavior in space, but that they also translate to clinical applications on Earth. Spinoff research includes: investigating genomic and proteomic profiles associated with MSC cytoarchitecture and differentiation; assessing the potential of MSCs in treating musculoskeletal pathologies in spaceflight; using drugs to promote normal MSC-mediated morphogenesis.

Epilogue

Outer space, stars, galaxies, and planets. They have always been a fascination of mine for as long as I can remember. Some of the most breathtaking moments in my life have been out on top of a mountain, in the vast expanse of a dessert, or in the woods far from civilization where I stare mesmerized into the star-filled night sky.

One of my earliest childhood memories was when, at the age of seven in the second grade, I learned about different kinds of clouds. And when I discovered that clouds were nothing more than water vapor, and that beyond Earth's atmosphere there was nothing more than outer space, I lost my sense of where God lived. I concluded then, that God did not sit on a golden throne on top of clouds. That's when I became addicted to outer space.

My idol in third grade was Galileo Galilee, and I made a plastic bottle figurine of him to present to my class. Later on, when I was 8 or 9, somehow I got my hands on some NASA posters of galaxies, planets, and astronauts that I plastered all over the walls of my room.

At age 10, my neighbor found out about my love for space and shared that same passion. When I had first met him, Joel was in the process of building a patio in his backyard; but within a couple months, had an amateur telescope pad set up. He showed me Mars, Saturn, Jupiter, the moon, pulsars, and many other stars I knew very little about. Joel talked all about space with me and while I grasped very little of it, he fueled my passion further.

When I started middle school, I remember grabbing my mom's old astronomy textbook, and spending weeks reading through the first few chapters, amazed by how much mankind knew about something we'll never completely understand. This was the first textbook that I read out of my own initiative.

In high school, at age 17, I secured an internship at NASA Goddard with Chuck Clagett's group. He later hired me as a Co-op when I was 19, and then converted me to a full-time civil servant when I was 23 after my obtaining my BS/MS degrees. I am still under his supervision to this day. Sometimes I have to remind myself that my job is the epitome of my childhood ambitions. For that, I am fortunate, beyond measure.

In the midst of all this, I also became interested in biology. You see, learning about outer space satisfied my curiosity, but it didn't fully satisfy my desire to do something purposeful with my life. During my undergraduate years, this became very important to me, so much in fact, that I started taking basic pre-med coursework in my senior year. Not only did I think that becoming a medical doctor would've given me a more fulfilling life, but I came to the conclusion that the human body was one of the most complex engineering systems we could study. Space biology is the perfect melding of my interests, providing me the opportunity to explore my scientific curiosity and allowing me the satisfaction of helping to preserve the health of astronauts, with potential spinoffs for clinical applications on Earth.

Appendix A: Matlab simulation of conventional clinostat

```
% Simulation of particle in clinostat
clear all; close all; clc

% Parameters
d=0.15; % diameter of clinostat [m]
rho1=1040; % density of a bead [kg/m^3]
rho2=1000; % density of fluid media [kg/m^3]
rho=rho1-rho2; % mass differential [kg]
w=200*(1/60*2*pi); % rotation speed [rad/sec]
g=9.81; % grav acceleration [m/sec^2]
mu=1e-3; % dynamic viscosity of water [N/s/m^2]
b=200e-6; % particle size [m]

% Initial values
r=d/4; % particle distance from center [m]
a1=0; % particle angle from horizontal in inertial frame [rad]
a2=0; % particle angle from horizontal in rotational frame [rad]
x=r*cos(a2); % x-position
y=r*sin(a2); % y-position

t=0:0.01:5;
xs=[]; ys=[]; vs=[]; a1s=[]; a3s=[]; % storage matrices
for lp=2:length(t)
    dt=t(lp)-t(lp-1);
    rev=w*dt;
    [a3,v]=solve(subs( ...
        'b^2*rho*(g*cos(a1)+w^2*r*cos(a2)+2*w*vv*cos(aa3-
a2)*sin(a2))=8*mu*vv*cos(aa3)'), ...
        subs( ...
        'b^2*rho*(g*sin(a1)+w^2*r*sin(a2)-2*w*vv*cos(aa3-
a2)*cos(a2))=8*mu*vv*sin(aa3)'));
    a3=eval(a3(1)); v=eval(v(1));
    % recalculate positions
    vx=v*cos(a3); vy=v*sin(a3);
    x=x+vx*dt; y=y+vy*dt;
    r=sqrt((x^2+y^2));
    a2=atan2(y,x);
    a1=a1+rev;
    % plot figures: inertial frame
    subplot(1,2,1)
    plot(d/2*cos(0:0.01:2*pi),d/2*sin(0:0.01:2*pi), ...
        'linewidth',2); % clinostat boundary
    hold on; plot(0,0,'kx'); % plot center
    plot(d/2*cos(a1),d/2*sin(a1),'b^','linewidth',2) % plot marker
    plot(r*cos(a1),r*sin(a1),'ro','linewidth',2); % particle location
    plot(0,0,'k.','markersize',2); hold off;
    axis(1.2*[-d/2,d/2,-d/2,d/2]); axis('square')
    set(gca,'FontSize',12,'LineWidth',1.5,'xticklabel',' ','yticklabel',' ')
    title('Inertial Frame','fontsize',12)
    % plot figures: rotating frame
    subplot(1,2,2)
    plot(d/2*cos(0:0.01:2*pi),d/2*sin(0:0.01:2*pi), ...
        'linewidth',2); % clinostat boundary
    hold on; plot(0,0,'kx'); % plot center
    plot(d/2*cos(0),d/2*sin(0), ...
        'b^','linewidth',2) % plot marker
```

```
    plot(x,y,'ro','linewidth',2); % particle location
    plot(0,0,'k.','markersize',2); hold off;
    axis(1.2*[-d/2,d/2,-d/2,d/2]); axis('square');
    set(gca,'FontSize',12,'LineWidth',1.5,'xticklabel',' ','yticklabel',' ')
    title('Rotational Frame','fontsize',12)
    % store values
    xs=[xs,x]; ys=[ys,y]; vs=[vs,v]; a1s=[a1s a1]; a3s=[a3s a3];
    % record movie
    pause(0.01);
    mov(:,lp-1)=getframe(gcf);
end
movie2avi(mov,'clino.avi','fps',20,'compression','none')
% plot figures: shear stress
tau=mu*3/2*abs(vs)/b;
subplot(2,1,1)
plot(t(1:length(vs)),10*tau,'linewidth',1);
set(gca,'FontSize',12,'LineWidth',1.5,'xticklabel',' ')
title('Maximum Shear Stress (dyne/cm^2)','fontsize',12)
% plot figures: inertial frame
subplot(2,2,3)
plot(d/2*cos(0:0.01:2*pi),d/2*sin(0:0.01:2*pi), ...
    'linewidth',2); % clinostat boundary
hold on; plot(0,0,'kx'); % plot center
r=sqrt(xs.^2+ys.^2);
plot(r.*cos(a1s),r.*sin(a1s),'r','linewidth',1); % particle location
hold off; axis(1.2*[-d/2,d/2,-d/2,d/2]); axis('square')
set(gca,'FontSize',12,'LineWidth',1.5,'xticklabel',' ','yticklabel',' ')
title('Inertial Frame','fontsize',12)
% plot figures: rotating frame
subplot(2,2,4)
plot(d/2*cos(0:0.01:2*pi),d/2*sin(0:0.01:2*pi), ...
    'linewidth',2); % clinostat boundary
hold on; plot(0,0,'kx'); % plot center
plot(xs,ys,'r','linewidth',2); % particle location
hold off; axis(1.2*[-d/2,d/2,-d/2,d/2]); axis('square');
set(gca,'FontSize',12,'LineWidth',1.5,'xticklabel',' ','yticklabel',' ')
title('Rotational Frame','fontsize',12)
```

Appendix B: Matlab analytical solution for cavity flow

```
% Analytical Solution from Weiss and Florsheim 1965
% First order approximation for 2d lid driven flow
clear all; close all; clc

d=2e-3; w=0.94e-3;  % depth and width [m]
uinf=0.0015; % max velocity in freestream flow [m/s]
tb=w/40; % boundary layer thickness of incoming stream [m]

% x,y coord (origin at bottom left)
np=40; % mesh density
x=0:w/np/2:w; y=0:d/np/20:d;
[xx,yy]=meshgrid(x,y);

% some coefficients
ca=2*pi/3^(1/4)/w*sin(1/2*atan(sqrt(2)));
cb=2*pi/3^(1/4)/w*cos(1/2*atan(sqrt(2)));
cc=sin(1/2*atan(sqrt(2)))*cosh(cb*d)*cos(ca*d)+ ...
    cos(1/2*atan(sqrt(2)))*sinh(cb*d)*sin(ca*d)- ...
    tan(ca*d)/tanh(cb*d)*(cos(1/2*atan(sqrt(2)))*cosh(cb*d)*cos(ca*d)- ...
    sin(1/2*atan(sqrt(2)))*sinh(cb*d)*sin(ca*d));
cd=tan(ca*d)/tanh(cb*d);
ce=(1+cb^2/ca^2)*tan(ca*d)+(1-cb^2*cd^2/ca^2)*(1/tan(ca*d));
cf=3^(1/4)/pi*ca*cb*w^2/cc*(cos(ca*d)*sinh(cb*d)+cd*sin(ca*d)*cosh(cb*d));
ud=uinf/(1+cf*tb/w); ud=uinf; % boundary velocity

% get the x-direction velocities, ux
syms ysym; uxx=diff(ud*sin(pi*xx/w).^2/ca/ce/sinh(cb*d)/cos(ca*d)* ...
    (cb/ca*cosh(cb*ysym)*sin(ca*ysym)-sinh(cb*ysym)*cos(ca*ysym)+ ...
    (1-cb*cd/ca)/tan(ca*d)*sinh(cb*ysym)*sin(ca*ysym)),ysym);
for lp1=1:length(y)
    for lp2=1:length(x)
        ux(lp1,lp2)=subs(uxx(lp1,lp2),ysym,yy(lp1,lp2));
    end
end

% get the y-direction velocities, uy
syms xsym; uyy=-diff(ud*sin(pi*xsym/w)^2/ca/ce/sinh(cb*d)/cos(ca*d)* ...
    (cb/ca*cosh(cb*yy).*sin(ca*yy)-sinh(cb*yy).*cos(ca*yy)+ ...
    (1-cb*cd/ca)/tan(ca*d)*sinh(cb*yy).*sin(ca*yy)),xsym);
for lp3=1:length(y)
    for lp4=1:length(x)
        uy(lp3,lp4)=subs(uyy(lp3,lp4),xsym,xx(lp3,lp4));
    end
end

% truncate the data
y=y(2:end)-d/(np*d/w);
xx=xx(2:end,:); yy=yy(2:end,:)-d/(np*d/w);
ux=ux(2:end,:); uy=uy(2:end,:);

% plot the velocity magnitudes
um=sqrt(ux.^2+uy.^2); % velocity magnitudes
[xi,yi]=meshgrid(0:w/np/4:w,0:d/np/4:d);
mag=interp2(xx,yy,um,xi,yi,'spline');
figure; surf(xi,yi,mag); shading flat; axis equal; axis tight; view(0,90)
```

```
% plot centerline and max velocities vs. depth
umax=max(um,[],2); % max velocity along cavity depth
figure; plot(fliplr(y),abs(ux(:,round(end/2))))
hold on; plot(fliplr(y),umax,'r:'); set(gca,'YScale','log')

% plot streamlines
[stx,sty]=meshgrid(0:w/round(np/2):w,0:d/round((np/2*d/w)):d);
figure; streamline(xx,yy,ux,uy,stx,sty); axis equal; axis tight;

% ------------------------------------------------------------------------
% Compare analytical solution with critical Pe to find Lc

% critical Pe
diffcoeff=6.8e-10; % diffusion coefficient [m^2/s]
pelength=50e-6; % characteristic length [m]
vc=diffcoeff/pelength; % critical velocity for Pe=1 [m/s]
vcp=vc*ones(length(y),1);
scf=1; % conservative scaling factor

% find the critical length in cavity
fitcoeff=polyfit(fliplr(y),log(umax)',1);
fitumax=fitcoeff(1)*fliplr(y)+log(ud);
fitumax2=fitcoeff(1)*fliplr(y)+scf*log(ud); % from polyfit
fitumax3=ud*exp(-4.24/w*y); % from simplified derivation
fitumax4=ud*sinh(cb*[y(2:end),d])/sinh(cb*d); % from full derivation
figure; plot(fliplr(y),fitumax2,'b-',fliplr(y),log(umax),'k-', ...
    fliplr(y),log(abs(ux(:,round(end/2)))),'k:',fliplr(y),log(vcp), ...
    'r--',y,log(fitumax3),'g',fliplr(y),log(fitumax4),'r:')
iv=log(vc); iy=-w/4.24*(iv-scf*log(ud));
if iy<d
    hold on; plot(iy,iv,'ro')
    text(0.9*iy,0.9*iv,['Lc=',num2str(iy),'m'])
end
xlabel('Depth into Cavity [m]'); ylabel('ln(velocity) [m/s]')
title('Velocity Magnitudes vs. Depth into Cavity')
legend('polyfit','maximum','centerline','critical Pe','simple','complete')

% generate a threshold velocity plot
figure; hold on
for lp4=1:length(mag)
    for lp5=1:length(mag)
        if mag(lp4,lp5)<=vc
            plot(xi(lp4,lp5),yi(lp4,lp5),'k.');
        end
    end
end
shading flat; axis equal; axis tight; view(0,90)

% generate a threshold velocity plot
figure; hold on
for lp4=1:length(mag)
    for lp5=1:length(mag)
        if mag(lp4,lp5)<=vc
            plot((d-yi(lp4,lp5))*1000,xi(lp4,lp5)*1000,'k.');
        end
    end
end
shading flat; axis equal; axis tight; axis([0 4.9 0 1])
set(gca,'YAxisLocation','right','FontSize',12,'LineWidth',1.5)
set(gcf,'PaperUnits','centimeters'); xSize = 8; ySize = 12;
set(gcf,'PaperPosition',[0 0 xSize ySize])
set(gcf,'Position',[0 0 xSize*50 ySize*50])
```

```
% plot the velocity magnitudes
um=sqrt(ux.^2+uy.^2); % velocity magnitudes
[xi,yi]=meshgrid(0:w/np/4:w,0:d/np/4:d);
mag=interp2(xx,yy,um,xi,yi,'spline');
figure; surf(xi,yi,mag); shading flat; axis equal; axis tight; view(0,90)
set(gca,'YAxisLocation','right','FontSize',12,'LineWidth',1.5)
set(gcf,'PaperUnits','centimeters'); xSize = 8; ySize = 12;
set(gcf,'Position',[0 0 xSize*50 ySize*50])
set(gcf,'PaperPosition',[0 0 xSize ySize])
```

Appendix C: Solid Edge CAD drawings for CTM

The following drawings can be used as a reference to build the CTM system demonstrated in this dissertation. However, machining and material tolerances should be taken into account when attempting to reproduce the parts.

All dimensions are in inches (not mm) unless otherwise stated.

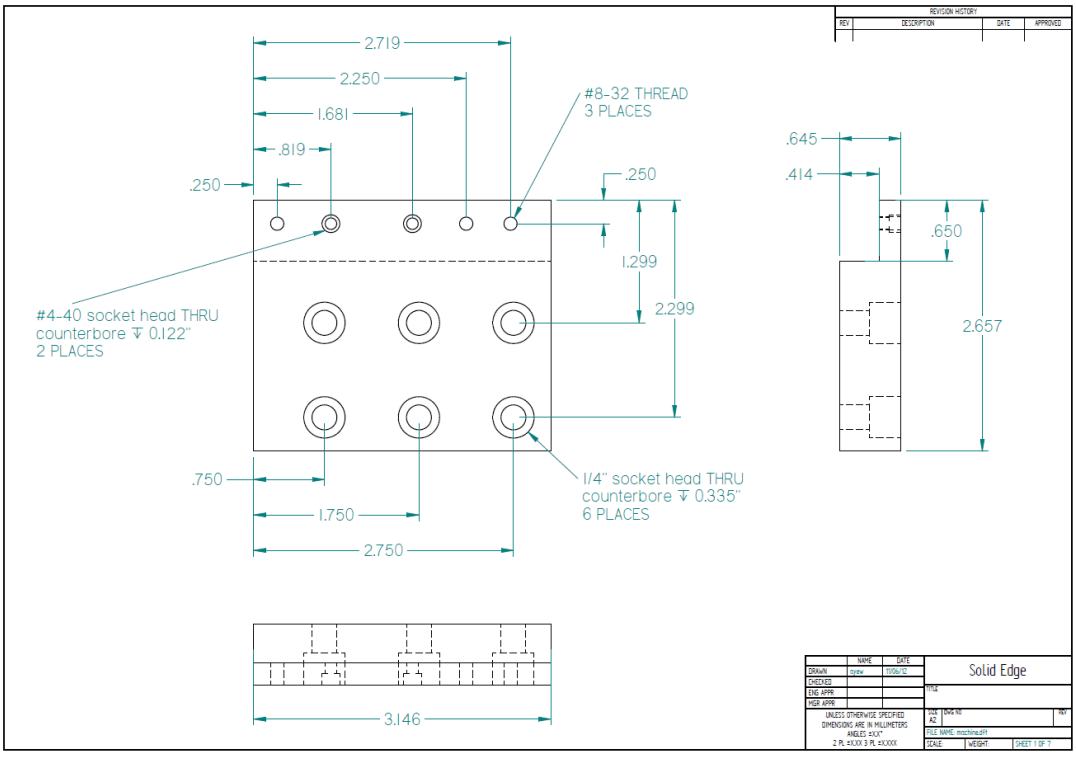

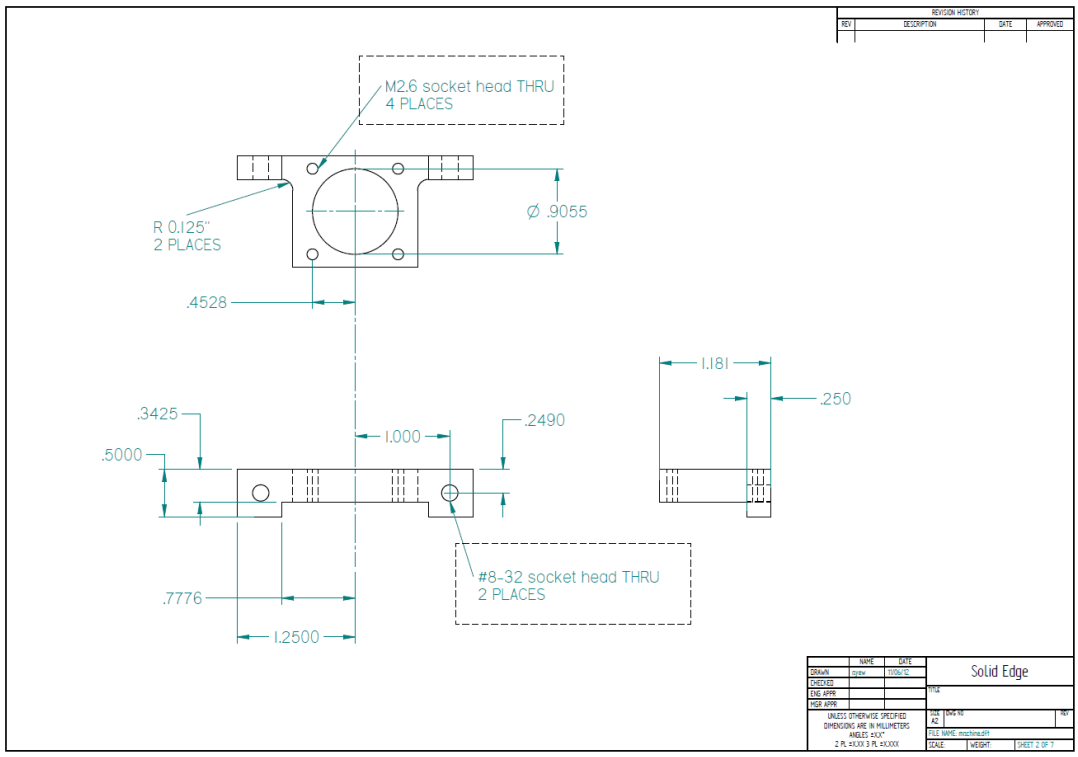
REVISION HISTORY
REV
DESCRIPTION
DATE
APPROVED
M2.6 socket head THRU
4 PLACES
R 0.125"
2 PLACES
Ø .9055
.4528
1.181
.250
.3425
.5000
1.000
.2490
#8-32 socket head THRU
2 PLACES
.7776
1.2500
NAME
DATE
DRAWN
CHECKED
ENG APPR.
MGR APPR.
Solid Edge
TITLE
SIZE
A2
DWG NO
REV
FILE NAME: machine.dft
SCALE:
WEIGHT:
SHEET 2 OF 7

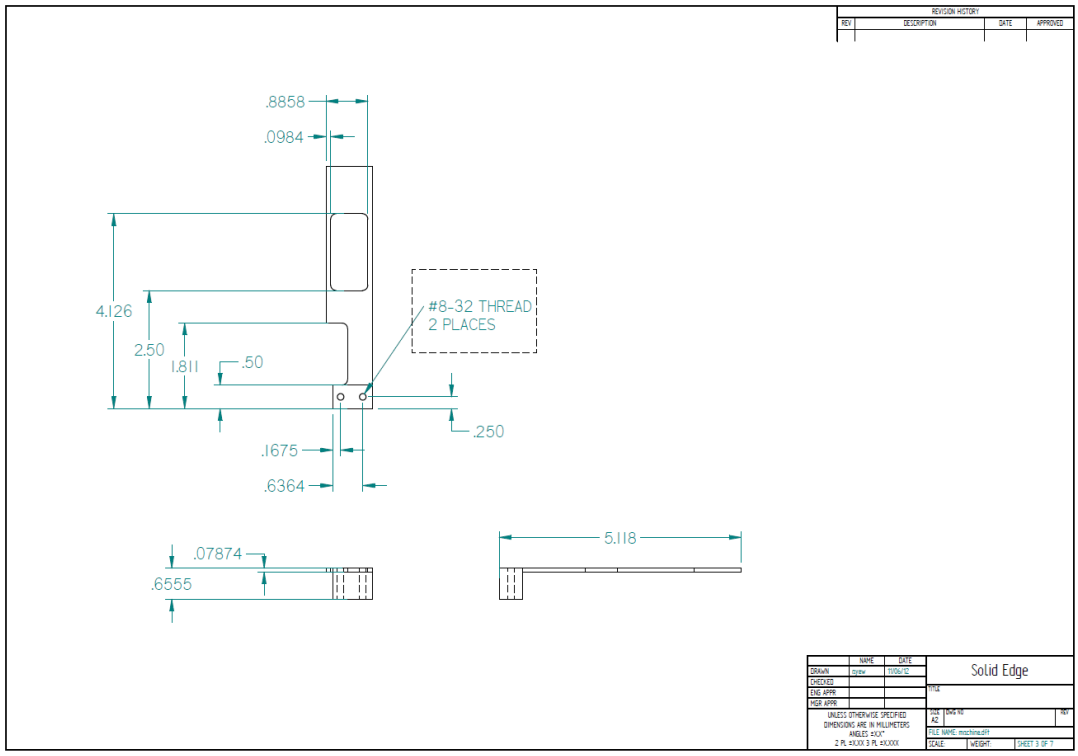
REVISION HISTORY
REV
DESCRIPTION
DATE
APPROVED
.8858
.0984
4.126
2.50
1.811
.50
#8-32 THREAD
2 PLACES
.250
.1675
.6364
5.118
.07874
.6555
NAME
DATE
DRAWN
CHECKED
ENG APPR.
MGR APPR.
Solid Edge
TITLE
SIZE
A2
DWG NO
REV
FILE NAME: machine.dft
SCALE:
WEIGHT:
SHEET 3 OF 7

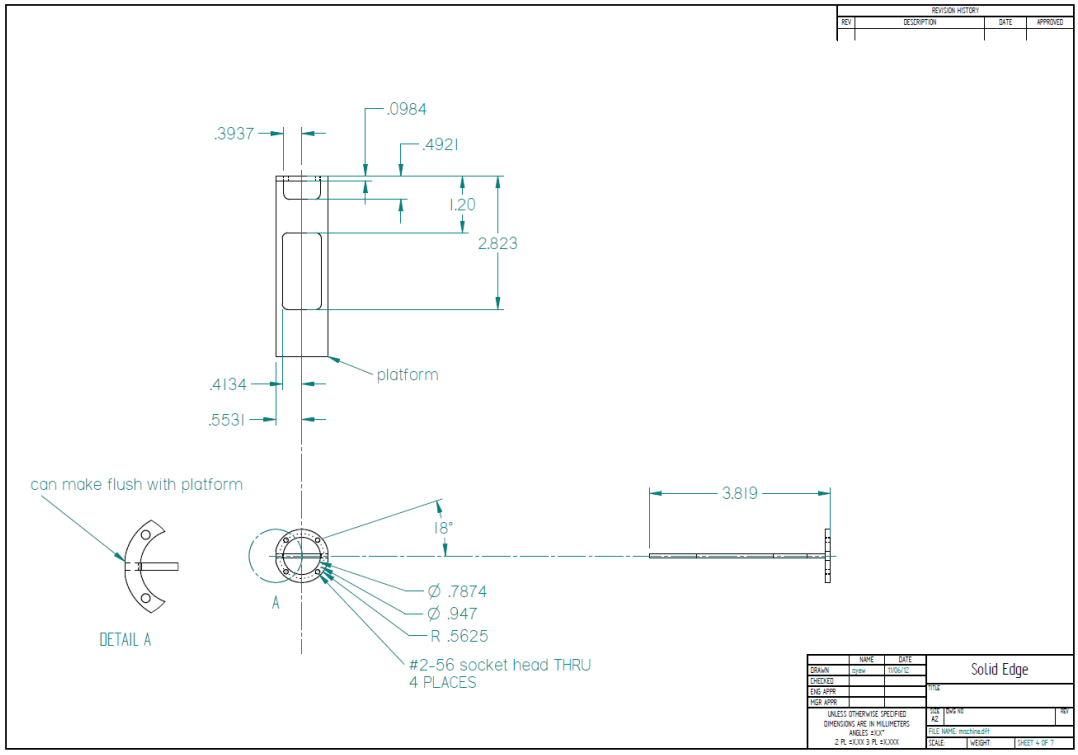
REVISION HISTORY
REV
DESCRIPTION
DATE
APPROVED
.0984
.3937
.4921
1.20
2.823
platform
.4134
.5531
can make flush with platform
18°
3.819
A
Ø .7874
Ø .947
R .5625
#2-56 socket head THRU
4 PLACES
DETAIL A
NAME
DATE
DRAWN
CHECKED
ENG APPR
MGR APPR
UNLESS OTHERWISE SPECIFIED
DIMENSIONS ARE IN MILLIMETERS
ANGLES ±1/2°
2 PL ±XX.X 3 PL ±X.XXX
Solid Edge
TITLE
SIZE
A2
DWG NO
REV
FILE NAME: machine.dft
SCALE:
WEIGHT:
SHEET 4 OF 7

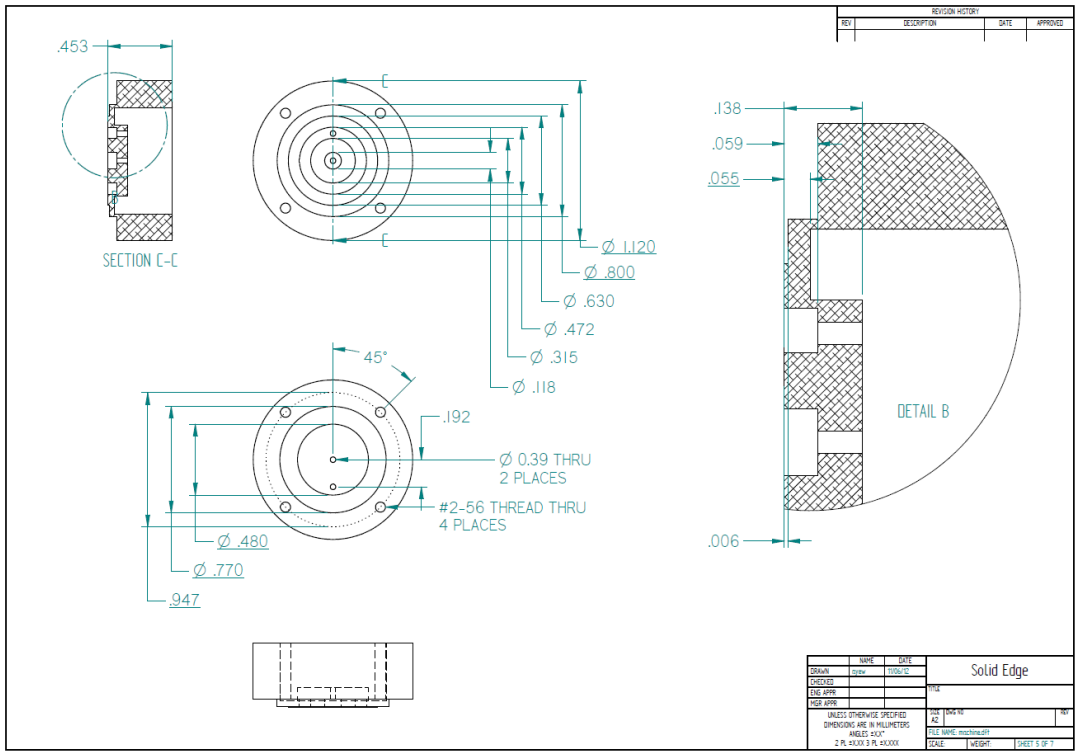
REVISION HISTORY
REV
DESCRIPTION
DATE
APPROVED
.453
SECTION C-C
Ø 1.120
Ø .800
Ø .630
Ø .472
Ø .315
Ø .118
45°
.192
Ø 0.39 THRU
2 PLACES
#2-56 THREAD THRU
4 PLACES
Ø .480
Ø .770
.947
.138
.059
.055
.006
DETAIL B
NAME
DATE
DRAWN
CHECKED
ENG APPR
MGR APPR
UNLESS OTHERWISE SPECIFIED
DIMENSIONS ARE IN MILLIMETERS
ANGLES ±1/2°
2 PL ±XX.X 3 PL ±X.XXX
Solid Edge
TITLE
SIZE
A2
DWG NO
REV
FILE NAME: machine.dft
SCALE:
WEIGHT:
SHEET 5 OF 7

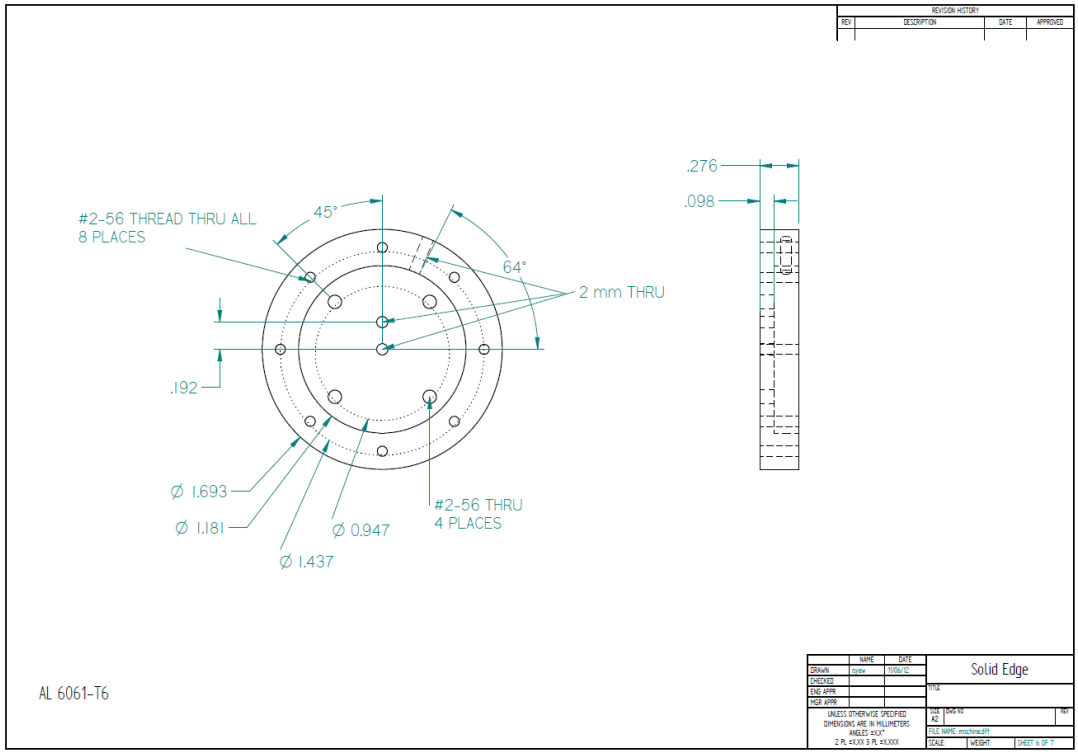
REVISION HISTORY
REV
DESCRIPTION
DATE
APPROVED
.276
.098
#2-56 THREAD THRU ALL
8 PLACES
45°
64°
2 mm THRU
.192
Ø 1.693
Ø 1.181
Ø 0.947
Ø 1.437
#2-56 THRU
4 PLACES
AL 6061-T6
NAME
DATE
DRAWN
CHECKED
ENG APPR.
MGR APPR.
Solid Edge
TITLE
SIZE
A2
DWG NO
REV
SCALE
WEIGHT
SHEET 6 OF 7

Appendix D: LabVIEW block diagram for control system

The controls algorithm we developed uses RS-232 communication protocols for the stepper motor, microscope, and XY motorized stage. The camera accepts commands via IEEE 1394 firewire. To ensure proper communications with instruments, we ask readers to refer to manufacturers' manuals.

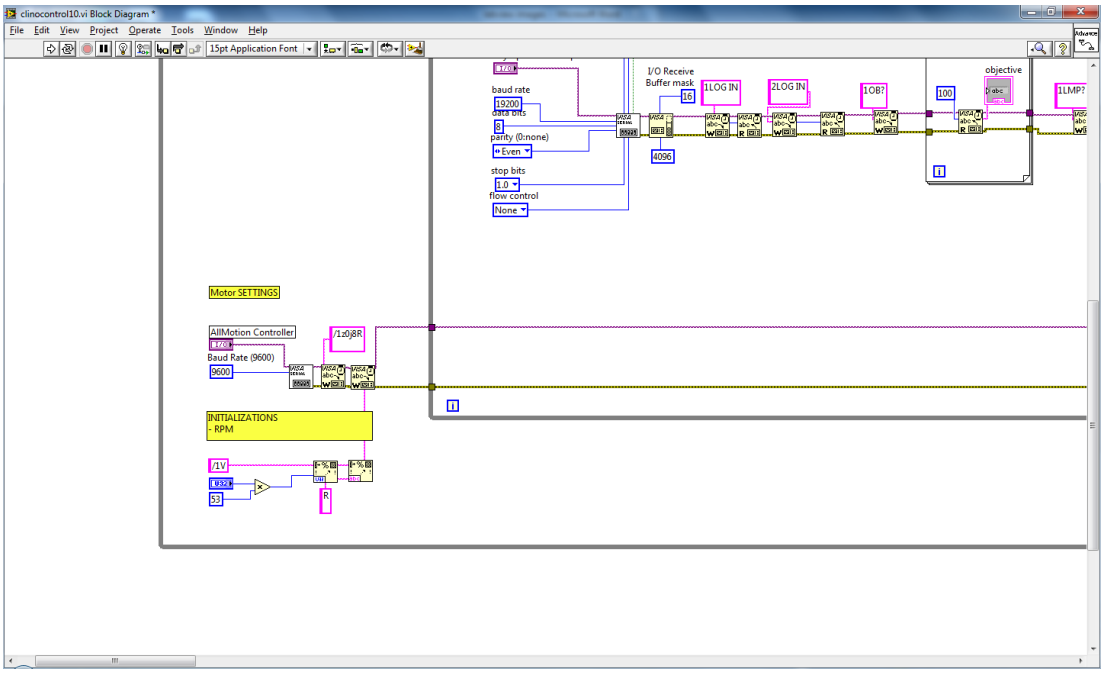

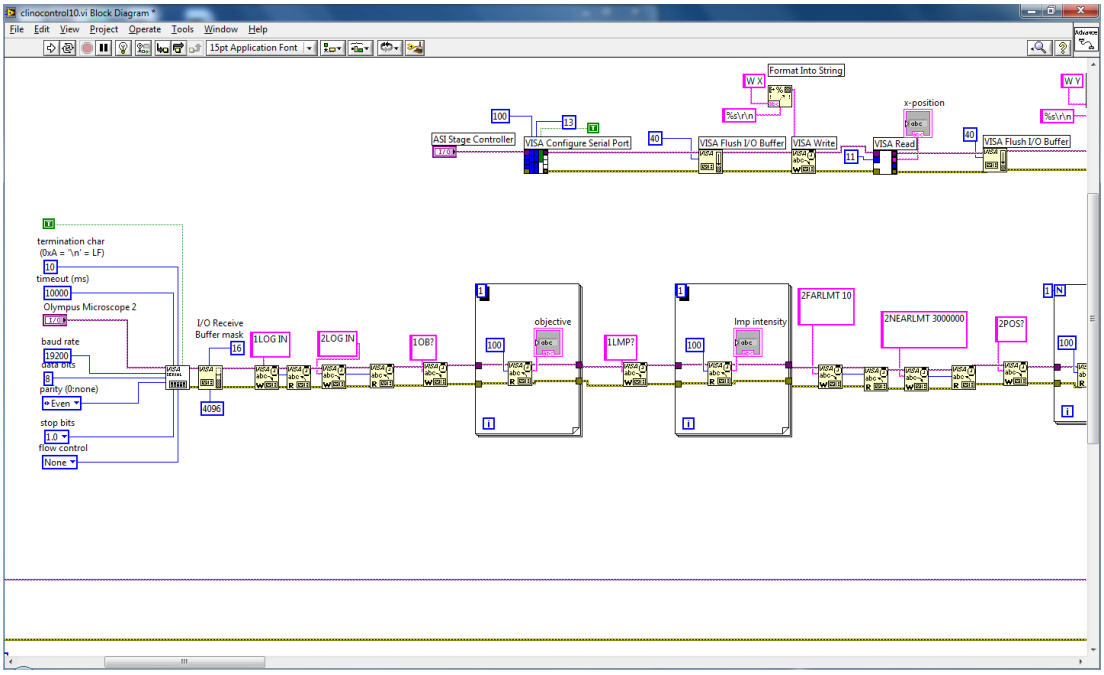
clinocontrol10.vi Block Diagram *
File Edit View Project Operate Tools Window Help
15pt Application Font
Format Into String
x-position
ASI Stage Controller
VISA Configure Serial Port
VISA Flush I/O Buffer
VISA Write
VISA Read
termination char
(0xA = '\n' = LF)
timeout (ms)
Olympus Microscope 2
baud rate
data bits
parity (0:none)
stop bits
flow control
I/O Receive
Buffer mask
1LOG IN
2LOG IN
1OB?
objective
1LMP?
Imp intensity
2FARLMT 10
2NEARLMT 3000000
2POS?

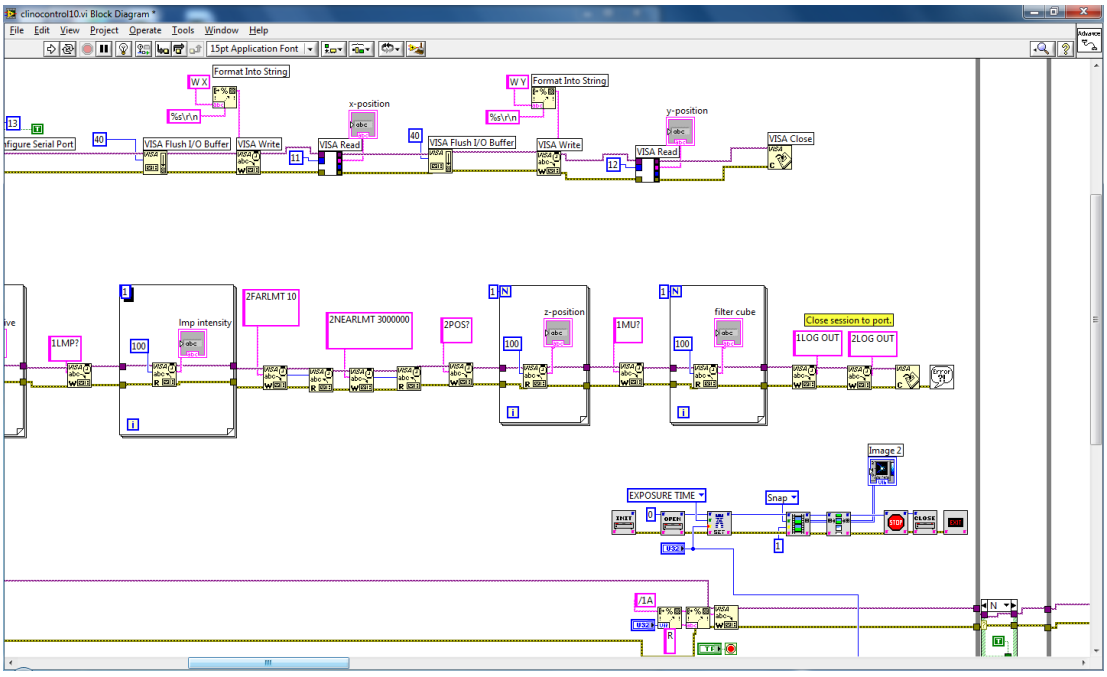
clinocontrol10.vi Block Diagram *
File Edit View Project Operate Tools Window Help
15pt Application Font
Format Into String
x-position
y-position
VISA Close
1LMP?
Imp intensity
2FARLMT 10
2NEARLMT 3000000
2POS?
z-position
1MU?
filter cube
Close session to port.
1LOG OUT
2LOG OUT
Image 2
EXPOSURE TIME
Snap

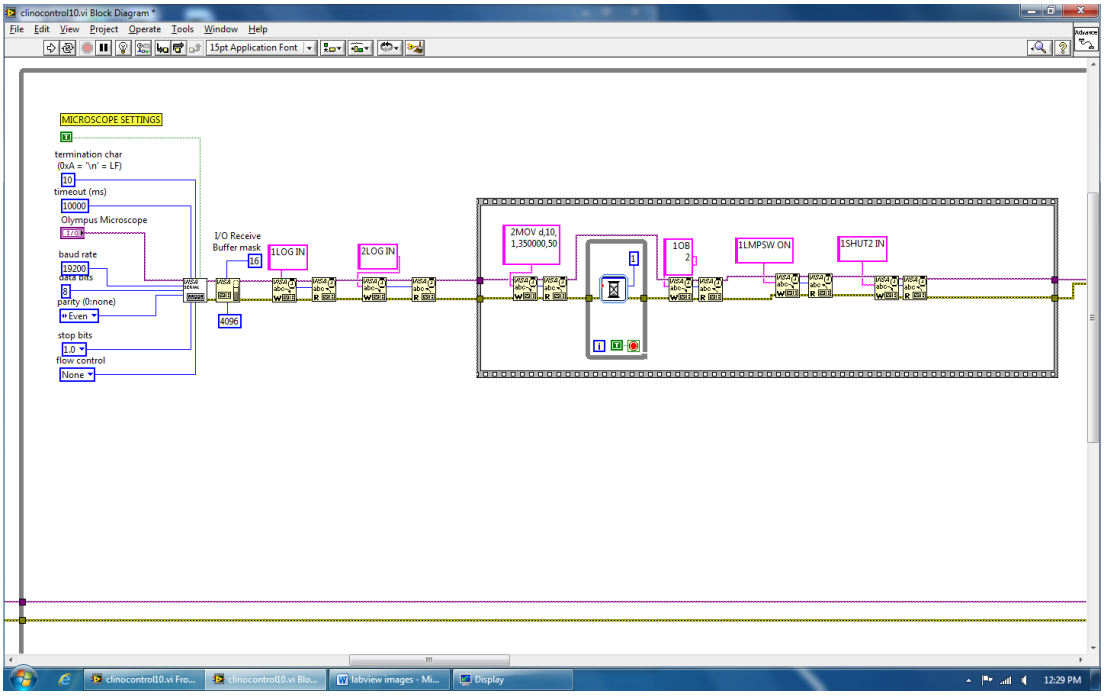
clinocontrol10.vi Block Diagram *
File Edit View Project Operate Tools Window Help
15pt Application Font
MICROSCOPE SETTINGS
termination char
(0xA = '\n' = LF)
10
timeout (ms)
10000
Olympus Microscope
baud rate
19200
data bits
8
parity (0:none)
Even
stop bits
1.0
flow control
None
I/O Receive
Buffer mask
16
4096
1LOG IN
2LOG IN
2MOV d,10
1,350000,50
1OB
2
1LMPSW ON
1SHUT2 IN
clinocontrol10.vi Fro...
clinocontrol10.vi Blo...
labview images - Mi...
Display
12:29 PM

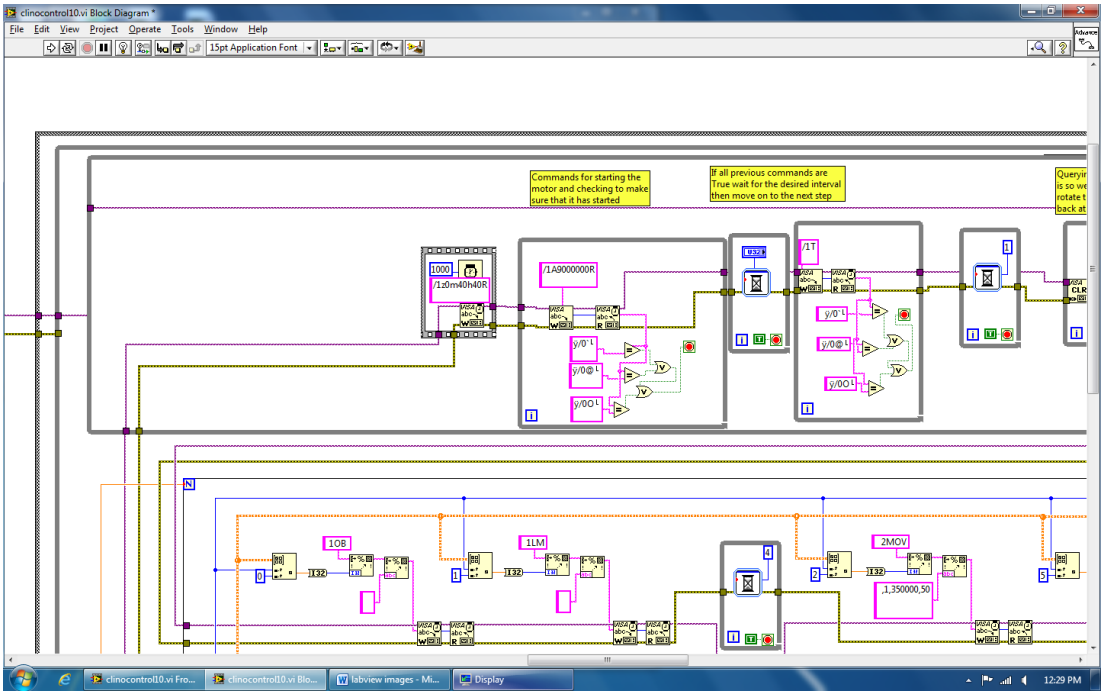
clinocontrol10.vi Block Diagram *
File Edit View Project Operate Tools Window Help
15pt Application Font
Commands for starting the
motor and checking to make
sure that it has started
If all previous commands are
True wait for the desired interval
then move on to the next step
1000
/1z0m40h40R
/1A9000000R
/1T
1OB
1LM
2MOV
,1,350000,50
clinocontrol10.vi Fro...
clinocontrol10.vi Blo...
labview images - Mi...
Display
12:29 PM

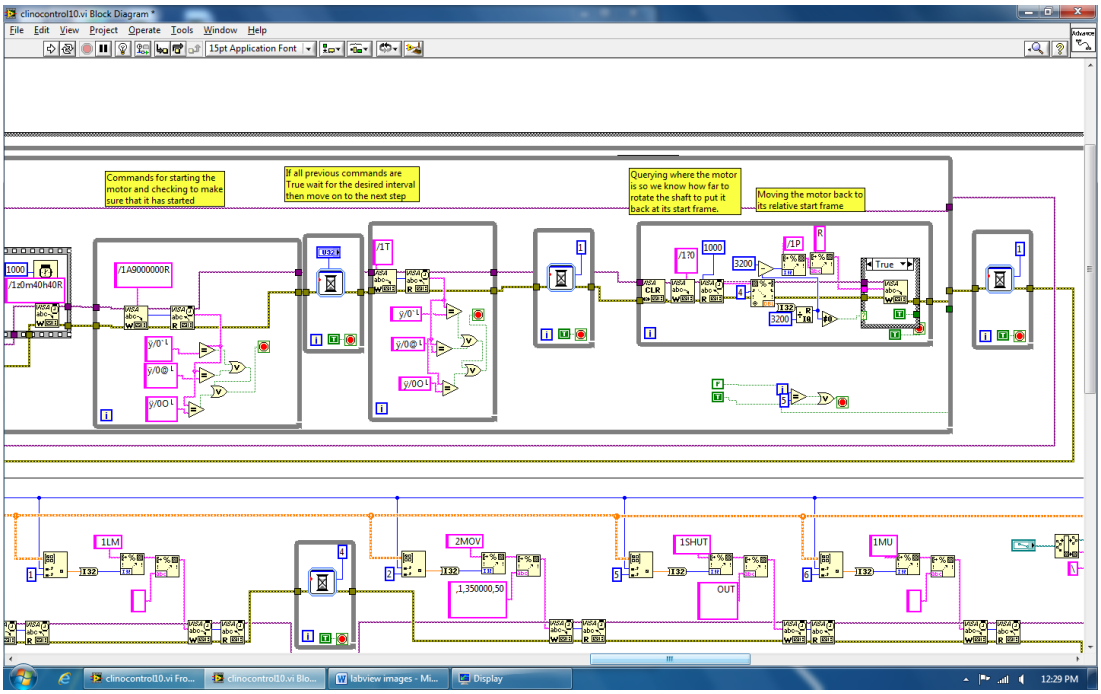
clinocontrol10.vi Block Diagram *
File Edit View Project Operate Tools Window Help
15pt Application Font
Commands for starting the motor and checking to make sure that it has started
If all previous commands are True wait for the desired interval then move on to the next step
Querying where the motor is so we know how far to rotate the shaft to put it back at its start frame.
Moving the motor back to its relative start frame
/1A9000000R
/1T
/1O
/1P
1LM
2MOV
1SHUT
1MU
OUT
clinocontrol10.vi Fro...
clinocontrol10.vi Blo...
labview images - Mi...
Display
12:29 PM

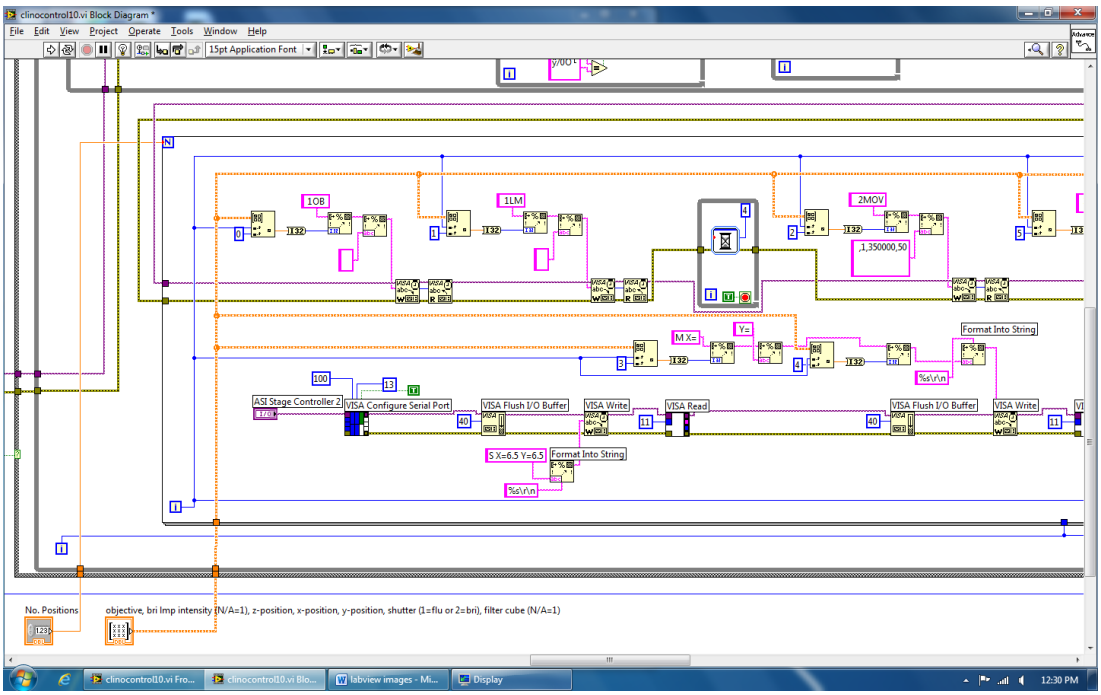
clinocontrol10.vi Block Diagram *
File Edit View Project Operate Tools Window Help
15pt Application Font
1OB
1LM
2MOV
M X=
Y=
Format Into String
ASI Stage Controller 2
VISA Configure Serial Port
VISA Flush I/O Buffer
VISA Write
VISA Read
S X=6.5 Y=6.5
No. Positions
objective, bri lmp intensity (N/A=1), z-position, x-position, y-position, shutter (1=flu or 2=bri), filter cube (N/A=1)
clinocontrol10.vi Fro...
clinocontrol10.vi Blo...
labview images - Mi...
Display
12:30 PM

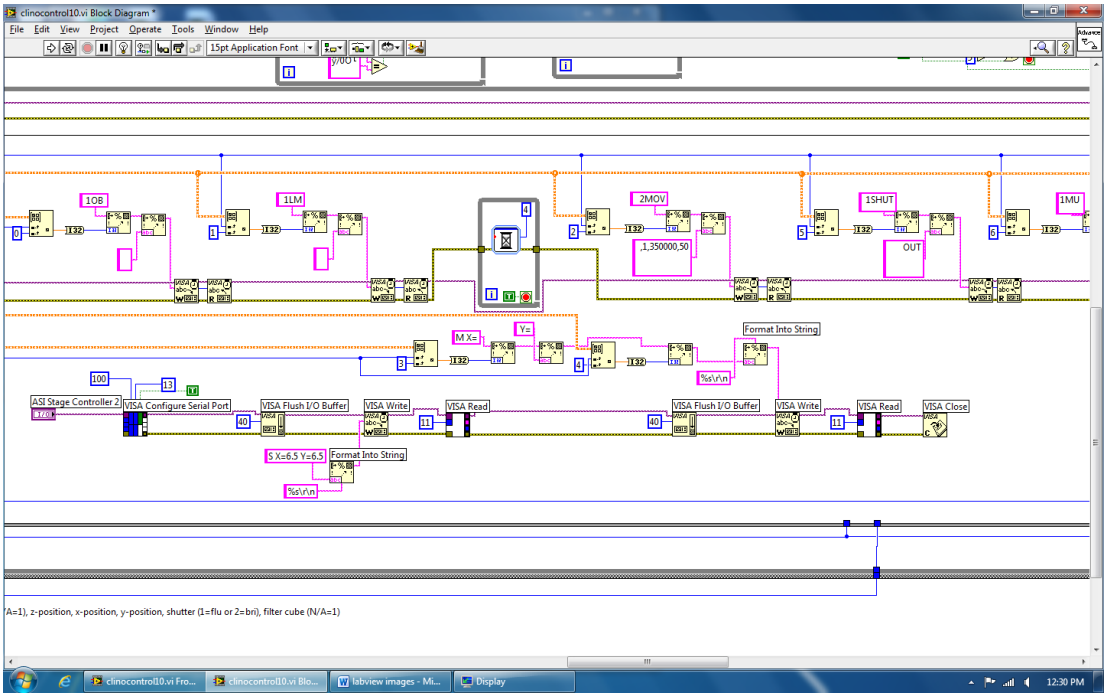
clinocontrol10.vi Block Diagram *
File Edit View Project Operate Tools Window Help
15pt Application Font
1OB
1LM
2MOV
,1,350000,50
1SHUT
OUT
1MU
M X=
Y=
Format Into String
%s\r\n
100
13
ASI Stage Controller 2
VISA Configure Serial Port
VISA Flush I/O Buffer
VISA Write
VISA Read
VISA Close
S X=6.5 Y=6.5
A=1), z-position, x-position, y-position, shutter (1=flu or 2=bri), filter cube (N/A=1)
clinocontrol10.vi Fro...
clinocontrol10.vi Blo...
labview images - Mi...
Display
12:30 PM

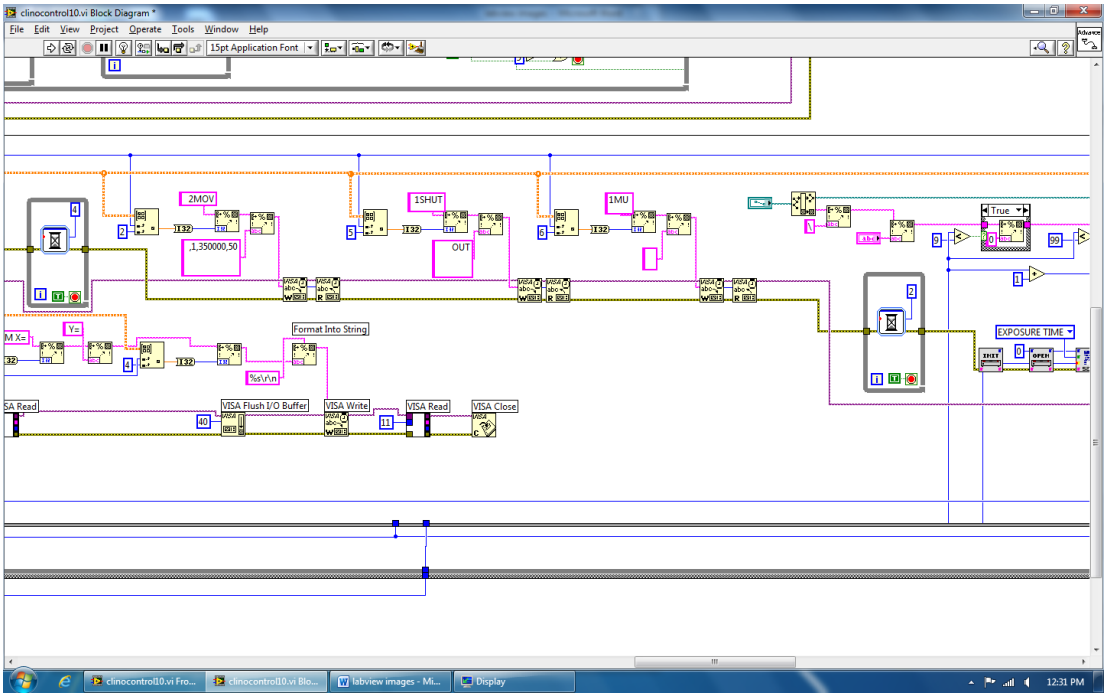
clinocontrol10.vi Block Diagram *
File Edit View Project Operate Tools Window Help
15pt Application Font
2MOV
,1,350000,50
1SHUT
OUT
1MU
True
EXPOSURE TIME
M X=
Y=
Format Into String
%s\r\n
VISA Flush I/O Buffer
VISA Write
VISA Read
VISA Close
clinocontrol10.vi Fro...
clinocontrol10.vi Blo...
labview images - Mi...
Display
12:31 PM

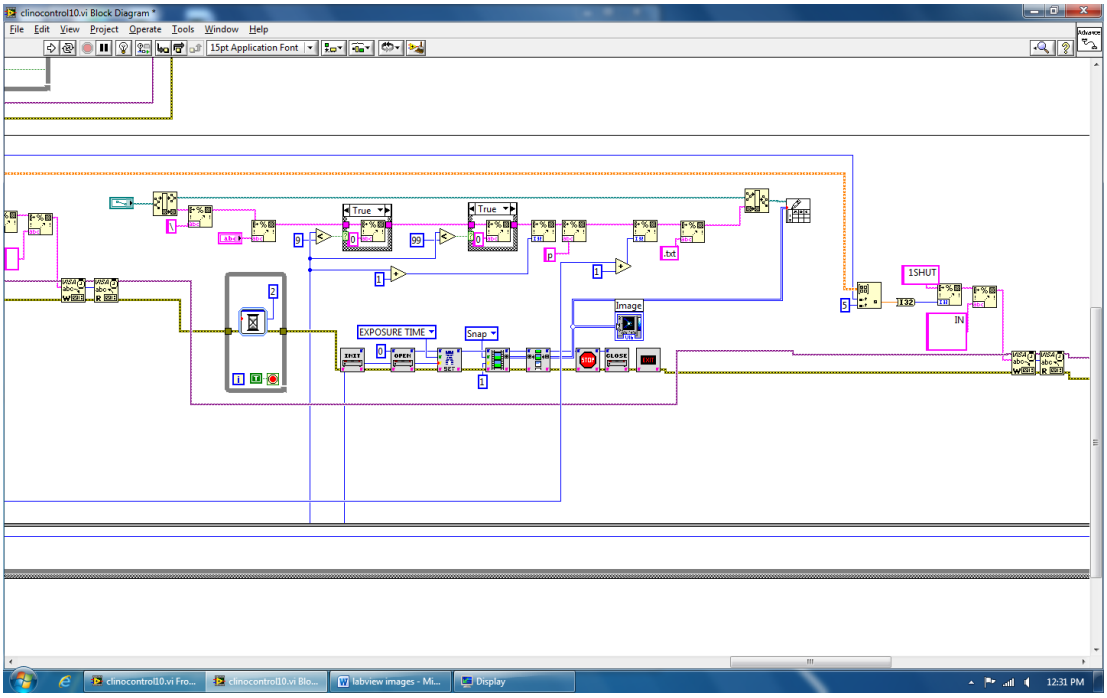
clinocontrol10.vi Block Diagram *
File Edit View Project Operate Tools Window Help
15pt Application Font
True
True
EXPOSURE TIME
Snap
Image
1SHUT
IN
clinocontrol10.vi Fro...
clinocontrol10.vi Blo...
labview images - Mi...
Display
12:31 PM

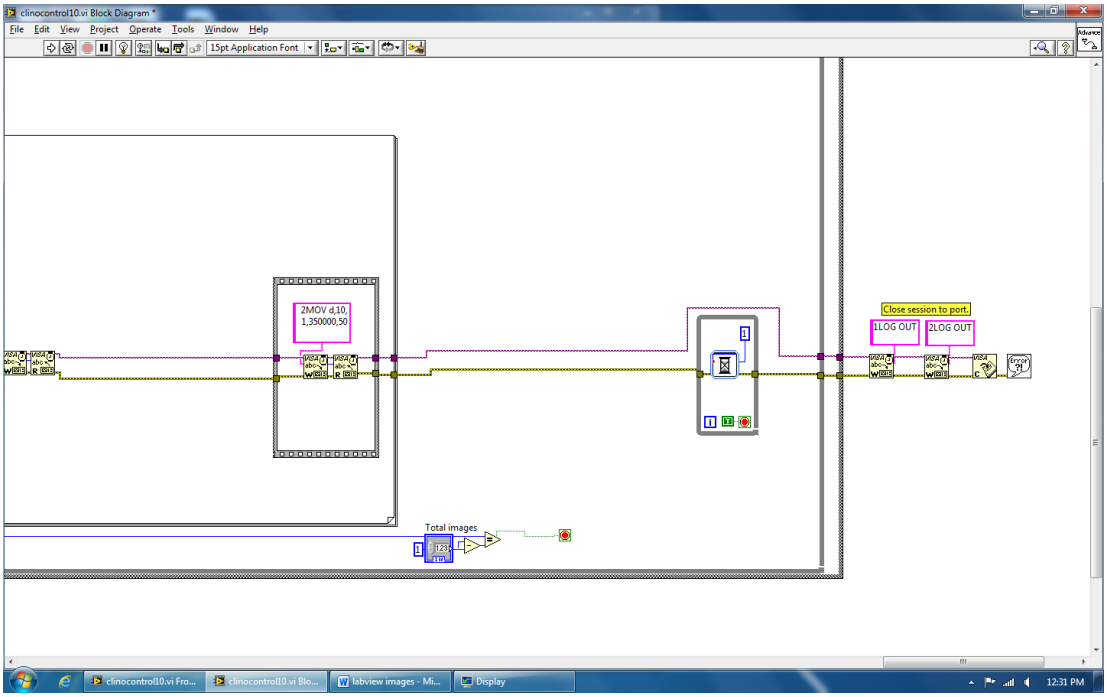
clinocontrol10.vi Block Diagram *
File Edit View Project Operate Tools Window Help
15pt Application Font
2MOV d,10,
1,350000,50
Close session to port
1LOG OUT
2LOG OUT
Total images
clinocontrol10.vi Fro...
clinocontrol10.vi Blo...
labview images - Mi...
Display
12:31 PM

Appendix E: Matlab image processing tool for cell morphology

```
% This program is an image processing tool that can be used to alter
% images, select regions of interest for calculating: (1) area, (2)
% major/minor axes dimensions, and (3) orientation
clear all; close all; clc

% load the data
im=imread('p3t005.bmp');
im=single(im);

% gray threshold
figure; histfit(im(:))
gt=input('Set threshold value (to use histogram mean, leave empty) and press
''Enter'': ');
if isempty(gt)==1
    gt=mean(im(:))
end
figure; subplot(1,2,1); imagesc(im); colormap(gray);
axis off; axis equal; axis tight; set(gca,'YDir','normal'); ax=pbaspect;
im(find(im<gt))=0;
im(find(im>=gt))=1;

% draw black lines
subplot(1,2,2); imagesc(im); colormap(gray); hold on;
axis off; axis equal; axis tight; set(gca,'YDir','normal'); ax=pbaspect;
title('Draw black lines')
fprintf('Click on two endpoints for all desired blackout lines and right-
click when done \n')
yblack=[]; xblack=[];
check1=1;
counter=1;
while check1==1
    [yblack(counter),xblack(counter),check1]=ginput(1);
    if mod(counter,2)==0
        blackline=line([yblack(counter-1),yblack(counter)], ...
            [xblack(counter-1),xblack(counter)]);
        set(blackline,'linewidth',1.5)
    end
    counter=counter+1;
end
yblack=yblack(1:end-1); xblack=xblack(1:end-1);
yblack(find(yblack<=0))=2;
xblack(find(xblack<=0))=2;
yblack(find(yblack>size(im,2)))=size(im,2)-1;
xblack(find(xblack>size(im,1)))=size(im,1)-1;
stepsize=100;
for loop2=1:length(yblack)/2
    xx=linspace(xblack(2*loop2-1),xblack(2*loop2),stepsize);
    yy=linspace(yblack(2*loop2-1),yblack(2*loop2),stepsize);
    for loop3=1:length(xx)
        im(round(xx(loop3)),round(yy(loop3)))=0;
        im(round(xx(loop3))+1,round(yy(loop3)))=0;
        im(round(xx(loop3)),round(yy(loop3))+1)=0;
        im(round(xx(loop3))-1,round(yy(loop3)))=0;
        im(round(xx(loop3)),round(yy(loop3))-1)=0;
    end
end
```

```
% select ROI
subplot(1,2,2); imagesc(im); colormap(gray); hold on;
axis off; axis equal; axis tight; set(gca,'YDir','normal'); ax=pbaspect;
title('Select ROIs')
fprintf('Click on one point in every ROI and right-click when done \n')
yuswer=[]; xuser=[];
check2=1;
counter=1;
while check2==1
    [yuser(counter),xuser(counter),check2]=ginput(1); % get points from the
picture
    if check2==1
        plot(yuser(counter),xuser(counter),'r+')
    end
    counter=counter+1;
end
yuser=yuser(1:end-1); xuser=xuser(1:end-1);

area=[]; major=[]; minor=[]; direction=[];
for loop=1:length(yuser)
    npix=0; % count pixels
    xpix=[]; ypix=[]; % store xy pixel locations for linescan
    xstore=[]; ystore=[]; % store xy pixel for fill
    xo=floor(xuser(loop)); yo=floor(yuser(loop));

    % start scanfill
    yc=yo; xxline=xo;
    while isempty(xxline)==0 % up direction

        xline=xxline; xxline=[];
        while isempty(xline)==0
            xc=min(xline); xs=xc;
            xline(find(xline==xc))=[];

            check3=1; % right direction
            while check3==1
                if im(xc,yc)==1 && xc<size(im,1) && yc<size(im,2) && ...
                          xc>1 && yc>1
                    if im(xc+1,yc)==1 || im(xc,yc+1)==1 || ...
                          im(xc-1,yc)==1 || im(xc,yc-1)==1 ||
                    im(xc+1,yc+1)==1 || im(xc-1,yc+1)==1 ...
                            || im(xc-1,yc-1)==1 || im(xc+1,yc-1)==1
                        npix=npix+1;
                        xpix=[xpix xc]; ypix=[ypix yc];
                        xxline=[xxline xc];
                        xstore=[xstore xc]; ystore=[ystore yc];
                        xc=xc+1;
                        xline(find(xline==xc))=[];
                    end
                else
                    check3=0;
                end
            end

            xc=xs-1;
            xline(find(xline==xc))=[];
            check4=1; % left direction
            while check4==1
                if im(xc,yc)==1 && xc<size(im,1) && yc<size(im,2) && ...
                          xc>1 && yc>1
                    if im(xc+1,yc)==1 || im(xc,yc+1)==1 || ...
```

```
                    im(xc-1,yc)==1 || im(xc,yc-1)==1 ||
                im(xc+1,yc+1)==1 || im(xc-1,yc+1)==1 ...
                        || im(xc-1,yc-1)==1 || im(xc+1,yc-1)==1
                    npix=npix+1;
                    xpix=[xpix xc]; ypix=[ypix yc];
                    xxline=[xxline xc];
                    xstore=[xstore xc]; ystore=[ystore yc];
                    xc=xc-1;
                    xline(find(xline==xc))=[];
                end
            else
                check4=0;
            end
        end
    end
    yc=yc+1;
end

yc=yo-1; xxline=xo;
while isempty(xxline)==0 % down direction

    xline=xxline; xxline=[];
    while isempty(xline)==0
        xc=min(xline); xs=xc;
        xline(find(xline==xc))=[];

        check3=1; % right direction
        while check3==1
            if im(xc,yc)==1 && xc<size(im,1) && yc<size(im,2) && ...
                    xc>1 && yc>1
                if im(xc+1,yc)==1 || im(xc,yc+1)==1 || ...
                    im(xc-1,yc)==1 || im(xc,yc-1)==1 ||
                im(xc+1,yc+1)==1 || im(xc-1,yc+1)==1 ...
                        || im(xc-1,yc-1)==1 || im(xc+1,yc-1)==1
                    npix=npix+1;
                    xpix=[xpix xc]; ypix=[ypix yc];
                    xxline=[xxline xc];
                    xstore=[xstore xc]; ystore=[ystore yc];
                    xc=xc+1;
                    xline(find(xline==xc))=[];
                end
            else
                check3=0;
            end
        end

        xc=xs-1;
        xline(find(xline==xc))=[];
        check4=1; % left direction
        while check4==1
            if im(xc,yc)==1 && xc<size(im,1) && yc<size(im,2) && ...
                    xc>1 && yc>1
                if im(xc+1,yc)==1 || im(xc,yc+1)==1 || ...
                    im(xc-1,yc)==1 || im(xc,yc-1)==1 ||
                im(xc+1,yc+1)==1 || im(xc-1,yc+1)==1 ...
                        || im(xc-1,yc-1)==1 || im(xc+1,yc-1)==1
                    npix=npix+1;
                    xpix=[xpix xc]; ypix=[ypix yc];
                    xxline=[xxline xc];
                    xstore=[xstore xc]; ystore=[ystore yc];
                    xc=xc-1;
                    xline(find(xline==xc))=[];
                end
```

```
            else
                check4=0;
            end
        end
    end
    yc=yc-1;
end
plot(ystore,xstore,'r.')
area=[area npix];

% calculate centroid and ellipse dimensions
xcentroid=mean(xpix);
ycentroid=mean(ypix);
plot(ycentroid,xcentroid,'bx')
da=1; theta=0; dxr=0; dyr=0;
for lp=1:1:180
    rcheck=1;
    rcount=1;
    while rcheck==1 && xcentroid+dxr<size(im,1) && ...
         ycentroid+dyr<size(im,2) && xcentroid+dxr>1 && ycentroid+dyr>1
        if im(floor(xcentroid+dxr),floor(ycentroid+dyr))==0
            rcheck=0;
        end
        dxr=rcount*cosd(lp);
        dyr=rcount*sind(lp);
        rcount=rcount+1;
    end
    lcheck=1;
    lcount=1;
    dxl=0; dyl=0;
    while lcheck==1 && xcentroid+dxl<size(im,1) && ...
         ycentroid+dyl<size(im,2) && xcentroid+dxl>1 && ycentroid+dyl>1
        if im(floor(xcentroid+dxl),floor(ycentroid+dyl))==0
            lcheck=0;
        end
        dxl=lcount*cosd(lp+180);
        dyl=lcount*sind(lp+180);
        lcount=lcount+1;
    end
    if rcount+lcount>da
        da=rcount+lcount;
        theta=lp;
        axr=xcentroid+dxr; ayr=ycentroid+dyr;
        axl=xcentroid+dxl; ayl=ycentroid+dyl;
    end
end
line([ayr ayl],[axr axl])
% plot minor axis
rcheck=1;
rcount=1;
mxr=0; myr=0;
while rcheck==1 && xcentroid+mxr<size(im,1) && ...
         ycentroid+myr<size(im,2) && xcentroid+mxr>1 && ycentroid+myr>1
    if im(floor(xcentroid+mxr),floor(ycentroid+myr))==0
        rcheck=0;
    end
    mxr=rcount*cosd(theta-90);
    myr=rcount*sind(theta-90);
    rcount=rcount+1;
end
lcheck=1;
lcount=1;
mxl=0; myl=0;
```

```
    while lcheck==1 && xcentroid+mxl<size(im,1) && ...
              ycentroid+myl<size(im,2) && xcentroid+mxl>1 && ycentroid+myl>1
        if im(floor(xcentroid+mxl),floor(ycentroid+myl))==0
            lcheck=0;
        end
        mxl=lcount*cosd(theta+90);
        myl=lcount*sind(theta+90);
        lcount=lcount+1;
    end
    db=rcount+lcount;
    bxr=xcentroid+mxr; byr=ycentroid+myr;
    bxl=xcentroid+mxl; byl=ycentroid+myl;
    line([byr byl],[bxr bxl])

    major=[major da]; minor=[minor db]; direction=[direction theta];

end

% print results
disp('area'); disp(area')
disp('major axis'); disp(major')
disp('minor axis'); disp(minor')
disp('direction'); disp(direction')
```

Appendix F: SPSS statistics for experimental significance

For our statistical analysis, we conducted a comparison of means between 60- and 0 RPM specimens using a 2-tailed t-test and identified significance as $*p<0.05$.

<u>0 hr time point:</u>

Group Statistics

	VAR00003	N	Mean	Std. Deviation	Std. Error Mean
VAR00001	1.00	3	3539.3333	2099.02866	1211.87476
	2.00	3	2583.6667	439.00607	253.46028

Independent Samples Test

		Levene's Test for Equality of Variances		t-test for Equality of Means						
									95% Confidence Interval of the Difference	
		F	Sig.	t	df	Sig. (2-tailed)	Mean Difference	Std. Error Difference	Lower	Upper
VAR00001	Equal variances assumed	2.331	.202	.772	4	.483	955.66667	1238.09634	-2481.83987	4393.17320
	Equal variances not assumed			.772	2.175	.515	955.66667	1238.09634	-3981.76455	5893.09789

<u>1 hr time point:</u>

Group Statistics

	VAR00003	N	Mean	Std. Deviation	Std. Error Mean
VAR00001	1.00	3	5563.3333	2461.39114	1421.08484
	2.00	3	3733.6667	2299.57873	1327.66240

Independent Samples Test

		Levene's Test for Equality of Variances		t-test for Equality of Means						
									95% Confidence Interval of the Difference	
		F	Sig.	t	df	Sig. (2-tailed)	Mean Difference	Std. Error Difference	Lower	Upper
VAR00001	Equal variances assumed	.113	.754	.941	4	.400	1829.66667	1944.78008	-3569.90846	7229.24180
	Equal variances not assumed			.941	3.982	.400	1829.66667	1944.78008	-3579.73932	7239.07266

2 hr time point:

Group Statistics

	VAR00003	N	Mean	Std. Deviation	Std. Error Mean
VAR00001	1.00	3	2849.6667	850.79982	491.20950
	2.00	3	5382.6667	1610.44849	929.79287

Independent Samples Test

		Levene's Test for Equality of Variances		t-test for Equality of Means						
									95% Confidence Interval of the Difference	
		F	Sig.	t	df	Sig. (2-tailed)	Mean Difference	Std. Error Difference	Lower	Upper
VAR00001	Equal variances assumed	1.954	.235	-2.409	4	.074	-2533.00000	1051.57099	-5452.62914	386.62914
	Equal variances not assumed			-2.409	3.036	.094	-2533.00000	1051.57099	-5857.39941	791.39941

3 hr time point:

Group Statistics

	VAR00003	N	Mean	Std. Deviation	Std. Error Mean
VAR00001	1.00	3	3561.0000	801.17102	462.55630
	2.00	3	5028.0000	2470.68553	1426.45096

Independent Samples Test

		Levene's Test for Equality of Variances		t-test for Equality of Means						
									95% Confidence Interval of the Difference	
		F	Sig.	t	df	Sig. (2-tailed)	Mean Difference	Std. Error Difference	Lower	Upper
VAR00001	Equal variances assumed	6.017	.070	-.978	4	.383	-1467.00000	1499.57349	-5630.48349	2696.48349
	Equal variances not assumed			-.978	2.416	.415	-1467.00000	1499.57349	-6963.17091	4029.17091

4 hr time point:

Group Statistics

	VAR00003	N	Mean	Std. Deviation	Std. Error Mean
VAR00001	1.00	3	3564.6667	677.47275	391.13908
	2.00	3	7006.3333	2035.23103	1175.04118

Independent Samples Test

		Levene's Test for Equality of Variances		t-test for Equality of Means						
									95% Confidence Interval of the Difference	
		F	Sig.	t	df	Sig. (2-tailed)	Mean Difference	Std. Error Difference	Lower	Upper
VAR00001	Equal variances assumed	5.029	.088	-2.779	4	.050	-3441.66667	1238.43109	-6880.10259	-3.23074
	Equal variances not assumed			-2.779	2.438	.087	-3441.66667	1238.43109	-7950.44320	1067.10986

5 hr time point:

Group Statistics

	VAR00003	N	Mean	Std. Deviation	Std. Error Mean
VAR00001	1.00	3	4399.6667	765.90230	442.19390
	2.00	3	10625.3333	3571.25207	2061.86334

Independent Samples Test

		Levene's Test for Equality of Variances		t-test for Equality of Means						
									95% Confidence Interval of the Difference	
		F	Sig.	t	df	Sig. (2-tailed)	Mean Difference	Std. Error Difference	Lower	Upper
VAR00001	Equal variances assumed	8.895	.041	-2.952	4	.042	-6225.66667	2108.74747	-12080.48826	-370.84508
	Equal variances not assumed			-2.952	2.184	.088	-6225.66667	2108.74747	-14605.65858	2154.32525

6 hr time point:

Group Statistics

	VAR00003	N	Mean	Std. Deviation	Std. Error Mean
VAR00001	1.00	3	3713.3333	1360.50187	785.48612
	2.00	3	10643.6667	3232.37534	1866.21277

Independent Samples Test

		Levene's Test for Equality of Variances		t-test for Equality of Means						
									95% Confidence Interval of the Difference	
		F	Sig.	t	df	Sig. (2-tailed)	Mean Difference	Std. Error Difference	Lower	Upper
VAR00001	Equal variances assumed	3.746	.125	-3.423	4	.027	-6930.33333	2024.78111	-12552.02694	-1308.63972
	Equal variances not assumed			-3.423	2.687	.049	-6930.33333	2024.78111	-13820.16085	-40.50582

7 hr time point:

Group Statistics

	VAR00003	N	Mean	Std. Deviation	Std. Error Mean
VAR00001	1.00	3	3933.6667	1764.38582	1018.66863
	2.00	3	10822.3333	3418.33415	1973.57614

Independent Samples Test

		Levene's Test for Equality of Variances		t-test for Equality of Means						
									95% Confidence Interval of the Difference	
		F	Sig.	t	df	Sig. (2-tailed)	Mean Difference	Std. Error Difference	Lower	Upper
VAR00001	Equal variances assumed	2.738	.173	-3.102	4	.036	-6888.66667	2220.96568	-13055.05596	-722.27737
	Equal variances not assumed			-3.102	2.995	.053	-6888.66667	2220.96568	-13963.40492	186.07158

8 hr time point:

Group Statistics

	VAR00003	N	Mean	Std. Deviation	Std. Error Mean
VAR00001	1.00	3	4246.3333	1899.38999	1096.61332
	2.00	3	12440.6667	3424.62163	1977.20622

Independent Samples Test

		Levene's Test for Equality of Variances		t-test for Equality of Means						
									95% Confidence Interval of the Difference	
		F	Sig.	t	df	Sig. (2-tailed)	Mean Difference	Std. Error Difference	Lower	Upper
VAR00001	Equal variances assumed	2.357	.200	-3.624	4	.022	-8194.33333	2260.95228	-14471.74323	-1916.92344
	Equal variances not assumed			-3.624	3.124	.034	-8194.33333	2260.95228	-15230.69009	-1157.97658

References

[1] National Aeronautics and Space Administration. About NASA. *What Does NASA Do?* Retrieved January 26, 2013, from www.nasa.gov/about/highlights/what_does_nasa_do.html

[2] National Aeronautics and Space Administration. Budget. *FY 13 Budget.* Retrieved January 26, 2013, from www.nasa.gov/news/budget/index.html

[3] Horneck, G., Klaus, D. M., & Mancinelli, R. L. (2010). Space microbiology. *Microbiology and Molecular Biology Reviews*, *74*(1), 121-156.

[4] Vitale, R. (2012). Plutonium powers this Red Planet rover. *The Columbus Dispatch.* Retrieved January 26, 2013, from www.dispatch.com/content/stories/science/2012/09/02/plutonium-powers-this-red-planet-rover.html

[5] Andrykowski, M. A., Carpenter, J. S., Greiner, C. B., Altmaier, E. M., Burish, T. G., Antin, J. H., Gingrich, R., Cordova, M. J., & Henslee-Downey, P. J. (1997). Energy level and sleep quality following bone marrow transplantation. *Bone marrow transplantation*, *20*(8), 669-679.

[6] Mathieu, P. S., & Loboa, E. G. (2012). Cytoskeletal and Focal Adhesion Influences on Mesenchymal Stem Cell Shape, Mechanical Properties, and Differentiation Down Osteogenic, Adipogenic, and Chondrogenic Pathways. *Tissue Engineering Part B: Reviews, 18*(6), 436-444.

[7] Li, J., Zhang, S., Chen, J., Du, T., Wang, Y., & Wang, Z. (2009). Modeled microgravity causes changes in the cytoskeleton and focal adhesions, and decreases in migration in malignant human MCF-7 cells. *Protoplasma*, *238*(1), 23-33.

[8] Crawford-Young, S. J. (2006). Effects of microgravity on cell cytoskeleton and embryogenesis. *International journal of developmental biology*, *50*(2), 183-191.

[9] Gershovich, P. M., Gershovich, J. G., & Buravkova, L. B. (2009). Cytoskeleton structure and adhesion properties of human stromal precursors under conditions of simulated microgravity. *Cell and Tissue Biology*, *3*(5), 423-430.

[10] Slentz, D. H., Truskey, G. A., & Kraus, W. E. (2001). Effects of chronic exposure to simulated microgravity on skeletal muscle cell proliferation and differentiation. *In Vitro Cellular & Developmental Biology-Animal*, *37*(3), 148-156.

[11] Hirasaka, K., Nikawa, T., Yuge, L., Ishihara, I., Higashibata, A., Ishioka, N., Okubo, A., Miyashita, T., Suzue, N., Ogawa, T., Orada, M., & Kishi, K. (2005). Clinorotation prevents differentiation of rat myoblastic L6 cells in association with reduced NF-κB signaling. *Biochimica et Biophysica Acta (BBA)-Molecular Cell Research*, *1743*(1), 130-140.

[12] Ontiveros, C., & McCabe, L. R. (2002). Simulated microgravity suppresses osteoblast phenotype, Runx2 levels and AP-1 transactivation. *Journal of cellular biochemistry*, *88*(3), 427-437.

[13] Unsworth, B. R., & Lelkes, P. I. (1998). Growing tissues in microgravity. *Nature medicine*, *4*(8), 901-907.

[14] Scheuring, R. A., Mathers, C. H., Jones, J. A., & Wear, M. L. (2009). Musculoskeletal injuries and minor trauma in space: incidence and injury mechanisms in US astronauts. *Aviation, Space, and Environmental Medicine*, *80*(2), 117-124.

[15] Vico, L., Collet, P., Guignandon, A., Lafage-Proust, M. H., Thomas, T., Rehailia, M., & Alexandre, C. (2000). Effects of long-term microgravity exposure on cancellous and cortical weight-bearing bones of cosmonauts. *The Lancet*, *355*(9215), 1607-1611.

[16] Leblanc, A. D., Schneider, V. S., Evans, H. J., Engelbretson, D. A., & Krebs, J. M. (2009). Bone mineral loss and recovery after 17 weeks of bed rest. *Journal of Bone and Mineral Research*, *5*(8), 843-850.

[17] Holick, M. F. (1998). Perspective on the impact of weightlessness on calcium and bone metabolism. *Bone*, *22*(5), 105S-111S.

[18] LeBlanc, A., Schneider, V., Shackelford, L., West, S., Oganov, V., Bakulin, A., & Voronin, L. (2000). Bone mineral and lean tissue loss after long duration space flight. *J Musculoskelet Neuronal Interact*, *1*(2), 157-60.

[19] Gupta, S., Manske, S. L., & Judex, S. (2012). Increasing the number of unloading/reambulation cycles does not adversely impact body composition and lumbar bone mineral density but reduces tissue sensitivity. *Acta Astronautica*. *In press.*

[20] Fitts, R. H., Riley, D. R., & Widrick, J. J. (2001). Functional and structural adaptations of skeletal muscle to microgravity. *Journal of Experimental Biology*, *204*(18), 3201-3208.

[21] Williams, D., Kuipers, A., Mukai, C., & Thirsk, R. (2009). Acclimation during space flight: effects on human physiology. *Canadian Medical Association Journal*, *180*(13), 1317-1323.

[22] Sayson, J. V., & Hargens, A. R. (2008). Pathophysiology of low back pain during exposure to microgravity. *Aviation, space, and environmental medicine*, *79*(4), 365-373.

[23] Johnston, S. L., Campbell, M. R., Scheuring, R., & Feiveson, A. H. (2010). Risk of herniated nucleus pulposus among US astronauts. *Aviation, space, and environmental medicine*, *81*(6), 566-574.

[24] Yew, A. G. (2008). The Equilibrium Geometry Theory for Bone Fracture Healing. MS Thesis. University of Maryland, College Park. Print.

[25] Bagge, M. (2000). A model of bone adaptation as an optimization process. *Journal of Biomechanics*, *33*(11), 1349-1357.

[26] Tsubota, K. I., Adachi, T., & Tomita, Y. (2002). Functional adaptation of cancellous bone in human proximal femur predicted by trabecular surface remodeling simulation toward uniform stress state. *Journal of biomechanics*, *35*(12), 1541-1551.

[27] Chen, X. Y., Zhang, X. Z., Guo, Y., Li, R. X., Lin, J. J., & Wei, Y. (2008). The establishment of a mechanobiology model of bone and functional adaptation in response to mechanical loading. *Clinical Biomechanics*, *23*, S88-S95.

[28] Okumura Y., Nikawa T. (2011). Mechanobiology in Space. Mechanosensing Biology, Noda M. (Ed.) Springer. 63-70.

[29] Brown, A. H. (2007). From gravity and the organism to gravity and the cell. *Gravitational and Space Biology*, *4*(2), 7-18.

[30] Todd, P. (2007). Gravity-dependent phenomena at the scale of the single cell. *Gravitational and Space Biology*, *2*(1), 95-113.

[31] Albrecht-Buehler, G. (2007). Possible mechanisms of indirect gravity sensing by cells. *Gravitational and Space Biology*, *4*(2), 25-34.

[32] Hughes-Fulford, M. (2003). Function of the cytoskeleton in gravisensing during spaceflight. *Advances in Space Research*, *32*(8), 1585-1593.

[33] Hehlgans, S., Haase, M., & Cordes, N. (2007). Signalling via integrins: implications for cell survival and anticancer strategies. *Biochimica et Biophysica Acta (BBA)-Reviews on Cancer*, *1775*(1), 163-180.

[34] Voller, A., Bartlett, A., & Bidwell, D. E. (1978). Enzyme immunoassays with special reference to ELISA techniques. *Journal of Clinical Pathology*, *31*(6), 507-520.

[35] Burnette, W. N. (1981). Western blotting: Electrophoretic transfer of proteins from sodium dodecly sulfate-polyacrylamide gels to unmodified nitrocellulose and radiographic detection with antibody and radioiodinated protein a. *Anal. Biochem.*, *112*, 195-203.

[36] Bartlett, J. M., & Stirling, D. (2003). A short history of the polymerase chain reaction. *DNA*, *226*, 3-6.

[37] Morey-Holton, E. R., & Globus, R. K. (1998). Hindlimb unloading of growing rats: a model for predicting skeletal changes during space flight. *Bone*, *22*(5), 83S-88S.

[38] Bloomfield, S. A., Allen, M. R., Hogan, H. A., & Delp, M. D. (2002). Site- and compartment-specific changes in bone with hindlimb unloading in mature adult rats. *Bone*, *31*(1), 149-157.

[39] Silva, A. V. D., & Volpon, J. B. (2004). Model of tail suspension and its effect in some mechanical properties of the rat bone. *Acta Ortopédica Brasileira*, *12*(1), 22-31.

[40] Synthecon Inc. *Rotary cell culture systems.* Retrieved January 26, 2013, from http://www.synthecon.com/rotary-cell-culture-systems.html

[41] Cogoli, M. (1992). The fast rotating clinostat: a history of its use in gravitational biology and a comparison of ground-based and flight experiment results. *ASGSB bulletin: publication of the American Society for Gravitational and Space Biology*, *5*(2), 59-67.

[42] Schatten, H., Lewis, M. L., & Chakrabarti, A. (2001). Spaceflight and clinorotation cause cytoskeleton and mitochondria changes and increases in apoptosis in cultured cells. *Acta astronautica*, *49*(3), 399-418.

[43] Glade, N., Beaugnon, E., & Tabony, J. (2006). Ground-based methods reproduce space-flight experiments and show that weak vibrations trigger microtubule self-organisation. *Biophysical chemistry*, *121*(1), 1.

[44] Dedolph, R. R., & Dipert, M. H. (1971). The physical basis of gravity stimulus nullification by clinostat rotation. *Plant physiology*, *47*(6), 756-764.

[45] Klaus, D. M. (2007). Clinostats and bioreactors. *Gravitational and Space Biology*, *14*(2), 55-64.

[46] Unsworth, B. R., & Lelkes, P. I. (1998). Growing tissues in microgravity. *Nature medicine*, *4*(8), 901-907.

[47] Martin, I., Wendt, D., & Heberer, M. (2004). The role of bioreactors in tissue engineering. *TRENDS in Biotechnology*, *22*(2), 80-86.

[48] Dai, Z. Q., Wang, R., Ling, S. K., Wan, Y. M., & Li, Y. H. (2007). Simulated microgravity inhibits the proliferation and osteogenesis of rat bone marrow mesenchymal stem cells. *Cell proliferation*, *40*(5), 671-684.

[49] Koç, A., Emin, N., Elçin, A. E., & Elçin, Y. M. (2008). In vitro osteogenic differentiation of rat mesenchymal stem cells in a microgravity bioreactor. *Journal of Bioactive and Compatible Polymers*, *23*(3), 244-261.

[50] Zayzafoon, M., Gathings, W. E., & McDonald, J. M. (2004). Modeled microgravity inhibits osteogenic differentiation of human mesenchymal stem cells and increases adipogenesis. *Endocrinology*, *145*(5), 2421-2432.

[51] Meyers, V. E., Zayzafoon, M., Douglas, J. T., & McDonald, J. M. (2005). RhoA and cytoskeletal disruption mediate reduced osteoblastogenesis and enhanced adipogenesis of human mesenchymal stem cells in modeled microgravity. *Journal of Bone and Mineral Research*, *20*(10), 1858-1866.

[52] Yuge, L., Kajiume, T., Tahara, H., Kawahara, Y., Umeda, C., Yoshimoto, R., Wu, S., Yamaoka, K., Asashima, M., Kataoka, K., & Ide, T. (2006). Microgravity potentiates stem cell proliferation while sustaining the capability of differentiation. *Stem cells and development*, *15*(6), 921-929.

[53] Stiehler, M., Bünger, C., Baatrup, A., Lind, M., Kassem, M., & Mygind, T. (2009). Effect of dynamic 3-D culture on proliferation, distribution, and osteogenic differentiation of human mesenchymal stem cells. *Journal of Biomedical Materials Research Part A*, *89*(1), 96-107.

[54] Chen, X., Xu, H., Wan, C., McCaigue, M., & Li, G. (2006). Bioreactor Expansion of Human Adult Bone Marrow-Derived Mesenchymal Stem Cells. *Stem Cells*, *24*(9), 2052-2059.

[55] Liu, K., Tian, Y., Burrows, S. M., Reif, R. D., & Pappas, D. (2009). Mapping vortex-like hydrodynamic flow in microfluidic networks using fluorescence correlation spectroscopy. *Analytica chimica acta*, *651*(1), 85-90.

[56] Liu, K., Pitchimani, R., Dang, D., Bayer, K., Harrington, T., & Pappas, D. (2008). Cell culture chip using low-shear mass transport. *Langmuir*, *24*(11), 5955-5960.

[57] Gupta, K., Kim, D. H., Ellison, D., Smith, C., Kundu, A., Tuan, J., Suh, K., & Levchenko, A. (2010). Lab-on-a-chip devices as an emerging platform for stem cell biology. *Lab Chip*, *10*(16), 2019-2031.

[58] Kim, L., Toh, Y. C., Voldman, J., & Yu, H. (2007). A practical guide to microfluidic perfusion culture of adherent mammalian cells. *Lab Chip*, *7*(6), 681-694.

[59] Tourovskaia, A., Figueroa-Masot, X., & Folch, A. (2004). Differentiation-on-a-chip: a microfluidic platform for long-term cell culture studies. *Lab Chip*, *5*(1), 14-19.

[60] Ahmed, T., Shimizu, T. S., & Stocker, R. (2010). Bacterial chemotaxis in linear and nonlinear steady microfluidic gradients. *Nano letters*, *10*(9), 3379-3385.

[61] Chung, B. G., & Choo, J. (2010). Microfluidic gradient platforms for controlling cellular behavior. *Electrophoresis*, *31*(18), 3014-3027.

[62] Atencia, J., Morrow, J., & Locascio, L. E. (2009). The microfluidic palette: A diffusive gradient generator with spatio-temporal control. *Lab on a Chip*, *9*(18), 2707-2714.

[63] Meyvantsson, I., & Beebe, D. J. (2008). Cell culture models in microfluidic systems. *Annu. Rev. Anal. Chem.*, *1*, 423-449.

[64] Mach, A. J., Kim, J. H., Arshi, A., Hur, S. C., & Di Carlo, D. (2011). Automated cellular sample preparation using a Centrifuge-on-a-Chip. *Lab on a Chip*, *11*(17), 2827-2834.

[65] LeBlanc, A. D., Spector, E. R., Evans, H. J., & Sibonga, J. D. (2007). Skeletal responses to space flight and the bed rest analog: a review. *Journal of Musculoskeletal and Neuronal Interactions*, *7*(1), 33-47.

[66] LeBlanc, A. D., Evans, H. J., Schneider, V. S., Wendt 3rd, R. E., & Hedrick, T. D. (1994). Changes in intervertebral disc cross-sectional area with bed rest and space flight. *Spine*, *19*(7), 812-817.

[67] Ban, Y., Wu, Y. Y., Yu, T., Geng, N., Wang, Y. Y., Liu, X. G., & Gong, P. (2011). Response of osteoblasts to low fluid shear stress is time dependent. *Tissue and Cell*, *43*(5), 311-317.

[68] Huiskes, R., Driel, W. V., Prendergast, P. J., & Søballe, K. (1997). A biomechanical regulatory model for periprosthetic fibrous-tissue differentiation. *Journal of materials science: Materials in medicine*, *8*(12), 785-788.

[69] Park, J. Y., Yoo, S. J., Hwang, C. M., & Lee, S. H. (2009). Simultaneous generation of chemical concentration and mechanical shear stress gradients using microfluidic osmotic flow comparable to interstitial flow. *Lab Chip*, *9*(15), 2194-2202.

[70] Raty, S., Walters, E. M., Davis, J., Zeringue, H., Beebe, D. J., Rodriguez-Zas, S. L., & Wheeler, M. B. (2004). Embryonic development in the mouse is enhanced via microchannel culture. *Lab Chip*, *4*(3), 186-190.

[71] Weiss, R. F., & Florsheim, B. H. (1965). Flow in a cavity at low Reynolds number. *Physics of Fluids*, *8*(9), 1631-1635.

[72] Atencia, J., Cooksey, G. A., & Locascio, L. E. (2012). A robust diffusion-based gradient generator for dynamic cell assays. *Lab on a Chip*, *12*(2), 309-316.

[73] Wang, C. P., Sadeghi, F., Wereley, S. T., & Chuang, H. S. (2009). Investigation of Fluid Flow Out of a Microcavity Using μ PIV. *Tribology Transactions*, *52*(6), 817-832.

[74] Lee, Y. K., Wong, M., & Zohar, Y. (2005). Fluid flows in microchannels with cavities. *Microelectromechanical Systems, Journal of*, *14*(6), 1386-1398.

[75] Shankar, P. N., & Deshpande, M. D. (2000). Fluid mechanics in the driven cavity. *Annual Review of Fluid Mechanics*, *32*(1), 93-136.

[76] Pozrikidis, C. (1994). Shear flow over a plane wall with an axisymmetric cavity or a circular orifice of finite thickness. *Physics of Fluids*, *6*, 68-79.

[77] Crank, J. (1975]. The Mathematics of Diffusion, Oxford University Press, London.

[78] Lee, P. J., Hung, P. J., Rao, V. M., & Lee, L. P. (2006). Nanoliter scale microbioreactor array for quantitative cell biology. *Biotechnology and bioengineering*, *94*(1), 5-14.

[79] Begley, C. M., & Kleis, S. J. (2000). The fluid dynamic and shear environment in the NASA/JSC rotating-wall perfused-vessel bioreactor. *Biotechnology and bioengineering*, *70*(1), 32-40.

[80] Aroesty, J., & Gross, J. F. (1970). Convection and diffusion in the microcirculation. *Microvascular Research*, *2*(3), 247-267.

[81] Beebe, D. J., Mensing, G. A., & Walker, G. M. (2002). Physics and applications of microfluidics in biology. *Annual review of biomedical engineering*, *4*(1), 261-286.

[82] European Space Agency. DLR – Clinostats, centrifuges, RPM. *Human spaceflight research.* Retrieved December 20, 2012, from http://www.esa.int/Our_Activities/Human_Spaceflight/Human_Spaceflight_Research/DLR_-_Clinostats_Centrifugues_RPM

[83] Pache, C., Kühn, J., Westphal, K., Toy, M. F., Parent, J., Büchi, O., Franco-Obregon, A., Depeursinge, C., & Egli, M. (2010). Digital holographic microscopy real-time monitoring of cytoarchitectural alterations during simulated microgravity. *Journal of biomedical optics*, *15*(2), 026021-026021.

[84] Toy, M. F., Richard, S., Kühn, J., Franco-Obregón, A., Egli, M., & Depeursinge, C. (2012). Enhanced robustness digital holographic microscopy for demanding environment of space biology. *Biomedical Optics Express*, *3*(2), 313-326.

[85] van Loon, J. J. (2007). Some history and use of the random positioning machine, RPM, in gravity related research. *Advances in Space research*, *39*(7), 1161-1165.

[86] Gu, B., Chen, Y., & Zhu, D. (2007). Prediction of leakage rates through sealing connections with nonmetallic gaskets. *Chinese Journal of Chemical Engineering*, *15*(6), 837-841.

[87] Arghavani, J., Derenne, M., & Marchand, L. (2002). Prediction of gasket leakage rate and sealing performance through fuzzy logic. *The International Journal of Advanced Manufacturing Technology*, *20*(8), 612-620.

[88] Gu, B. Q., Sun, Z. G., Li, Y. Y., Huang, X. L., Zhou, J. F., & Shao, C. L. (2010). Study on Time-Correlated Leakage Predication Model of Nonmetallic Gaskets. *Advanced Materials Research*, *97*, 629-633.

[89] Greenwood, J. A., & Williamson, J. B. P. (1966). Contact of nominally flat surfaces. *Proceedings of the Royal Society of London. Series A. Mathematical and Physical Sciences*, *295*(1442), 300-319.

[90] Bush, A. W., Gibson, R. D., & Thomas, T. R. (1975). The elastic contact of a rough surface. *Wear*, *35*(1), 87-111.

[91] Adams, G. G., & Nosonovsky, M. (2000). Contact modeling—forces. *Tribology International*, *33*(5), 431-442.

[92] Carbone, G., & Bottiglione, F. (2008). Asperity contact theories: Do they predict linearity between contact area and load?. *Journal of the Mechanics and Physics of Solids*, *56*(8), 2555-2572.

[93] Yang, C., Tartaglino, U., & Persson, B. N. J. (2006). A multiscale molecular dynamics approach to contact mechanics. *The European Physical Journal E: Soft Matter and Biological Physics*, *19*(1), 47-58.

[94] Borri-Brunetto, M., Chiaia, B., & Ciavarella, M. (2001). Incipient sliding of rough surfaces in contact: a multiscale numerical analysis. *Computer methods in applied mechanics and engineering*, *190*(46), 6053-6073.

[95] Lorenz, B., & Persson, B. N. (2010). Leak rate of seals: Effective-medium theory and comparison with experiment. *The European Physical Journal E: Soft Matter and Biological Physics*, *31*(2), 159-167.

[96] Barry, F. P. (2008). Mesenchymal stem cell therapy in joint disease. *Tissue Engineering of Cartilage and Bone: Novartis Foundation Symposium, 249*, 86-102.

[97] Granero-Moltó, F., Weis, J. A., Miga, M. I., Landis, B., Myers, T. J., O'Rear, L., Longobardi, L., Jansen E. D., Mortlock D. P., & Spagnoli, A. (2009). Regenerative effects of transplanted mesenchymal stem cells in fracture healing. *Stem cells*, *27*(8), 1887-1898.

[98] Luo, W., Xiong, W., Qiu, M., Lv, Y., Li, Y., & Li, F. (2011). Differentiation of mesenchymal stem cells towards a nucleus pulposus-like phenotype utilizing simulated microgravity In vitro. *Journal of Huazhong University of Science and Technology: Medical Sciences*, *31*(2), 199-203.

[99] Discher, D. E., Mooney, D. J., & Zandstra, P. W. (2009). Growth factors, matrices, and forces combine and control stem cells. *Science*, *324*(5935), 1673-1677.

[100] Yamashita, A., Nishikawa, S., & Rancourt, D. E. (2010). Microenvironment modulates osteogenic cell lineage commitment in differentiated embryonic stem cells. *PloS one*, *5*(3), e9663.

[101] Tamma, R., Colaianni, G., Camerino, C., Di Benedetto, A., Greco, G., Strippoli, M., Vergari R., Grano, A., Mancini, L., Giorgio M., Colucci S., Grano M., & Zallone, A. (2009). Microgravity during spaceflight directly affects in vitro osteoclastogenesis and bone resorption. *The FASEB Journal*, *23*(8), 2549-2554.

[102] Nabavi, N., Khandani, A., Camirand, A., & Harrison, R. E. (2011). Effects of microgravity on osteoclast bone resorption and osteoblast cytoskeletal organization and adhesion. *Bone*, *49*(5), 965-974.

[103] McCabe, N. P., Androjna, C., Hill, E., Globus, R. K., & Midura, R. J. (2012). Simulated microgravity alters the expression of key genes involved in fracture healing. *Acta Astronautica*. *In press.*

[104] Uccelli, A., Moretta, L., & Pistoia, V. (2008). Mesenchymal stem cells in health and disease. *Nature Reviews Immunology*, *8*(9), 726-736.

[105] Ding, D. C., Shyu, W. C., & Lin, S. Z. (2011). Mesenchymal stem cells. *Cell transplantation*, *20*(1), 5-14.

[106] Chamberlain, G., Fox, J., Ashton, B., & Middleton, J. (2007). Concise review: mesenchymal stem cells: their phenotype, differentiation capacity, immunological features, and potential for homing. *Stem cells*, *25*(11), 2739-2749.

[107] Gao, J., Dennis, J. E., Muzic, R. F., Lundberg, M., & Caplan, A. I. (2001). The dynamic in vivo distribution of bone marrow-derived mesenchymal stem cells after infusion. *Cells Tissues Organs*, *169*(1), 12-20.

[108] McBeath, R., Pirone, D. M., Nelson, C. M., Bhadriraju, K., & Chen, C. S. (2004). Cell shape, cytoskeletal tension, and RhoA regulate stem cell lineage commitment. *Developmental cell*, *6*(4), 483-495.

[109] Finkelstein, H., Dvorochkin, N., Yousuf, R., Globus, R.K., Almeida, E.A. (2010) Spaceflight Reduces the Tissue Regenerative Potential of Stem Cells by Decreasing Proliferation and Increasing Early Differentiation. Stem Cells Biology Poster Session. 50th Annual Meeting of the American Society for Cell Biology, Philadelphia, PA, December 11-15, 2010.

[110] Sokal, R. R., & Rohlf, F. J. (1995). Assumptions of analysis of variance. *Biometry: The Principles and Practice of Statistics in Biological Research. 3rd ed. New York: WH Freeman*, 396-406.